The rare villin-expressing cell of the murine lower airway is a neuroendocrine cell producing the chemokine C-X-C motif ligand 13 under homeostatic conditions

Inaugural Dissertation

submitted to the

Faculty of Medicine

in partial fulfillment of the requirements

for the PhD-Degree

of the Faculties of Veterinary Medicine and Medicine

of the Justus Liebig University Giessen

by

Mahmoud, Wafaa

from

Jordan

Giessen 2021

From the Institute of Anatomy and Cell Biology
Director / Chairman: Prof. Dr. Wolfgang Kummer
of the Faculty of Medicine of the Justus Liebig University Giessen

First Supervisor and Committee Member: Prof. Dr. Wolfgang Kummer
Second Supervisor and Committee Member: Prof. Dr. Christiane Herden
Chairman and Committee Member: Prof. Dr. Martin Diener
External Reviewer and Committee Member: Prof. Dr. Matthias Ochs

Date of Doctoral Defense: 17/12/2021

Table of contents

Table of contents

List of abbreviations

5-HTP	5-hydroxytryptophan
AADC	aromatic L-amino acid decarboxylase
ACh	acetylcholine
APUD	amine precursors uptake and decarboxylation
Ascl1	achaete-scute homolog 1
BALT	bronchus-associated lymphoid tissue
BCA-1	B cell–attracting chemokine
BLC	B lymphocyte chemoattractant
BLR1	Burkitt's Lymphoma Receptor 1
CALHM1	calcium homeostasis modulator 1
CB	calbindin D-28
CCL11	chemokine (C-C motif) ligand 11
CCL19	chemokine (C-C motif) ligand 19
CCL2	chemokine (C-C motif) ligand 2
CCL21	chemokine (C-C motif) ligand 21
CCL22	chemokine (C-C motif) ligand 22
CCL26	chemokine (C-C motif) ligand 26
CFTR	cystic fibrosis transmembrane regulator
CGRP	calcitonin gene-related peptide
ChAT	choline acetyltransferase
COPD	chronic obstructive pulmonary disease
CTL4	choline transporter-like protein 4
CXCL12	C-X-C motif chemokine ligand 12
CXCL13	C-X-C motif chemokine ligand 13

List of abbreviations

CXCR5	C-X-C chemokine receptor type 5
DAB	3.3′-diaminobenzidine-hydrochloride
DC	dendritic cells
DOPA	3,4-dihydroxyphenylalanine
DPSS	diode pumped solide state 561
E	embryonic days
eGFP	enhanced green fluorescent protein
EhABPH	entamoeba histolytica actin-binding protein homologue
GABA	gamma-aminobutyric acid
GAD67	glutamic acid decarboxylase 67
GDF-15	growth differentiation factors 15
GNAT3	G protein α-gustducin
GPCR	G protein-coupled receptors
HEPES	(2-hydroxyethyl)-1-piperazineethanesulfonic acid
IFN-γ	interferon gamma
IL-25	interleukin 25
IL-8	interleukin 8
Mash1	mammalian achaete-scute homolog 1
MCP1	monocyte chemoattractant protein 1
MDC	macrophage-derived chemokine
NAChRs	nicotinic acetylcholine receptors
NEB	neuroepithelial bodies
OCTs	organic cation transporters
PCA	principle component analysis
PCR	polymerase chain reaction
PGP 9.5	protein gene product 9.5

List of abbreviations

PIP2	phosphatidylinositol 4,5-bisphosphate
PLC-β2	phospholipase C isoform β2
PLC-γ1	phospholipase C-γ1
Pou2f3	POU domain, class 2, transcription factor 3
PRL-3	phosphatase of regenerating liver 3
Ptp4A3	protein tyrosine phosphatase 4A3
Robo	roundabout receptor
SEM	standard error of the mean
Shh	sonic hedgehog
SP	substance P
SREC-1	scavenger receptor expressed by endothelial cells-1
SNAP-25	synaptosomal-associated protein, 25 kDa
TAE	tris-acetate-ethylenediaminetetraacetic acid
Tas1r1	taste receptor type 1 member 1
Tas1r2	taste receptor type 1 member 2
Tas1r3	taste receptor type 1 member 3
Tas2r	taste receptor type 2
TRPM5	transient receptor potential cation channel subfamily M, member 5
UMAP	Uuniform manifold approximation and projection
VGLUT	vesicular glutamate transporters
VIP	vasoactive intestinal peptide

1 Introduction

1.1 Structural organization of mouse lower airways and their epithelium

The respiratory system is a hierarchy that is divided into structural and functional elements; the conducting zone and the respiratory zone (Figure 1.1). The conducting zone comprises the airways transporting gases into and out of the lungs. This zone includes the trachea and bronchial divisions until the terminal bronchioles. The respiratory zone consists of the respiratory bronchioles (not well developed in rodents), alveolar ducts, alveolar sacs, and alveoli [1].

The mouse trachea contains 15-18 C-shaped cartilaginous rings located anteriorly, supporting the airway and preventing it from collapsing. The free ends of these rings are connected by a thin fibromuscular membrane. The soft posterior part gives the esophagus the flexibility to expand when food passes through it. The trachea ends at the carina, where it bifurcates into the right and left main bronchi (extrapulmonary bronchi), which still have cartilage. They give rise to approximately six to eight generations of intrapulmonary airways without supporting cartilage. The submucosal glands are limited to the proximal trachea, usually detected between the first 1–8 cartilage rings [1–3].

The cellular composition and structure of the epithelium vary from proximal (tracheal) to distal (bronchial) airways. In mice, the trachea and mainstem bronchi are lined by pseudostratified epithelium. The smaller bronchi and bronchioles are lined by a simple epithelium [1, 2, 4].

The lining epithelium of the conducting airways is build up by a mixture of distinct cell types, comprising basal, secretory, ciliated, and rare cells, including pulmonary ionocytes, solitary cholinergic chemosensory cells (tuft or brush cells), solitary neuroendocrine cells, and neuroepithelial bodies (Figure 1.1) [2, 4–6].

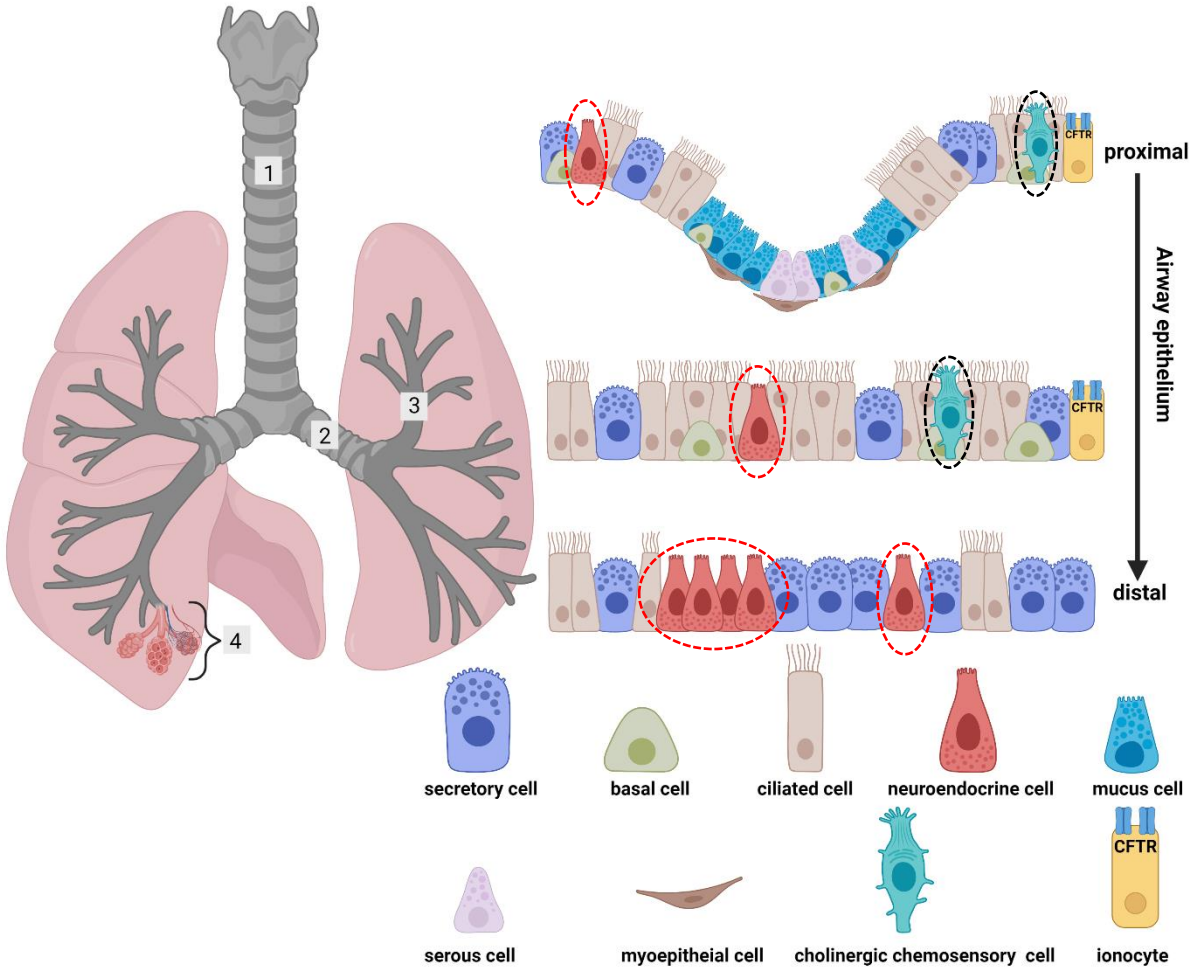

Figure 1.1: Structural organization of mouse lower airways and their epithelium.
Left panel: Anatomy of the lower airways and lungs in the mouse. The conducting zone consists of the trachea (1), which divides into primary bronchi (2); they give rise to approximately six to eight generations of intrapulmonary airways (3). The respiratory zone is represented by (4). Right panel shows the different types of epithelial cells and the change in the conducting airway epithelium from proximal to distal. Submucosal glands are only present in the proximal part of the trachea. Solitary neuroendocrine cells are dispersed within the epithelium of the trachea and bronchial divisions. Neuroepithelial bodies are located below the tracheal bifurcation (neuroendocrine cells are surrounded by red dotted circles). The cholinergic chemosensory cells (black dotted circles) are dispersed along the lower airway epithelium; their density decreases from proximal to distal (none of them have been noticed in smaller bronchioles or the alveoli). Created with BioRender.com.

1.1.1 Rare epithelial cell types in mouse lower airways

Ionocytes, neuroendocrine and cholinergic chemosensory cells are unique and poorly understood cell populations in the respiratory system.

Ionocytes exhibit particularly high expression of the ion channel CFTR (cystic fibrosis transmembrane regulator) and might be involved in the pathogenesis of cystic fibrosis [5, 6].

Cholinergic chemosensory cells are sentinels of microbial products, initiating protective neural reflexes and local innate immune responses [7–9]. Neuroendocrine cells in the respiratory system represent a cell population with multifunctional tasks. They can play an important role in the physiology and pathobiology of different conditions. They are implicated in airway epithelial regeneration following injury [10–12], may play a role in chemosensation [13–15], mechanosensation [16, 17], and recent works demonstrated their role in immunoregulation [18, 19]. Also, neuroendocrine cells raised clinical interest since they are the predominant cells of origin of highly malignant small cell lung cancer [11, 20–22].

This study focuses on structural and functional aspects regarding these rare chemosensory epithelial cell types in the mouse lower airways, focusing predominantly upon neuroendocrine cells.

1.2 Cholinergic chemosensory cells (tuft/brush) in mouse lower airways

By electron microscopy, Rhodin and Dalham (1956) observed a distinct population of rare non-ciliated columnar epithelial cells scattered across the rat tracheal epithelium. They had brush-like apical projections, and features of their cytoplasm and their organelles varied from the ciliated and goblet cells. They called them brush cells. The brush cell is elongated, has a tapered basal part resting on the basement membrane and has small processes extending from the cell. The cytoplasm of brush cells shows a medium opacity between the faint ciliated cells and opaque goblet cells. The Golgi zone is not very prominent and is located above the nucleus. It contains small mitochondria and bundles of fine fibrils [23].

Similar cells have been identified in mouse trachea. They are elongated flask-shaped or triangular with apical process extending into the lumen. They have one or more basal processes and are similar in morphology to neuroendocrine cells of the trachea [7, 24–26].

These cells are cholinergic expressing the acetylcholine (ACh) synthesizing enzyme, choline acetyltransferase (ChAT) [7, 27], and they can release ACh [9].

The cholinergic chemosensory cells are dispersed along the upper and lower airway epithelium and in the laryngeal and tracheal submucosal glands. The density of cholinergic chemosensory cells decreases from the nasal to the bronchiolar epithelium. They are present in the bronchi and large bronchioles, but at a lower density than in higher airways. In the trachea, they are predominantly localized in the intercartilage regions. No cholinergic chemosensory cells have been noticed in smaller bronchioles or the alveoli [7, 24–26].

The cholinergic chemosensory cells are associated with peptidergic nerve fibers in the upper airways but are not densely innervated in the trachea. There, 5.8% of cholinergic chemosensory

cells receive contacts from $CGRP^+$ (calcitonin gene-related peptide) nerve fibers, while 21.7% of cholinergic chemosensory cells in the trachea are close to non-peptidergic nerve fibers (PGP 9.5^+(protein gene product)/$CGRP^-$) [7, 24, 27]. A portion of cholinergic chemosensory cells are connected to cholinoceptive sensory nerve fibers. They sense bitter substances and bacterial quorum sensing molecule in the airway lining fluid and subsequently release the ACh. This ACh activates nicotinic acetylcholine receptors (nAChRs) on the adjacent sensory nerve fibers, triggering a reduction in the breathing frequency [7, 8].

Tracheal cholinergic chemosensory cells express Tas1r3 (taste receptor type 1 member 3) [6, 24, 27]. Tas1r3 is part of umami (Tas1r1 (taste receptor type 1 member 1)-Tas1r3 heterodimers) and sweet receptors (Tas1r2 (taste receptor type 1 member 2)-Tas1r3 heterodimers) [28]. Additionally, tracheal cholinergic chemosensory cells express receptors of the bitter taste Tas2r (taste receptor type 2) family [6, 7, 27, 29].

They also express elements of taste signal transduction cascade; G protein α-gustducin (GNAT3), phospholipase C isoform β2 (PLC-β2) and calcium-activated monovalent cation channel transient receptor potential cation channel subfamily M, member 5 (TRPM5) [7, 24, 25, 30].

Cholinergic chemosensory cells detect formyl peptides from lung pathogenic bacteria, and the canonical taste transduction signaling pathway finally leads to the release of ACh. This pathway includes a PLC-β2-ITPR3-TRPM5 signaling cascade and utilizes an unknown receptor unrelated to formyl peptide and taste receptors. Acetylcholine activates mucociliary clearance, the main innate defense mechanism in the lower airway, by paracrine cholinergic signaling from cholinergic chemosensory cells to ciliated cells via muscarinic M3 receptors, independent of neuronal pathways [9].

Tracheal cholinergic chemosensory cells are a predominant source of interleukin 25 (IL-25). In addition, they express IL-25 receptor (IL17RB), IL-18, IL-10, C-X-C motif chemokine ligand 12 (CXCL12/stromal cell-derived factor 1) and the enzymes involved in the cysteinyl leukotrienes synthesis. The production of these mediators by these cells suggests a role in airway immune responses [27].

Tracheal cholinergic chemosensory cells in mice are generated prenatally, they appeared at embryonic day (E) 18. Postnatally, the cholinergic chemosensory cells substantially expanded until post-embryonic day 78 [31].

Villin has been used in immunohistochemistry as a marker of brush cells in the mouse trachea. Previous studies have demonstrated that the mouse trachea has at least two types of brush cells. They have comparable cell morphology of apical tuft of villin-immunoreactive microvilli. The

cells of the first type express specific cholinergic chemosensory cell markers (TRPM5 or ChAT), while cells of the second type do not express these specific markers [7, 32]. Additionally, these cell types can be discriminated by their dependence on the transcription factor Pou2f3 (POU domain, class 2, transcription factor 3/ Skn-1). Pou2f3 is required for the development of cholinergic chemosensory cells, but not for the second type [7, 32].

According to villin-immunoreactivity of brush cells, it has been shown that 38% of the brush cells (villin-immunoreactive cells) are TRPM5-positive and 62% are TRPM5-negative [32]. In another study using *ChAT*-eGFP (enhanced green fluorescent protein) mice, 83% of brush cells (villin-immunoreactive cells) are ChAT-positive and 17% are ChAT-negative [7].

The development of TRPM5-positive chemosensory cells is critically dependent on the transcription factor Pou2f3. Genetic deletion of *Pou2f3* results in general absence of TRPM5-positive chemosensory cells [32]. In the trachea of *Pou2f3* knockout mice, no TRPM5 and ChAT-immunoreactive cells have been detected, while villin-immunoreactive cells persist. Thus, TRPM5-negative brush cells still developed independent of Pou2f3. In addition, all TRPM5 chemosensory brush cells in other organs like the alimentary tract, pancreatic duct, urethra, thymus, and auditory tube are absent in *Pou2f3 (Skn-1)* knockout mice, but like the trachea, villin-immunoreactive cells persist in urethra and thymus [32].

Up to this time, the identity and the molecular characterization and function of these rare villin-positive cells remained unknown.

1.3 Villin and advillin

1.3.1 Structure and function of villin

Villin is a specialized microfilament-associated protein, which binds G- and F-actin microfilaments in a calcium-dependent fashion. It is not a major protein associated with microfilaments in all cells, suggesting that proteins with similar biochemical features to villin might also be present in other cells [33–35].

Villin has been detected by immunohistochemistry in the microvilli of the epithelial cells of the intestine and the proximal tubules of the kidney in different species including humans, mice, and rats [35–41]. Villin has been detected also in human embryonic intestinal cells before the formation of microvilli [36, 42].

Villin is an actin modifying protein, it can bundle, sever, cap, and nucleate actin. Based on structural and functional aspects, villin can share similarities with two categories of actin-binding proteins. One category includes proteins involved in actin capping, nucleating, and severing. This group contains repeats of a conserved domain. The smallest proteins of this

category have three conserved domains (S1–S3) and include severin, fragmin, and CapG. Villin, gelsolin, and deseverin consist of six repeats of a conserved domain (S1–S6). The second category, like villin, has a carboxyl-terminal domain (headpiece), and these proteins are likely involved in actin crosslinking. Members of this category are supervillin, advillin, protovillin, and EhABPH (Entamoeba histolytica actin-binding protein homologue) (Figure 1.2) [43–47]. The first domain, S1, is responsible for villin's actin-capping activity, whereas actin nucleating and severing activities require the entire villin core [48]. Villin has at least two F-actin-binding sites to allow adjacent filaments to be bridged, a strong but Ca^{2+}-dependent site in the core [49, 50], and a Ca^{2+}-independent site in the headpiece [51].

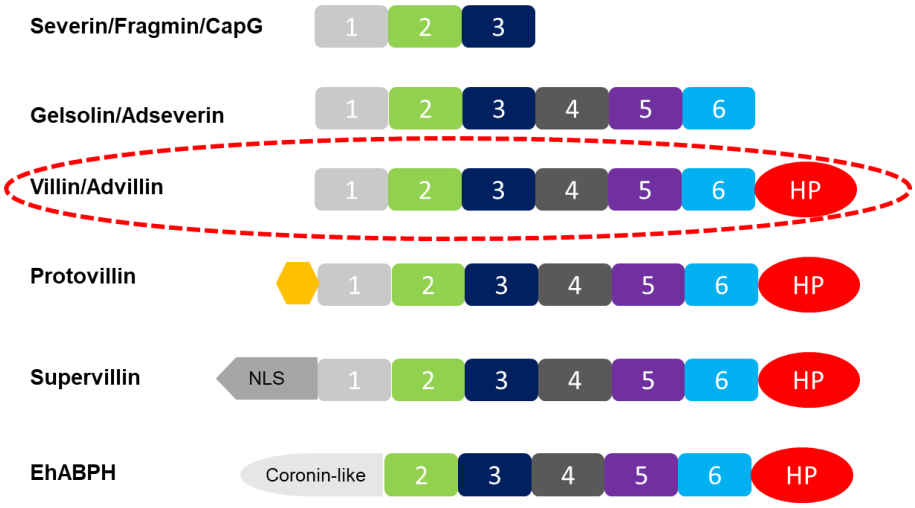

Figure 1.2: Domain structure of the gelsolin/villin family.
The homologous domains of the amino-terminal are numbered 1-6. Severin, fragmin, and CapG are the smallest proteins in this family with three conserved domains (S1–S3). Villin, gelsolin, and deseverin consist of six repeats of a conserved domain (S1–S6). Others, like villin, have carboxyl-terminal domain (headpiece, HP), e.g. supervillin, advillin, protovillin, and EhABPH, but they differ in their core structure. Advillin shares the highest structural and functional similarities with villin.

In villin-deficient mice, the overall assembly and generation of the microvilli are not affected in various absorptive tissues. Mice with villin deficiency are viable and fertile. They have intact microvilli in the intestine, liver bile canaliculi, and proximal tubules in the kidney. However, minor changes have been observed in microvilli ultrastructure. For example, in the small intestine of these mice, the actin bundles in the microvillar core are diffused compared to the central dense actin core in the wild-type. Furthermore, mice with villin deficiency have a thicker and diffused terminal web (situated at the base of the microvilli) compared to the dense, localized filament of the terminal web in the wild-types [52, 53]. In contrast, villin seems to

play a key role in the regulation of the Ca^{2+}-dependent actin fragmentation in physiological or pharmacological conditions [53].

Actin binding to villin is entirely dependent on Ca^{+2} (nucleation, severing, capping, and bundling) [48–51, 54]. Other elements regulate villin interaction with F-actin. For example, tyrosine phosphorylation reduces the actin polymerizing property of villin and enhances its actin-depolymerizing property. Phosphorylation of villin decreases actin nucleation and bundling, but enhances actin severing function. Villin phosphorylation lowers the villin's binding affinity for F-actin. [55]. Tropomyosin, as an actin-binding protein, is contained in the rootlet, but not in the core of the microvillus. It can bind to actin with high affinity and causes up to 30 percent of villin and fimbrin dissociation from the cores. Tropomyosin also reduces the bundling of F-actin by villin [56]. Phosphatidylinositol 4,5-bisphosphate (PIP2) enhances the actin-bundling of villin, but inhibits severing and capping activities of villin [57].

Villin is an epithelial cell-specific anti-apoptotic protein, it maintains mitochondrial integrity during apoptosis. It inhibits caspase-9 and caspase-3, which leads to a delay in the apoptotic response. The anti-apoptotic effect of villin is based on phosphatidylinositol 3-kinase and phosphorylated Akt activation [58].

Villin influences epithelial cell migration, and tyrosine phosphorylation of villin is essential for its role in cell migration [59]. In response to extracellular stimulation, tyrosine-phosphorylated villin associates with phospholipase C-γ1 (PLC-γ1), and consequently, aids in transducing signals involved in the migration of cells. The role of villin in cell migration may suggest a significant function during embryogenesis and cancer cell metastasis [60].

1.3.2 Structure and function of advillin

Advillin shares structural and functional similarities with other proteins in its family, especially villin. Advillin has a six-domain structure like gelsolin and villin. Advillin has a headpiece domain (carboxyl-terminal). Along its full length, advillin shares amino acid homology to villin. Murine villin and advillin share 65% identity at the nucleic acid level, with 75% homology and 59% identity in amino acid sequence. The headpieces of villin and advillin share 44% identity at the nucleic acid level, with 60% homology and 40% identity in amino acid sequence [61]. Functionally, advillin is an actin-binding protein. It has a functional carboxyl-terminal headpiece domain, that can bundle actin like villin. Advillin can nucleate, cap, and sever actin filaments [62].

1.3.3 Villin and advillin in brush cells

Villin and fimbrin antibodies have been considered excellent immunohistochemical markers to identify brush cells at the light microscopic level in the rat respiratory tract and digestive system, particularly the submandibular and parotid glands, pancreatic ducts, and stomach [39, 40]. They labeled the apical and the basolateral margin, making it possible to identify brush cells when the narrow apical tips of the cell are not included in the section. Yet, they are less suitable to identify brush cells in the intestinal epithelium due to the abundant expression of these proteins in the epithelial lining of the intestinal tube [39, 40]. Similarly, villin antibodies have been used as a marker in immunohistochemistry to identify mouse brush cells in the trachea, laryngeal and tracheal glandular ducts, auditory tube, thymus, urethra, and gastrointestinal tract [7, 26, 32, 63–66]. Villin-immunoreactivity also has been detected in human tuft cells of the gastrointestinal and pancreatic-biliary tract [67, 68].

Analysis of tuft cells of the small intestine from mice expressing eGFP under the control of the *Trpm5* promoter showed that brush cells expressed the same amount of villin as other intestinal epithelial cells. However, expression of advillin, another structural protein, was limited to tuft cells [69]. Thus, advillin is strongly and specifically expressed in intestinal brush cells, suggesting the possibility that the formerly published immunostaining of the intestinal brush cells with villin antibodies might have resulted from cross-reactivity with advillin, and advocating advillin as a more specific brush cell marker [69].

Brush cells in the thymus also have been shown to express mRNA of advillin [70]. Also, a very recent publication using non-cross-reacting antibodies showed that tuft cells in the murine intestine do not express villin protein, but advillin protein [62]. In another recent study, using in situ hybridization and immunohistochemistry, villin is expressed by all intestinal epithelial cells at mRNA and the protein level, and by all gall bladder epithelial cells at mRNA level, but only in individual cells at the protein level. Advillin expression, however, is limited to tuft cells at both mRNA and the protein level. *Avil* and *Vil1* mRNAs are co-expressed in intestinal tuft cells (The advillin and villin proteins are encoded by the *Avil and Vil1* genes, respectively) [71]. Cell-type-specific deletion of ChAT in the trachea has been achieved by using an *Avil-Cre* mouse strain to generate $Avil^{cre}$:$ChAT^{fl/fl}$ mice [9], indicating that advillin is a brush cell marker in the trachea.

1.4 Neuroendocrine cells in mouse lower airways

The airway neuroendocrine cell system includes solitary neuroendocrine cells, which are dispersed within the epithelium of the trachea and bronchial tree, and clusters of cells known

as neuroepithelial bodies (NEB) located below the tracheal bifurcation, mainly in intrapulmonary airways. The presence of a large number of dense cored vesicles is the most distinctive characteristic of the neuroendocrine cells. The neuroendocrine cells are associated with nerve fibers and they can produce different amines, neurotransmitters, and neuropeptides which are subjected to species variability [72–76].

Froelich was the first to indicate histologically the existence of clear cells (named "helle Zelle", 1949) in broncho-pulmonary epithelium of several mammals including humans by hematoxylin and eosin staining [77, 78]. Later (1958), Feyrter suggested the presence of endocrine (paracrine) cells in the human airway epithelium; he considered this cell as a part of his "diffuse endocrinic epithelial organ" or "clear cell system". As these cells exhibit some distinct cytochemical and structural properties, for instance, argyrophilic cytoplasm, and the ability to selectively take up amine precursors, they have been counted as members of the APUD (amine precursors uptake and decarboxylation) cell system [79].

Lauweryns and Peuskens referred to cellular corpuscles in the broncho-pulmonary epithelium of the human infant as "neuroepithelial bodies". They are rounded to oval epithelial cell groups, consist of large basal cells containing translucent cytoplasm and several non-ciliated cells located in their apical part. They have argyrophilic cytoplasm mainly at the basal side, and they are associated with free intracorpuscular nerve terminals [80]. Comparable neuroepithelial bodies were documented in the pulmonary respiratory epithelium of several adult mammals such as rabbit, lion, monkey, cat, pig, rat, and mouse. They are located particularly at the bifurcations of the airways [74–76].

The airway epithelium of the mouse contains an extensive system of neuroendocrine cells. They have been also termed enterochromaffin-like cells because of their morphological similarity to gastro-intestinal enterochromaffin cells [81]. They can take up and decarboxylate 3,4-dihydroxyphenylalanine (DOPA) or 5-hydroxytryptophan (5-HTP) to produce dopamine or serotonin, indicating that the cells have a capacity of taking up, synthesizing, and store up the amines upon administration of precursors of amine [76, 81]. They are flask-shaped or triangular cells resting on the basement membrane. They have slender necks extending towards the lumen and short thick processes extending from their basal part. These cells are more frequent in the epithelium of the larynx and decrease in density caudally. In the distal region of the trachea and the main bronchi, they are less frequent [81]. A very distinctive ultrastructural feature of tracheal neuroendocrine cells is the presence of dense core vesicles which are concentrated basally, their diameter measures 80-100 nm [81]. Distally, in the bronchiolar divisions, they are grouped forming clusters of tightly packed columnar cells (neuroepithelial body) consisting of

five to twenty cells in each cluster and mostly lacking processes. In more distal airways, the cells are more rounded [76, 81]. Neuroepithelial bodies have been found through the entire length of the bronchioles until the terminal bronchioles [82].

1.4.1 Neuroendocrine cell development in the mouse lung

At the pseudo-glandular stage of the embryonic lung (E11.5-E16.5 in the mouse), the distribution patterns of epithelial cells in the lung are determined, airway branching morphogenesis occurs, and a population of multipotent epithelial progenitors is comprising the terminal buds. Further expansion of the bronchial tree is associated with the formation of lineage-restricted progenitors from descendants of the multipotent progenitor cells, which produce all the differentiated cells, including neuroendocrine cells [83–85]. Solitary cells and those of the neuroepithelial bodies have the same origin as other airway epithelial cells from the sonic hedgehog (Shh) epithelial lineage and do not originate from the neural crest [86]. Neuroendocrine cells are identified by the early marker Ascl1 at late E12.5 to E13.5 at the proximal area in a “salt and pepper” pattern and are not limited to bifurcation points [85, 86] These cells migrate on the basement membrane distally in the direction of the bronchial bifurcation and cluster there, creating nodal neuroepithelial bodies. However, some neuroendocrine cells form clusters at inter-bifurcation sites (internodal neuroepithelial bodies) [85]. Small clusters of neuroendocrine progenitors are found in late E13.5 to E14, whereas at E15.5, large clusters of NE cells are detected [86]. By E15.5–E16, solitary neuroendocrine cells and cells of neuroepithelial bodies express PGP9.5 and CGRP. Neuroepithelial body formation is divided into three developmental stages: neuroendocrine cell selection (E12.5 to E13.5), cluster formation (E13.5 to E15.5), and differentiation (E15.5 onward). Throughout differentiation, PGP9.5-positive nerve fibers make contact and ramify on the neuroepithelial bodies [86]. Notch-Hes1 signaling leads to solitary neuroendocrine cell generation and is necessary to suppress solitary neuroendocrine cell differentiation from their epithelial progenitors [85]. Cluster formation does not take place by the proliferation of neuroendocrine cell progenitors, as neuroendocrine progenitors stop dividing at or shortly after *Ascl1* expression. Solitary neuroendocrine cells temporarily lose epithelial-type cell adhesion during cluster formation but remain associated with the membrane when crawling over and between neighboring epithelial cells to reach cluster areas at the branching point, in a cell migration mode, called slithering [86].

1.4.2 Innervation

Several studies have shown that solitary neuroendocrine cells and neuroepithelial bodies in the airways of different species are connected to nerve fibers [7, 80, 87–89].

In an immunohistochemical study of mouse trachea, adrenergic nerve endings are most abundant in the region of tracheal epithelium which comprises many neuroendocrine cells. These nerve terminals run between epithelial cells and are close to the neuroendocrine cells [81]. Another study revealed that 5.9% of the tracheal solitary neuroendocrine cells in the mouse receive contacts from CGRP-positive nerve fibers, and 21% of them receive nonpeptidergic nerve fibers (PGP 9.5^{+}, $CGRP^{-}$) [7].

Mouse lungs contain many nerve terminals that selectively contact neuroepithelial bodies. Investigation of the origin and neurochemical pattern of contacting nerve fibers demonstrated that at least two distinct populations of nerve terminals can be received. These nerve terminals originate from myelinated vagal sensory nerve fibers: one glutamatergic, expressing vesicular glutamate transporters (VGLUT) and calbindin D-28 (CB) (20% of neuroepithelial bodies), and the second expressing $P2X_2$ and $P2X_3$ ATP receptors (24% of neuroepithelial bodies). Some of the vagal sensory nerve terminals (VGLUT or $P2X_{2/3}$ ATP receptor) that contact the neuroepithelial bodies express markers for cholinergic vesicles (VAChT) [90].

Three different populations of CGRP-positive nerve fibers terminals with and without substance P (SP) expression are observed near neuroepithelial bodies, varicose $CGRP^{+}/SP^{+}$ and delicate $CGRP^{+}/SP^{+}$ or $CGRP^{+}/SP^{-}$ fibers. They are distinct from other vagal sensory nerve fibers. Only the $CGRP^{+}/SP^{+}$ nerve fiber population originates from vagal sensory neurons. Additionally, some nitrergic nerve terminals (nNOS) or vasoactive intestinal peptide-positive (VIP) nerve terminals are found to be associated with the base of neuroepithelial bodies [90].

1.4.3 Functions of neuroendocrine cells

1.4.3.1 Role of neuroendocrine cells in airway epithelial regeneration

Pulmonary neuroendocrine cell proliferation during homeostasis is extremely low [11]. However, it has been shown that neuroepithelial bodies with associated nascent club cells form a special microenvironment for the regeneration of the epithelium of the airway. In response to the depletion of club cells by naphthalene-induced oxidative airway injury, both proliferate and function as progenitor cell populations. Neuroendocrine cells, on the other hand, make a limited contribution to proliferation and repair following ozone-induced airway injury in response to damage to ciliated cells [10]. The proliferating pulmonary neuroendocrine cells after naphthalene injury poses the ability to produce club cells and ciliated cells [11]. These ciliated

cells, however, may originate from the club cells which have been generated from pulmonary neuroendocrine cells [11, 91]. The ablation of pulmonary neuroendocrine cells, however, does not affect the regeneration of club cells, suggesting that in the absence of neuroendocrine cells, club cells can regenerate. In homeostasis or after lung damage, ablated neuroendocrine cells may not be replaced by other types of lung cells [11].

A recent study has been demonstrated that a minor subpopulation of neuroendocrine cells in neuroepithelial body has a stem cell activity (2-4 cells). After severe airway injury, they proliferate to generate neuroendocrine cells. The neuroendocrine stem cells go back to quiescence at the end of the first week. In the next two weeks, one cell deprograms and continues the proliferation to regenerate the injured epithelium around the neuroepithelial body, including club and ciliated cells [12].

1.4.3.2 Role of neuroendocrine cells in chemosensation

The fact that neuroepithelial bodies are densely innervated by vagal sensory neurons led to consider them as sensory airway receptors [92]. The calcium sensing receptor, for instance, was exclusively expressed in neuroepithelial cells of the postnatal mouse lung. This receptor integrates pathophysiological signals and harmonizes the changes in the level of calcium between the extra- and intracellular environment [13]. In addition, NADPH oxidase has been proposed to be an O_2 sensor in the neuroepithelial bodies of the neonatal mouse lungs. In these reports, compared to control mice, the response of neuroepithelial bodies to hypoxia was impeded in oxidase-deficient neonatal mice ($gp91^{phox}$ knockout), suggesting that NADPH oxidase dysfunction inhibits the O_2 sensing ability of the neuroepithelial bodies [14, 15].

1.4.3.3 Role of neuroendocrine cells in mechanosensation

Immunocytochemistry has demonstrated expression of the mechano- and hypoosmosensitive ion channel TRPC5 on the apical surface of neuroepithelial body cells in the mouse lung. However, no TRPC5-immunoreactivity has been observed on surrounding club cells or other epithelial cells in the airway. The mechanosensitive Ca^{2+} channel TRPC5 is directly stimulated by a physiological hypoosmotic stimulation of neuroepithelial body cells, leading to the opening of these channels, accompanied by a rise in intracellular [Ca^{2+}]. They initiate the transduction of mechanosensory signals to the central nervous system through the vagal nerve and using purinergic pathway signaling [16].

It has been shown that the mechanically activated cation channel Piezo2 is expressed in neuroepithelial bodies which are likely to be also innervated by $Piezo2^{+}$ afferent nerve fibers.

This observation suggests the possibility that the neuroepithelial body maybe acts as a mechanosensor and sensing the lung inflation, which is still unclear up to this time [17].

1.4.3.4 Role of neuroendocrine cells in immunoregulation

In the mouse lung, neuroendocrine cells act as airway sensors that provoke immune responses via the release of the neuropeptide CGRP. This function is regulated by *Robo* (roundabout receptor gene). The expression of *Robo* in the lung epithelium is limited to the neuroendocrine cells. *Robo* inactivation results in the inability of neuroendocrine cells to cluster into neuroepithelial bodies and in upregulation of neuropeptides and invasion of immune cells [18] Recent work also identified them as crucial regulators of type 2 immune responses in the airways. Mutant mice lacking neuroendocrine cells due to genetic deficiency of the transcription factor *Ascl1* exhibit severely reduced mucosal type 2 response in models of allergic asthma. In mouse models of allergic airway inflammation, gamma-aminobutyric acid (GABA) released from neuroepithelial bodies induces goblet cell hyperplasia and mucus overproduction. In addition, CGRP released from neuroendocrine cells stimulates group 2 innate lymphoid cells to release IL-5, which in the end recruits eosinophils [19].

1.5 Chemokines

Chemokines are small (8 to 12 kDa) highly conserved proteins. They bind to G protein-coupled receptors (GPCR), seven transmembrane domain receptors, and participate in several biological processes involving chemoattraction, antimicrobial activity, angiogenesis, integrin activation which is involved in leukocyte-endothelial cell communication and adhesion, leukocyte degranulation, and release of inflammatory mediators [47, 93–101].

Structurally, chemokines are characterized by four conserved cysteine residues, forming two disulfide bonds, a covalent bond formed between the first cysteine and the third in the sequence, and another disulfide bond formed between the second and the fourth cysteine. The chemokine family is subclassified based on the local sequence at the first two cysteines into four subfamilies, CXC, CC, (X)C, and CX3C. In the CXC chemokines (α-chemokines), the first two cysteines are separated by one amino acid, while there is no amino acid between these two cysteines in CC chemokines (β-chemokines). In the (X)C subfamily (δ-chemokines), the first and third cysteines are absent. The CX3C subfamily (γ-chemokines) contains three amino acids between the first and the second cysteine (Figure 1.3) [102, 103].

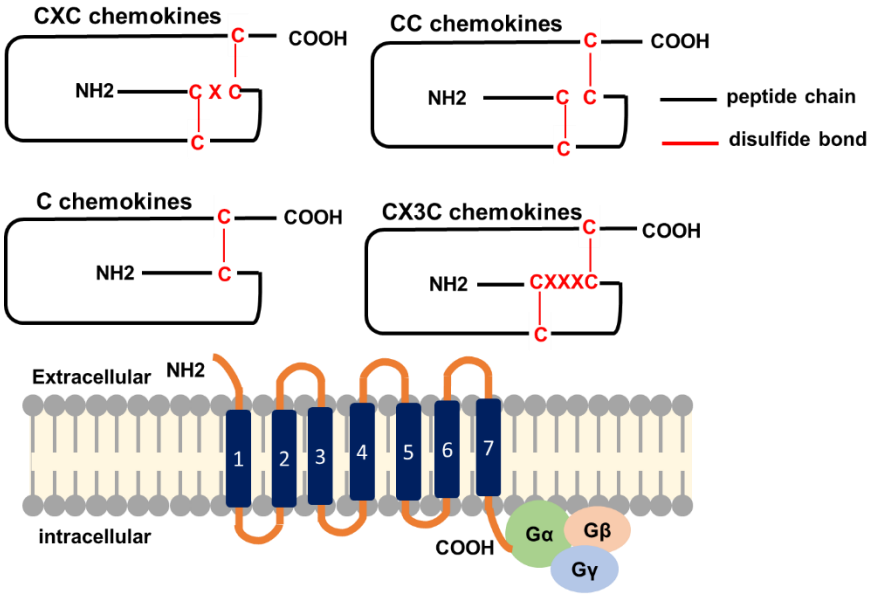

Figure 1.3: Chemokine classification and GPCR structure.
Based on the first two cysteine residues in the N-terminus, chemokines are classified into four subfamilies: In CXC chemokines, the first two cysteines are separated by one amino acid, while there is no amino acid between these two cysteines in CC chemokines. In the C subfamily, the first and third cysteines are absent; the CX3C subfamily contains three amino acids between the first and the second cysteines. They all bind to G protein-coupled receptors (GPCR), seven transmembrane domain receptors.

Chemokines are functionally divided into either homeostatic or inflammatory. In normal organs or tissues, homeostatic chemokines are produced and secreted constitutively, and they regulate the trafficking of cells by guiding cells that express their related GPCR to certain locations. This indicates that homeostatic chemokines are essential for tissues and organs to maintain a steady and active leukocyte arrangement to organize the immune reactions that can be triggered by insults. Examples of homeostatic chemokines are CXCL12, CXCL13, chemokine (C-C motif) ligand 19 (CCL19), and chemokine (C-C motif) ligand 21 (CCL21). However, inflammatory chemokines are not constitutively expressed at high levels in the absence of tissue injury. They are expressed upon stimulation by pro-inflammatory mediators, such as microbial products, tumor necrosis factor, and interferon gamma (IFN-γ). Inflammatory chemokines can be produced in any tissue and by many cells to cause temporary recruitment of inflammatory leukocytes to impaired tissues. Examples of inflammatory chemokines are interleukin 8 (IL-8 or chemokine (C-X-C motif) ligand 8, CXCL8) and chemokine (C-C motif) ligand 2 (CCL2) or monocyte chemoattractant protein 1 (MCP1). However, there are some chemokines with dual functions, like chemokine (C-C motif) ligand 11 (CCL11 or also known as eosinophil

chemotactic protein and eotaxin-1) and chemokine (C-C motif) ligand 22 (CCL22 or macrophage-derived chemokine (MDC)) [102–105].

1.5.1 C-X-C motif ligand 13 (CXCL13)

The G protein-coupled receptor *BLR1* mRNA (Burkitt's Lymphoma Receptor 1) was detected initially (1992) in cell lines of Burkitt's Lymphoma and healthy human lymphatic tissues, but not detected in cell lines of undifferentiated B lymphocytes, T lymphocytes, erythroid, myeloid, monocytic and non-hematopoietic cell lines [106]. Later, mouse *blrl1* mRNA was detected only in tissues and cell lines of the lymphoid lineage and neuronal origin [107]. *Blr1*-deficient mice failed to develop inguinal lymph nodes and had abnormal development of primary follicles and germinal centers in Peyer's patches and spleen, suggesting its involvement in the trafficking and activation of mature B lymphocytes in lymphatic tissues [108]. BLR1 has been identified later as C-X-C chemokine receptor type 5 (CXCR5) [109]. Later (1998), the ligand for BLR1 has been identified as a CXC chemokine and named BCA-1 (B cell–attracting chemokine) [109] or BLC (B lymphocyte chemoattractant) [110]. It is strongly expressed in the follicles of Peyer's patches, spleen and lymph nodes in humans and mice. B lymphocytes are highly attracted by CXCL13, whereas only small numbers of T cells and macrophages are induced to migrate. Thus, the chemokine BCA-1/CXCL13, which is expressed in human and murine lymphoid tissues predominantly by follicular dendritic cells (FDC), is an efficient attractant for B lymphocytes. It binds to the G-protein-coupled receptor CXCR5/BLR1 which is highly expressed by B lymphocytes. Additionally, a subpopulation of $CD4^+$ and $CD8^+$ T helper memory cells in humans and mice express this receptor [108–113].

Several studies have shown that CXCL13 plays a crucial role in bronchus-associated lymphoid tissue (BALT) formation in several pathological conditions, including allergic airway inflammation [114], lung cancer [115, 116], bacterial [117–119] and viral infection [120], cigarette smoking and chronic obstructive pulmonary disease (COPD) [121].

There is evidence that CXCL13 expression is not restricted to the follicular aggregates. For example, in a mouse model of allergic airway inflammation [114] and after bacterial infection [117], CXCL13 is widely upregulated in the lung, particularly in the airway epithelium [114, 117]. The cellular sources in homeostatic conditions, which may participate in the initial steps in these processes before BALT has been formed, are less clear. Some scattered CXCL13-immunoreactive cells have been described in the airway epithelium of non-allergic control mice [114] and non-infected mice [117], but their identity remained undefined.

1.5.2 Role of chemokines in BALT development and maintenance

Bronchus-associated lymphoid tissues are ectopic tertiary lymphoid organs that develop underneath the bronchial epithelium after infection or inflammation [122–124]. The existence of BALT in certain species, such as humans and mice, is usually correlated with pathological conditions [114–121, 125]. However, in other species, like rabbits and rats, BALT is constitutively present [126].

The leukocytes in BALT are organized in two distinct regions, a central follicular B cell zone, and a surrounding and interfollicular T cell zone [127]. B cell follicles include clusters of $IgD^{hi}IgM^{lo}$ mature resting B cells [128]. The B cell follicles also contain some CD8 T cells, dendritic cells (DC), and macrophages [123]. Most plasma cells are found around the follicle's edge or in the T cell region [115, 129]. In the center of some B cell follicles, FDC are found [122]. FDC expresses CXCL13, which is responsible for follicle organization and attraction of B cells and certain types of T cells to the follicles [113, 130]. Although in the absence of CXCL13, B cell areas can still form in *Cxcl13*$^{-/-}$ mice after influenza infection, these areas lack the dense form of true follicles and do not develop FDC [131]. CD21 and the lymphotoxin β receptor (LTβR) are also expressed by FDC [100, 132–134]. In reactive BALT, B cell follicles contain germinal centers, where B cells are dividing fast in reaction to the antigen [122]. Additionally, reactive BALT have activated CD4 T cells (T follicular helper (Tfh)) [127].

T cell zones are mostly located surrounding B cell follicles [127]. CD4 and CD8 T cells are located within T cell zones [124]. Dendritic cells, which are responsible for the presentation of antigen to T cells and maintenance of BALT integrity, are also located in this region [127, 129, 135], in addition to macrophages [136] and plasma cells [129]. High endothelial venules (HEV) and lymphatics are also located in the T cell zone or between the B cell follicle and the T cell zones [115, 122]. Reticular cells are located in T cell areas of BALT. Reticular cells express chemokines that attract T cells and activated DC, like CCL21 and CCL19. Additionally, CCL21 is most predominantly expressed on HEV and lymphatics in BALT [122–124, 131, 137].

Lymphotoxin signaling through its receptors, lymphotoxin β receptors (LTβR), and tumor necrosis factor receptor 1 (TNFR1) on mesenchymal cells, plays a critical role in the signaling pathway involved in the lymphoid organ development. Activation of LTβR leads to production of homeostatic chemokines like CXCL13, CCL19, and CCL21, subsequently recruiting lymphocytes and organizing lymphoid organ development [138, 139]. Lymphotoxin regulates stromal cell chemokine expression, then chemokine signaling on lymphocytes maintains LTαβ expression on their surface. Therefore, the interruption of this positive feedback loop leads to compromised lymphoid organ maintenance and development [123, 140]. The LTβR-signalling

and its association with BALT after lung tissue injury has been demonstrated in lungs from patients with smoking-associated COPD and mice exposed to chronic cigarette smoke. It has been shown that cigarette smoke leads to an increase in LTβR-ligands expression in immune cells, an increase in the non-canonical NF-κB signaling, and LTβR-target gene expression in the lung epithelial cells. Therapeutic inhibition of LTβR-signaling in mice disturbed BALT, and reduced epithelial non-canonical NF-κB activation, with non-canonical NF-κB targets *Cxcl13* and *Ccl19* to be among the most down regulated [141].

The regulation of the expression of the homeostatic chemokines is different between acute and chronic lung inflammation [123]. The previous lymphotoxin signaling is essential for the maintenance of BALT [129]. It is also important for the production of homeostatic chemokines in chronic inflammation models, such as cigarette smoking [142]. However, this signaling is not required to induce homeostatic chemokine expression during BALT development [122, 143]. During BALT development, IL-17 and possibly other inflammatory cytokines (independent of lymphotoxin) regulate the expression of CXCL13 and CCL19. However, the expression of CXCL13 and CCL19 is maintained by lymphotoxin signaling and not by IL-17 when BALT is formed and inflammation is resolved [143].

Chemokines that attract B and T lymphocytes are important for BALT formation. CXCL13 is essential for the formation of proper B cell follicles in BALT. BALT was still developed after influenza infection in *Cxcl13*$^{-/-}$ mice and had distinct areas of B and T cells, HEV, and lymphatics, but the follicles of the B cells only contained loose collections of B cells and no FDC development. In the mouse model, which lacks CCL19 and CCL21 (*plt/plt*), BALT was still formed following influenza infection but with smaller T cell regions and HEV, and large B cell follicles. However, *Cxcl13*$^{-/-}$*/plt/plt* mice following influenza infection failed to develop BALT. The same results were obtained in other studies that used the same deficient mice to study the development and role of BALT in tuberculosis granulomas [118, 123, 131].

BALT can be considered as a functional lymphoid tissue that recognizes airway antigens, initiates local immune responses, facilitates infectious disease clearance, reduces inflammatory responses, and defends against respiratory pathogens. [122, 123, 144–147]. The development of BALT is also connected to a broad range of chronic inflammatory disorders including chronic allergic airway diseases [148], cigarette smoke-induced COPD [121], and lung cancer [115, 116]. Nevertheless, the function of BALT in these disorders is less properly determined as BALT may contribute positively or negatively to the progression of these chronic lung diseases.

1.6 POU domain, class 2, transcription factor 3 (Pou2f3/Skn-1a)

Homeodomain protein Pou2f3/Skn-1a is a transcription factor originally detected in the epidermal keratinocytes and it is associated with their differentiation [149, 150].

The development of TRPM5-positive chemosensory cells is critically dependent on the transcription factor Pou2f3. Genetic deletion of *Pou2f3* results in the general absence of TRPM5-positive chemosensory cells, including TRPM5-positive chemosensory cells in the tracheal epithelium [32]. In oropharyngeal taste buds, Pou2f3/Skn-1a protein is crucial for taste cell development, differentiation, function and maintenance. Pou2f3/Skn-1a is expressed in umami, bitter, sweet taste cells and basal cells of the taste buds. *Pou2f3*–deficient mice have an altered cellular composition of taste buds. There is a complete loss of type II taste cells, resulting in reduced or lacked responses to umami, bitter and sweet tastants. *Pou2f3*–deficient mice have no expression of canonical type II taste cell markers (GNAT3 nor PLCβ2) and the ATP release channel CALHM1 (calcium homeostasis modulator 1) in taste buds. Several studies have shown that this deficiency is also associated with a 30% to a three-time increase of type III taste cell numbers (sour cells) without affecting the number of gustatory neurons that convey the sour taste signals [151–154].

Pou2f3 has been identified as a master regulator for the development of TRPM5-positive chemosensory cells in mice [32]. Furthermore, Pou2f3 has been identified as a master regulator of a tuft cell-like subtype of human small cell lung cancer (SCLC-P subtype) lacking the typical neuroendocrine markers [155]. In mouse models, SCLC-P tumors largely emerge from an unknown origin cell that is neither a neuroendocrine, club nor alveolar cell type II, implying that this variant can originate from a tuft cell [156].

The impact of Pou2f3 on tracheal epithelial development beyond the block of generation of TRPM5-positive cells remained unknown, especially the effect on the other rare epithelial cells like neuroendocrine cells. Type III taste cells (sour taste cells) share some characteristics with neuroendocrine cells. They develop independent from Pou2f3, they share with neuroendocrine cells expression of aromatic L-amino acid decarboxylase (AADC), synaptosomal-associated protein, 25 kDa (SNAP-25), chromogranin A, chromogranin B, and they release serotonin and GABA [151, 157, 158].

1.7 Aim of the study

1. In previous studies, two distinct types of rare cells in the mouse tracheal epithelium displaying an apical tuft of villin-immunoreactive microvilli have been reported [7, 32]. The cells of the first type express cholinergic chemosensory cell-specific markers (TRPM5 or

ChAT), whilst the cells of the second type do not [7, 32]. These two cell types can be further discriminated by their dependence on Pou2f3. This transcription factor is required for the development of cholinergic chemosensory cells, but not for the second type [32]. In addition, the tracheal neuroendocrine cell is another third rare cell type which in light microscopy looks similar in morphology to tracheal cholinergic chemosensory cell [25]. Up to this time, the identity and the molecular characterization and function of the second type of rare villin-positive cells remained unknown (Figure 1.4). Thus, the current study aimed to determine the identity of these villin-positive cells in the murine airway epithelium. Several approaches were used for the assessment of villin expression in the murine airway epithelium, including electron microscopy, immunohistochemistry, RT-PCR, *in silico*-analysis of publicly available sequencing data sets, and immunohistochemical characterization of tissues obtained from *Vil1*-reporter mice.

2. A recent study has shown that tracheal cholinergic chemosensory cells are a predominant source of IL-25, in addition, they express IL-25 receptor (IL17RB), IL-18, IL-10, CXCL12 and the enzymes involved in the cysteinyl leukotrienes synthesis. The production of these mediators by these cells suggests a role in airway immune responses [27]. CXCL13 is another mediator which has an important role in airway immune response and has a crucial role in BALT formation. There is evidence that CXCL13 expression is not restricted to the follicular aggregates. For example, in allergic airway inflammation [114] and after bacterial infection [117], CXCL13 is widely upregulated in the lung, particularly in the airway epithelium [114, 117]. The cellular sources in homeostatic conditions, which may participate in the initial steps in these processes before BALT has been formed, are less clear. Some scattered CXCL13-immunoreactive cells have been described in the airway epithelium of non-allergic control mice [114] and non-infected mice [117], but their identity remained undefined (Figure 1.4). Thus, the present study aimed to assess the CXCL13 expression in the lower airway epithelium in homeostatic condition, focusing upon rare epithelial cell types. The expression of the chemokine CXCL13 (B-cell attracting chemokine) was assessed in the rare epithelial cells by immunohistochemistry, RT-PCR, *in silico*-analysis of publicly available sequencing data sets, and immuno-electron microscopy.

3. The Pou2f3 transcription factor is required for the development of cholinergic chemosensory cells, but not for the villin-immunoreactive cells (second type). Pou2f3 effect on the neuroendocrine cell population needs to be investigated. For example, there is evidence that *Pou2f3*–deficient mice have an altered composition of taste bud cells in addition to complete

loss of TRPM5-positive taste cells (type II taste cells). This deficiency is also associated with an increase of type III taste cells (sour cells) [152, 153]. Comparably, we hypothesized that deficiency in *Pou2f3* also might impact the TRPM5-negative cells in the airway epithelium, focusing upon neuroendocrine cells, which also share some similarities with type III taste cells (Figure 1.4). The density of neuroendocrine cells in the tracheas of *Pou2f3*–deficient mice was evaluated and compared with their controls by an immunohistochemical approach.

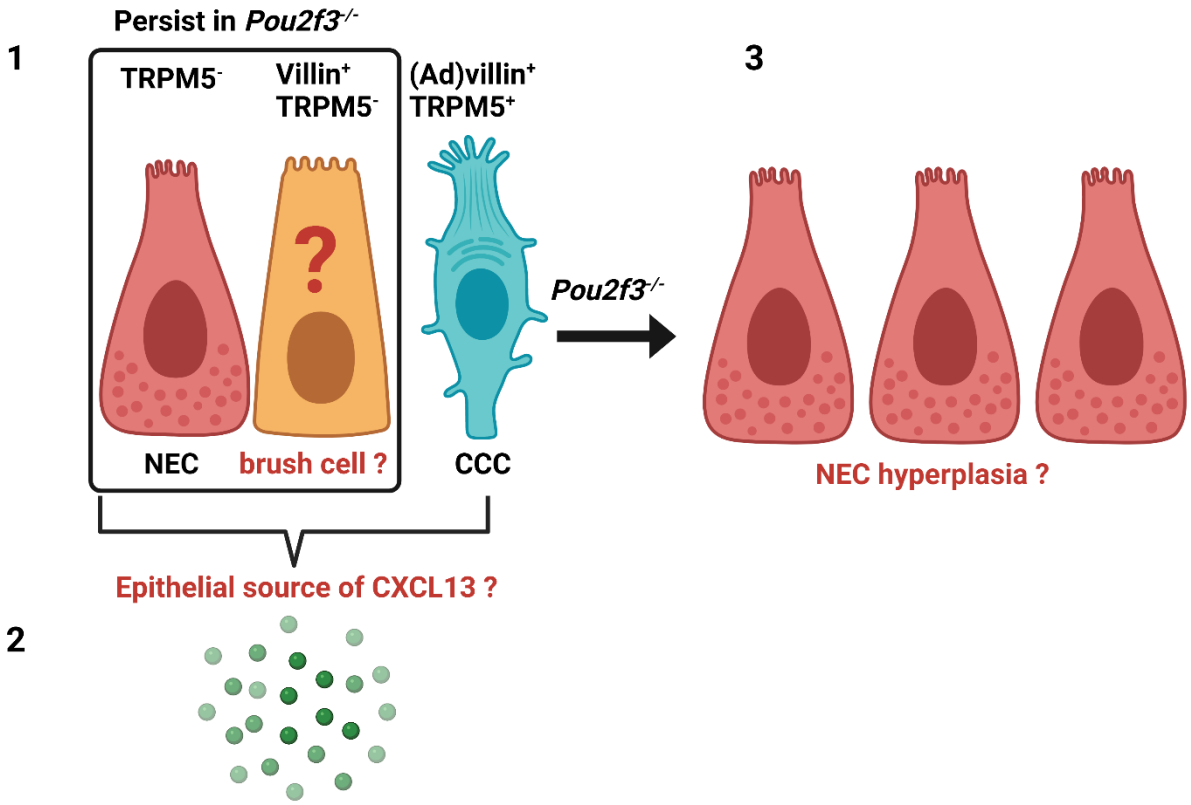

Figure 1.4: Aim of the study.
1. Determine the identity of the villin^{+}/TRPM5^{-} cell. 2. Assess the possible expression of CXCL13 by the rare chemosensory cells in the airway epithelium. 3. Study the impact of Pou2f3 on the neuroendocrine cells in murine tracheal epithelium. NEC: neuroendocrine cell, CCC: cholinergic chemosensory cell. Created with BioRender.com.

2 Materials and Methods

2.1 Animals

Mice were housed at the animal facility of the Justus-Liebig-University Giessen under specific pathogen free (SPF) conditions (10 h dark, 14 h light) with free access to food and water. This study was carried out in accordance with the recommendations of the European Communities Council Directive of 24th November 1986 (86/609/EEC). The protocol was approved by the local authorities, i.e., Regierungspräsidium Giessen, Germany (reference no. 572_M, 571_M, 714_M). Mice at least 12 weeks of age and from both genders were used. Mice were killed by inhalation of an overdose of 5% isoflurane (Abbott, Wiesbaden, Germany) and exsanguination through abdominal blood vessels.

The following animals were used in the experiments:

1. Wild-type C57BL/6Rj mice (Janvier Labs, Le Genest-Saint-Isle, France, Cat#5751862) (n=57).
2. Transgenic mice *ChAT*-eGFP (B6.Cg-Tg(RP23-268L19-EGFP)2Mik/J, Jackson Laboratory, Bar Harbour, USA, Cat# JAX:007902) (n=7):
3. Transgenic mice Pou2f3^{tm1Abek} (*Pou2f3*$^{-/-}$) mice [151] (n=27), the corresponding wild type (*Pou2f3*$^{+/+}$, n=14) and heterozygous (*Pou2f3*$^{+/-}$, n=21).
4. Transgenic mice *Vil1-Cre*$^{+}$*/ROSA*$^{mT/mG}$ (n=6) and *Vil1-Cre*$^{-}$*/ROSA*$^{mT/mG}$ (n=6).

The following mouse lines were used to create *the Vil1-Cre*$^{+}$*/ROSA*$^{mT/mG}$ mouse strain, a double-fluorescent reporter mouse line mT/mG, B6.129(Cg)-Gt(ROSA)26Sortm4(ACTB−tdTomato,−EGFP)Luo/J, (MGI:3716464), The Jackson Laboratory, Bar Harbor, Maine, USA) [159], and a mouse line that expresses Cre-recombinase under the control of the *Vil1* promoter (*Vil1-Cre*, B6.Cg- Tg(*Vil1-cre*)997Gum/J, (MGI:2448639), The Jackson Laboratory, Bar Harbor, Maine, USA) [160] (Figure 2.1).

Hemizygous *Vil1-Cre* mice were bred with the homozygous mT/mG mice. *Vil1-Cre*$^{+}$*/ROSA*$^{mT/mG}$ male and female progeny from these crosses were studied at 12 weeks of age (breeding of the mice was done in Max-Planck-Institute for Heart and Lung Research, Bad Nauheim, Prof. Dr. Stefan Offermanns group and Pharmacological Institute, Philipps University Marburg, Prof. Dr. Thomas Worzfeld group).

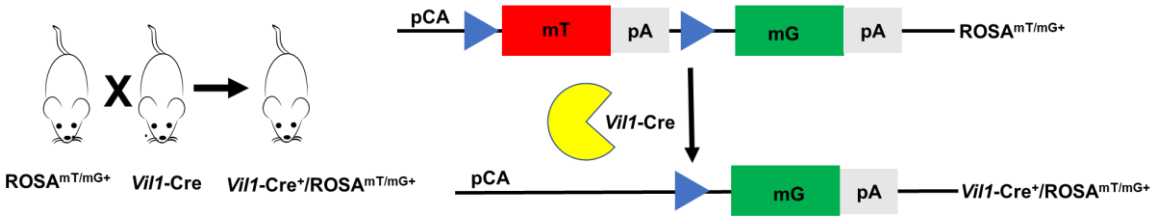

Figure 2.1: Schematic overview of the generation of *Vil1-Cre*$^{+}$*/ROSA*$^{mT/mG}$ mouse strain. ROSA$^{mT/mG}$ consists of a chicken b-actin core promoter with a CMV (cytomegalovirus) enhancer (pCA) driving a *loxP*-flanked coding sequence of membrane-targeted tandem dimer Tomato (mT) resulting in tdTomato expression with membrane localization. Breeding ROSA$^{mT/mG}$ mouse line which contains the double fluorescent reporter, mT and mG, with a mouse line that expresses Cre-recombinase under the control of the villin promoter (*Vil1-Cre*), results in cell-specific excision of mT and allowing the pCA promoter to drive expression of membrane-targeted enhanced green fluorescent protein eGFP (mG). Triangles represent *loxP* target sites for Cre-mediated recombination. PA denotes polyadenylation sequences.

2.1.1 3R Statement

In this study, more than 150 tissue specimens were collected, investigated and analyzed. In order to adhere to the 3R principle (reduction, replacement and refinement) in animal experiments principle [161], the number of animals used for this study was kept to a minimum by taking multiple organs (urethra, trachea, thymus, gall bladder, thyroid gland, intestine, kidney, tongue, spleen and lung) from the same animal and by taking specimens from animals that have been sacrificed for other purposes.

2.2 Tissue preparation

Tracheas were dissected either for whole mount preparation, cryosections, RT-PCR, transmission or scanning electron microscopy. For whole mount, tracheal epithelium RT-PCR and scanning electron microscopy, the trachea was removed and opened by cutting the trachealis muscle longitudinally to expose the lining epithelium. The trachea was then pinned on a piece of wax to align the epithelial layer approximately in the same plane. Then, the samples were either used for RT-PCR or scanning electron microscopy as described later or for whole mount immunostaining (Figure 2.2).

For whole mount immunostaining, samples were immersion fixed overnight at 4°C in Zamboni's fixative composed of 2% formaldehyde (Carl Roth, Karlsruhe, Germany) and 15% picric acid (Merck, Darmstadt, Germany) in 0.1 M phosphate buffer, pH 7.4, then washed in 0.1 M phosphate buffer (5x60 min).

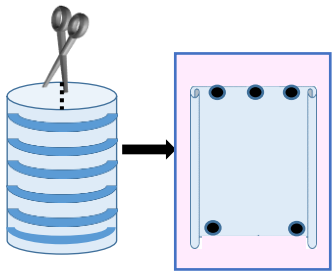

Figure 2.2: Tracheal whole mount preparation.
For whole mount preparation for immunohistochemistry, the trachea was removed and opened by cutting the trachealis muscle longitudinally to expose the lining epithelium. The trachea was then pinned on a piece of wax to align the epithelial layer approximately in the same plane. The same technique was used to prepare the tracheal epithelium for RT-PCR and scanning electron microscopy

Trachea, lung, spleen, and intestine processed for cryosectioning were dissected either freshly or after transcardiac perfusion with Zamboni solution after an initial perfusion with a rinsing solution containing heparin (2 ml/l; 10,000 U; Ratiopharm, Ulm, Germany) and procaine hydrochloride (5 g/l; Merck), pH 7.4 [162] Subsequently, all tissues were immersed in Zamboni's fixative overnight at 4°C, followed by washing steps in 0.1 M phosphate buffer (5x60 min) and overnight incubation for cryoprotection in 18% sucrose (Merck) in 0.1 M phosphate buffer at 4°C. Afterwards, specimens were embedded in OCT cryostat sectioning medium (Sakura Finetek, Staufen, Germany) and frozen in 2-methylbutane (Carl Roth) chilled by liquid nitrogen and stored at -20°C until further processing.

Whole tracheas, lungs and kidney processed for RT-PCR were dissected freshly and followed by the protocol as described in section 2.4.

2.3 Immunohistochemistry

2.3.1 Indirect immunohistochemistry of whole mount preparations

For whole mount tracheal preparation, the tracheas were washed in PBS for 15 min, permeabilization was achieved with 0.3% Triton X-100 (Carl Roth) in PBS (0.005 M phosphate buffer with 0.08 M NaCl, pH 7.4) for 2 hours, then non-specific binding sites were saturated by incubation with a blocking solution (4% normal horse serum (PAA, laboratories, Hessen, Germany) and 1% bovine serum albumin (Thermo Fisher, Massachusetts, USA) in PBS) for 2 hours. All antibodies were diluted in PBS+S (0.005 M phosphate buffer, with 0.15 M NaCl, pH 7.4). The primary antibodies were applied in different combinations overnight at room temperature. Primary antibodies are described in Table 2.1. After a washing step with PBS (5x30 min), the samples were incubated for 2 hours with blocking solution containing 4% normal horse serum and 1% bovine serum albumin in PBS, pH 7.4, then exposed overnight at room temperature to appropriate secondary antibodies listed in Table 2.2. Nuclei were labeled with 4′,6-diamidino-2-phenylindol (DAPI; 1 µg/ml; D9542, Sigma-Aldrich, St. Louis, USA).

Afterwards, samples were washed in PBS (5x30 min), post-fixed in buffered 4% formaldehyde (Carl Roth) for 10 min, and finally washed in PBS at room temperature (5x30 min). Samples were coverslipped with a drop of Mowiol 4–88 (pH 8.6; Merck).

2.3.2 Indirect immunohistochemistry of cryosections

For cryosections, 10 μm thick sections were cut using a microtome (CM-1900 cryostat; Leica), air dried for 1 hour and incubated for 1 hour with blocking solution containing 10% normal horse serum, 0.5% Tween 20 (Sigma-Aldrich), and 0.1% bovine serum albumin in PBS. All antibodies were diluted in PBS+S (0.005 M phosphate buffer, with 0.15 M NaCl, pH 7.4). The primary antibodies were applied in different combinations overnight at room temperature, Primary antibodies are described in Table 2.1. After a washing step with PBS (2x10 min), the sections were incubated for 1 hour at room temperature with secondary antibodies listed in Table 2.2. Nuclei were labeled with DAPI (1 μg/ml; D9542, Sigma-Aldrich). Afterwards, samples were washed in PBS (2x10 min), post-fixed in buffered 4% paraformaldehyde for 10 min, and finally washed in PBS at room temperature (2x10 min). Samples were coverslipped with a drop of Mowiol 4–88 (pH 8.6; Merck) or carbonate-buffered glycerol (pH 8.6, Sigma-Aldrich).

Antigen retrieval protocol was applied only before using the antibody against rabbit villin (Invitrogen, Carlsbad, California, USA, MA5-16408). In this protocol, after the slides air dried, the slides were placed in a cuvette filled with 10% citric acid in PBS, pH 6. Then the cuvette containing the slides was placed in 700 ml water bath and placed in a microwave oven (900 W) until boiling (~ 6 min). Then, the slides were placed again in the microwave oven for another 10 min. The cuvette containing the slides was left to cool for 15 min. Then the slides were washed in PBS (1x5 min).

Antigen	Host	Dilution	Source	Catalogue code
PGP9.5	rabbit, polyclonal	1:4,000	GeneTex, Irvine, USA	GTX109637
UCHL1 (PGP9.5)	chicken, polyclona	1:4,000	Novus Biologicals, Littleton, Colorado, USA	NB110-58872
CXCL13	goat, polyclonal	1:400-800	R&D Systems, Minneapolis, USA	AF470
αCGRP	rabbit, polyclonal	1:20,000	Peninsula Laboratories, San Carlos, USA	T-4032
αCGRP	goat, polyclonal	1:3,000	Biotrend, Cologne, Germany	BT17-2090-07
GFP	chicken, polyclonal	1:2,000-4,000	Novus Biologicals, Littleton, Colorado, USA	NB100-1614
Villin	rabbit, monoclonal	1.400	Invitrogen, Carlsbad, California, USA	MA5-16408
Villin-1 (N-terminal)	rabbit, polyclonal	1:400	Abgent, San Diego, California, USA	AP6774a
TPRM5	rabbit, polyclonal	1:4,000	Kaske et al. [30]	AB-321

Table 2.1: Primary antibodies used in immunofluorescence.

Antigen	Host	Conjugate	Dilution	Source	Catalogue code
rabbit Ig	donkey	Cy3	1:2,000	Chemicon, Limburg, Germany	AP182C
rabbit Ig	donkey	Alexa 488	1:500	Invitrogen, California, Carlsbad, USA	A-21206
rabbit Ig	donkey	Cy5	1:400	Dianova, Hamburg, Germany	711-175-152
chicken IgY	donkey	FITC	1:400	Dianova	703-095-155
chicken IgY	donkey	Cy3	1:2,000	Dianova	703-166-155
chicken IgY	donkey	Cy5	1:400	Dianova	703-175-155
goat Ig	donkey	Alexa 488	1:1000	Molecular Probes, Eugene, Oregon, USA	A-11055
goat Ig	donkey	CF488A	1:1000	Biotium, Hayward, California, USA	B-20016-1
goat Ig	donkey	Cy3	1:1,600	Merck, Kenilworth, New Jersey, USA	AP180C

Table 2.2: Secondary antibodies used in immunofluorescence.

2.3.3 Validation of antibody specificity

The specificity of antibodies was validated by:

1. Omission of primary antibody to control the secondary antibody specificity.
2. For CXCL13 primary antibody, a preabsorption control was done on tracheal cryosections and whole mounts using the immunizing antigen (full length recombinant CXCL13 protein, 470-BC-025, R&D Systems; 10 µg/ml overnight at room temperature), and a parallel control experiment was done without the immunizing antigen. Subsequently, samples were treated as described in the immunostaining protocol.
3. A positive tissue controls, spleen and intestine were used for CXCL13 and villin, respectively.

2.3.4 Microscopy

Samples were evaluated by epifluorescence (Axioplan 2, Zeiss, Oberkochen, Germany) equipped with appropriate filter sets (Table 2.3) and by confocal laser scanning microscopes (LSM 710, Zeiss; FLUOVIEW FV3000, Olympus, Tokyo, Japan; TCS SP8 LIGHTNINING,

Leica; LSM 980-Airyscan 2; Zeiss) equipped with appropriate laser sets (Argon 488, Argon 514, Diode 405, Diode pumped solide state 561 (DPSS) and HeNe 633). Whole trachea overview images were created using the LSM 710 (Zeiss), single pictures were stitched manually using inkscape version 0.92.4 (https://inkscape.org/de/).

Fluorescent dyes	Excitation filter	Emission filter	Dichroic mirror
Cy3	525-560 nm	570-650 nm	555 nm
Cy5	590-650 nm	665-740 nm	655 nm
DAPI	360-370 nm	420-460 nm	400 nm
FITC	460-490 nm	515-550 nm	505 nm

Table 2.3: Filters used in epifluorescence microscope.

2.3.5 Cell counting

For quantitative assessment of single, double or triple immunofluorescence labeling in whole mount tracheal preparations (PGP9.5/CXCL13 (n=40), CGRP/CXCL13 (n=15), PGP9.5/CXCL13/ChAT-eGFP (n=6) or TRPM5 (n=13)), Z-stacks images through the whole thickness of the epithelium were taken with a LSM710 confocal laser scanning microscope and a 25x water immersion objective lens. In total, 30 to 45 image stacks per trachea were obtained by a randomized scheme. The absolute number of immunoreactive cells was quantified manually using ImageJ plugin cell counter. For each trachea, the total count of single and double positive cells and their percentages and average numbers per mm^2 were calculated. The area for the images were measured in mm^2 after setting the appropriate scale using ImageJ.

To quantify CGRP- and CXCL13-immunoreactive epithelial cells in the bronchi and bronchioles, double-labeling with antibodies against CGRP and CXCL13 was performed. Longitudinal sections of the whole lung with the trachea attached were analyzed (5 animals, 3-4 sections each with a distance of at least 50 µm from each other). Counting was done manually using an Axioplan 2 epifluorescence microscope equipped with a 40x objective lens.

To quantify villin- and PGP9.5-immunoreactive epithelial cells in the C57BL/6Rj tracheas, double-labeling with antibodies against villin and PGP9.5 was performed. Coronal sections of the trachea were analyzed (4 animals, 8-10 sections each with a distance of at least 50 µm from each other). Counting was done manually using an Axioplan 2 epifluorescence microscope equipped with a 40x objective lens.

To quantify villin-eGFP and PGP9.5-immunoreactive epithelial cells in the *Vil1-Cre*$^{+}$*/ROSA*$^{mT/mG}$ tracheas, double-labeling with antibodies against GFP (to enhance fluorescence of villin-eGFP^{+} cells) and PGP9.5 was performed. Coronal sections of the trachea were analyzed (4 animals, 6-8 sections each with a distance of at least 50 µm from each other). Counting was done manually using an Axioplan 2 epifluorescence microscope equipped with a 40x objective lens.

2.4 Reverse transcription PCR (RT-PCR)

2.4.1 RNA extraction

Samples from whole trachea (n=2), lung (n=4) and kidney (n=1) from adult C57BL/6 J mice were freshly isolated and soaked in RLT buffer (Qiagen, Hilden, Germany) supplemented with 1% β-mercaptoethanol (Sigma-Aldrich) For tracheal epithelium (n=7 C57BL/6 J mice), the tracheal epithelial layer was abraded using cotton swabs soaked with RLT buffer supplemented with 1% β-mercaptoethanol and purified with a QIA shredder column (Qiagen). Total RNA from all samples was isolated by using the RNeasy kit (Qiagen) according to the manufacturer's instructions. RNAs were stored until further use at -80°C.

2.4.2 Complementary DNA synthesis (cDNA)

For cDNA synthesis (Eppendorf Master Cycler Personal 5332, Hamburg, Germany), 8 µl RNA was incubated with 1 µl 10x DNase reaction buffer and 1 µl DNase (1 U/µl; Invitrogen) for 15 min at 25°C to degrade contaminating DNA. To each sample 1 µl of EDTA (25 mM) was added. After 10 min incubation at 65°C, samples were rapidly cooled for 2 min and 9 µl reaction mixture of (1 µl oligo-dT (50 µM), 1 µl dNTPs (10 mM), 1 µl Superscript RNase H- RT (200 U/µl), 4 µl 5x first-strand buffer, 2 µl dithiothreitol (0.1 M)) was added to each sample. All reagents were from Invitrogen, except dNTPs which were from Qiagen. cDNAs were stored until further use at -20°C.

2.4.3 Polymerase chain reaction (PCR)

PCR (Eppendorf Master Cycler Gradient 5331, Hamburg, Germany) was performed with cDNA samples using primers (Table 2.3) for β-actin (housekeeping gene), *Cxcl13* and *Calca*. The following protocol was used: 1 µl cDNA as template, 2 µl $MgCl_2$ (25 mM), 2.5 µl 10x PCR buffer II, 0.75 µl dNTPs (10 mM), 0.75 µl of each primer (20 pM), 0.25 µl AmpliTaq Gold

DNA polymerase (5 U/µl; all reagents were purchased from Thermo Fisher) and 17.75 µl H_2O. PCR was conducted with the following temperature and time profile: 95°C for 12 min for initial denaturation, followed by 39 cycles at 95°C for 20 s, 60°C for 20 s, and 72°C for 20 s and a final extension at 72 °C for 7 min. β-Actin was used as an efficacy control for PCR, and omission of the reverse transcriptase during cDNA synthesis served as a negative control. Water negative controls were also processed with each reaction to check for the absence of genomic DNA contamination.

Gene	GeneBank accession No	Primer	Product length (bp)
β-actin	NM007393	forward: GTGGGAATGGGTCAGAAGG reverse: GGCATACAGGGACAGCACA,	300
Calca	NM001289444	forward: ATGCAGATGAAAGCCAGGGA reverse: AAGTTGTCCTTCACCACACC	158
Cxcl13	NM018866	forward: AGGCCACGGTATTCTGGAAG reverse: AGCTTGGGGAGTTGAAGACA	250
Vil1	NM009509.2	forward: TGGAAACCGAGACCTTGAGA reverse: TCCACTTTCGGGCTCATAAC	195
Vil1	NM009509.2	forward: GATAGGGAAACATGCCAATGA reverse: TCCACTTTCGGGCTCATAAC	270

Table 2.1: Primers used in RT-PCR.

2.4.4 Gel electrophoresis

Twenty-five µl of the PCR products were mixed with 5 µl loading buffer (1:5) (20 mg Orange G dye (Sigma-Aldrich), 25 ml of glycerol (Merck), 25 ml of 1xTAE buffer (see below)).
The PCR products were subjected to electrophoresis in 2% agarose gel (20 g/l agarose, Biozym GmbH, Wien, Austria) dissolved in Tris-acetate-ethylenediaminetetraacetic acid buffer (1x TAE pH 8) (to prepare stock solution of 50x TAE (242 g/l TRIS (Carl Roth), 57.1 ml/l glacial acetic acid (Merck), 100 ml/l of 0.5 M EDTA (Invitrogen), in 1 l distilled H_2O, pH 8.0). Then, the gel was boiled in microwave oven for ~ 4 min with (900 W) and 20 µl/l of ethidium bromide (1%; Carl Roth) was added. The gel was poured into horizontal electrophoresis in a Horizon 11-14 (peQlab biotechnology (VWR), Radnor, Pennsylvania, USA). After 20 min, 12.5 µl of the PCR products were applied to the gel. A 100 bp DNA ladder (Invitrogen) was run as marker

(6 µl). The electrophoresis was carried out at a voltage of 150 V over 30 min and bands were detected by UV light, using a spectrophotometer (Intas Gel Imager, Germany).

2.5 *In silico*-analysis of published mRNA sequencing data

Previously published gene expression data by Plasschaert and colleagues [5] of murine tracheal epithelial cells (MTECs) from uninjured C57Bl6/J mice were downloaded from SPRING and re-analyzed. Analysis and re-clustering were done using the Seurat R package (version 2.3.4) [164]. Principle component analysis (PCA) was done and UMAP (uniform manifold approximation and projection) was used for non-linear dimensional reduction [165]. Cells were represented in a two-dimensional UMAP plot, and clusters were identified and annotated based on the composition of typical marker genes (done by Dr. Krupali Poharkar, Institute for Anatomy and Cell Biology, Justus Liebig University, Giessen, 35385, Germany). Heat maps were created using gplots function heatmap.2 in R package (https://cran.r-project.org/). The top 200 most expressed genes in neuroendocrine cells were selected. About 60 of them were differentially expressed (fold change >1) compared to other cell types. From these ~60 genes, a heat map was created from $CXCL13^{+}$ and $CXCL13^{-}$ neuroendocrine cells. Another analysis was done by analyzing the original data set again using different selection criteria (fold change >2.5, average TPM value more than 1 in either CXCL13-positive or negative groups or both) and these genes were used to create further heat maps.

2.6 Electron microscopy

2.6.1 Transmission electron microscopy

2.6.1.1 Routine epon embedding

Tracheas were fixed for at least 24 hours in 2% paraformaldehyde and 1.5% glutaraldehyde (Merck) in 0.1 M phosphate buffer (pH 7.4). After fixation, specimens were washed in HEPES buffer 0.15 M, pH 7.4 (35.75 g of 4-(2-hydroxyethyl)-1-piperazineethanesulfonic acid (Carl Roth), in 1 l of distilled water) (5x10 min), osmicated for 2 hours in aqueous 1% osmium tetroxide (Sigma-Aldrich) and washed in distilled water (3x10 min). They were then contrasted in 1% uranyl acetate (Merck) overnight, washed in distilled water (2x15 min), dehydrated in an ascending series of ethanol (30% for 10 min, 50% for 10 min, 70% for 10 min, 90% for 10 min, 96% for 10 min and 100% ethanol, 2x10 min), then samples were transferred into propylene oxide (Merck) as a transitional solvent before being infiltrated with epon (100% ethanol + propylene oxide (1:1, 15 min), then in pure propylene oxide (2x5 min), after that in propylene

oxide + epon (Agar Scientific, Essex, UK) (1:1, 60 min)). Samples were then infiltrated with epon overnight at room temperature, then embedded in epon at 60 °C overnight, and ultrathin sections (80 nm) were cut using an ultramicrotome (Reichert Ultracut E, Leica).

2.6.1.2 Pre-embedding immunoelectron microscopy

For pre-embedding immunoelectron microscopy, the tracheal samples were dissected and immersed in Zamboni's fixative overnight at 4°C, followed by the same protocol which was used in section 2.2. Then, tracheal cryosections of 40 µm thickness were cut (CM-3050S cryostat; Leica).

Floating sections were rinsed in PBS, and unspecific protein binding sites were saturated with 10% normal porcine serum in PBS+S for 1 hour. Sections were then incubated overnight with goat polyclonal antibody to label CXCL13 (1:400 AF470, R&D system) or rabbit polyclonal antibody to label αCGRP (1:20,000; T-4032, Peninsula Laboratory). After a washing step with PBS (3x5 min), the sections were incubated with peroxidase-conjugated pig anti-rabbit Ig (1:100; P0217, Dako, Santa Clara, USA) for 1 hour to detect CGRP or with biotinylated secondary donkey anti-goat IgG (1:400; 705-065-147, Dianova) for 1 hour, followed by a washing step with PBS (2x10 min). Afterwards they were incubated with peroxidase-coupled streptavidin (1:100; 016-030-084, Dianova) for 1 hour to detect the primary CXCL13 antibody. Sections were rinsed in PBS (2x10 min), followed by 0.05 M Tris-HCl buffer (pH 8.6) (2x10 min). Staining was enhanced using a solution containing 15 mg/ml nickel ammonium sulfate (Honeywell, New Jersey, USA) and 0.125 mg/ml 3.3′-diaminobenzidine-hydrochloride (DAB) (Sigma-Aldrich) in 0.05 M Tris-HCl buffer for 10 min before adding H_2O_2 (Fluka) at a final concentration of 0.0023% for additional 45 min. Sections were washed in Tris-HCl buffer (3x5 min), osmicated for 30 min in aqueous 1% osmium tetroxide (Sigma-Aldrich) and washed in distilled water (5x5 min). Specimens were stained overnight *en bloc* in aqueous 1% uranyl acetate (Merck), dehydrated in an ascending series of ethanol (30% (15 min), 50% (15 min), 70% (15 min), 90% (15 min), 96% (15 min) and 100% (2x15 min), then samples were transferred into propylene oxide as a transitional solvent before being infiltrated with epon (100% ethanol + propylene oxide (1:1, 15 min), then in pure propylene oxide (2x15 min), after that in propylene oxide + epon (Agar Scientific, Essex, UK) (1:1, 30 min)). Samples were then infiltrated with epon overnight at room temperature, then embedded flat in epon at 60 °C overnight. Sections containing immunolabeled cells were selected by light microscopy (LEICA

DM750, Wetzlar, Germany) and transferred again into epon block at 60 °C overnight. Ultrathin sections of 80 nm thickness were cut using an ultramicrotome (Reichert Ultracut E, Leica).

2.6.1.2.1 Validation of antibody specificity

1. At electron microscopic level: Omission of primary antibody to control the secondary antibody specificity. Samples were also prepared using the same protocol without primary antibody.
2. At light microscopic level: To further validate the specificity of the biotinylated secondary antibodies used in combination with the CXCL13 primary antibody, 10 µm thick tracheal sections were air dried for 1 hour and unspecific protein binding sites were saturated with 10% normal swine serum in PBS+S for 1 hour. Sections were then incubated overnight either with goat polyclonal antibody to CXCL13 (1:400 AF470, R&D system) and rabbit polyclonal antibody to αCGRP (1:20,000; T-4032, Peninsula Laboratory) or with rabbit polyclonal antibody to αCGRP only. After a washing step with PBS (2x10 min), the sections were incubated with biotinylated donkey anti-goat IgG (1:400; 705-065-147, Dianova) for 1 hour and followed by a washing step with PBS (2x10 min), afterwards they were incubated with Cy3-coupled streptavidin (1:5,000; 016-160-084, Dianova) and donkey anti-rabbit Ig Alexa 488 (1:500, A-21206, Invitrogen). Nuclei were labeled with DAPI (1 µg/ml; D9542, Sigma-Aldrich). Afterwards, samples were washed in PBS (2x10 min), post-fixed in buffered 4% formaldehyde for 10 min, and finally washed in PBS at room temperature (2x10 min). Samples were coverslipped with a drop of carbonate-buffered glycerol (pH 8.6) and evaluated by epifluorescence microscopy (Axioplan 2, Zeiss).

2.6.1.3 Sample visualization and analysis

Ultrathin sections were analyzed using a transmission electron microscope (EM 902 N, Zeiss, Oberkochen, Germany) equipped with a slow-scan 2K CCD camera (TRS, Tröndle, Moorenweis, Germany).

The following cells were evaluated:

1. Cholinergic chemosensory cells, n=9 cells obtained from five mice, all from C57BL/6Rj.
2. Neuroendocrine cells, n=11 cells obtained from seven mice: *Pou2f3*$^{-/-}$=4 mice (eight cells) and C57BL/6Rj=3 mice (three cells).
3. Ciliated cells, n=28 cells obtained from five mice, all from C57BL/6Rj.
4. Secretory cells, n=30 cells obtained from five mice, all from C57BL/6Rj.

For measurements of vesicle and mitochondrial diameter, images were captured with 20,000 magnification. Only vesicles with clear border were considered for measurements. Using Image J software, two central perpendicular axes for each vesicle or two central perpendicular axes mitochondrion were measured.

Vesicle roundness was calculated using the formula: roundness=4*[area]/π*[long axis^2], in this case roundness=short axis diameter/long axis diameter), that is mean 1=ideal circle and 0=elongated shape.

For measurements of microvilli length, width and distance between the microvilli, images were captured with 12,000 magnification and Image J software was used.

For measurements of apical cell width, images were captured with 7,000 magnification and image J software was used.

The evaluated ciliated and secretory cells were chosen randomly, but all of them showed their nucleus and contact the basement membrane.

2.6.2 Scanning electron microscopy

Tracheas from C57BL/6Rj.mice (n=3) were fixed for at least 24 hours in 2% paraformaldehyde and 1.5% glutaraldehyde (Merck) in 0.1 M phosphate buffer (pH 7.4). After fixation, specimens were washed in HEPES buffer 0.15 M, pH 7.4 (3x10 min), osmicated for 2 hours in aqueous 1% osmium tetroxide (Sigma-Aldrich) and washed in distilled water (3x10 min). They were then dehydrated in an ascending series of ethanol (30% (10 min), 50% (10 min), 70% (10 min), 90% (10 min), 96% (10 min) and 100% (2x10 min), then samples were critical point dried by CO_2-treatment (CPD 030 critical point dryer, Bal-Tec, Pfaffikon, Switzerland) and sputtered with gold particles (Polaron E500, UK). Samples were visualized via a Philips XL30 scanning electron microscope.

For measurements of microvilli length and width, images were captured with 50,000 magnification and Image J software was used.

2.7 Statistical analysis

Data are presented as individual data points with median ± interquartile range and mean ± standard error of the mean (SEM). Statistical analyses of data were performed with GraphPad Prism software version 7 (La Jolla, CA, USA).

Normal distribution was analyzed in data sets with a large sample size, using the Kolmogorov-Smirnov and Shapiro-Wilk tests. Depending on the results, normally distributed data were further analyzed with parametric tests: Student’s unpaired t-test or One-Way ANOVA followed

by Tukey multiple comparisons test. Data that did not demonstrate normal distribution or data sets with small size samples were subjected to nonparametric tests: Mann-Whitney U-test or Kruskal-Wallis test followed by Dunn's multiple comparisons test. The Chi-Square test was used to analyze data sets that report frequencies. Differences were considered statistically significant when $p \leq 0.05$.

3 Results

3.1 Villin expression in neuroendocrine cells in the murine lower airways

Villin antibodies have been used in immunohistochemistry as a marker of cholinergic chemosensory cells in the mouse trachea. In these studies, a small population of cells with an apical villin-immunoreactive tuft, which was not immunoreactive to the cholinergic chemosensory cell markers TRPM5 and ChAT was reported. These villin-immunoreactive cells persisted in *Pou2f3* knockout mice, in which cholinergic chemosensory cells were absent [7, 32].

Up to this time, the identity and the molecular characterization and function of these rare villin positive cells remained unknown.

3.1.1 Ultrastructure of rare microvillous epithelial cell types in the murine trachea

To investigate the ultrastructure of the poorly defined villin-immunoreactive cells in the trachea, rare microvillous epithelial cell types in wild-type C57BL/6Rj (n=7 animals) and *Pou2f3*$^{+/-}$ mice (n=1) were compared with those of *Pou2f3*$^{-/-}$ mice (n=5). This approach was chosen on the rationale that neuroendocrine cells can be identified by the presence of basally accumulating dense core vesicles, and cholinergic chemosensory cells (brush cells) are absent in *Pou2f3*$^{-/-}$ but present in *Pou2f3*$^{+/-}$ and wild-type mice (Figure 3.1). Hence, in *Pou2f3*$^{-/-}$ mice, rare microvillous cells without basal accumulation of dense core vesicles should represent this ill-defined villin^{+} cell type. However, cells with neuroendocrine cell features were identified as the only rare microvillous epithelial cell type in *Pou2f3*$^{-/-}$ mice in all evaluated sections (Figure 3.1B), whereas typical cholinergic chemosensory cells (brush cells) were seen in addition to neuroendocrine cells in wild-types (Figure 3.1A).

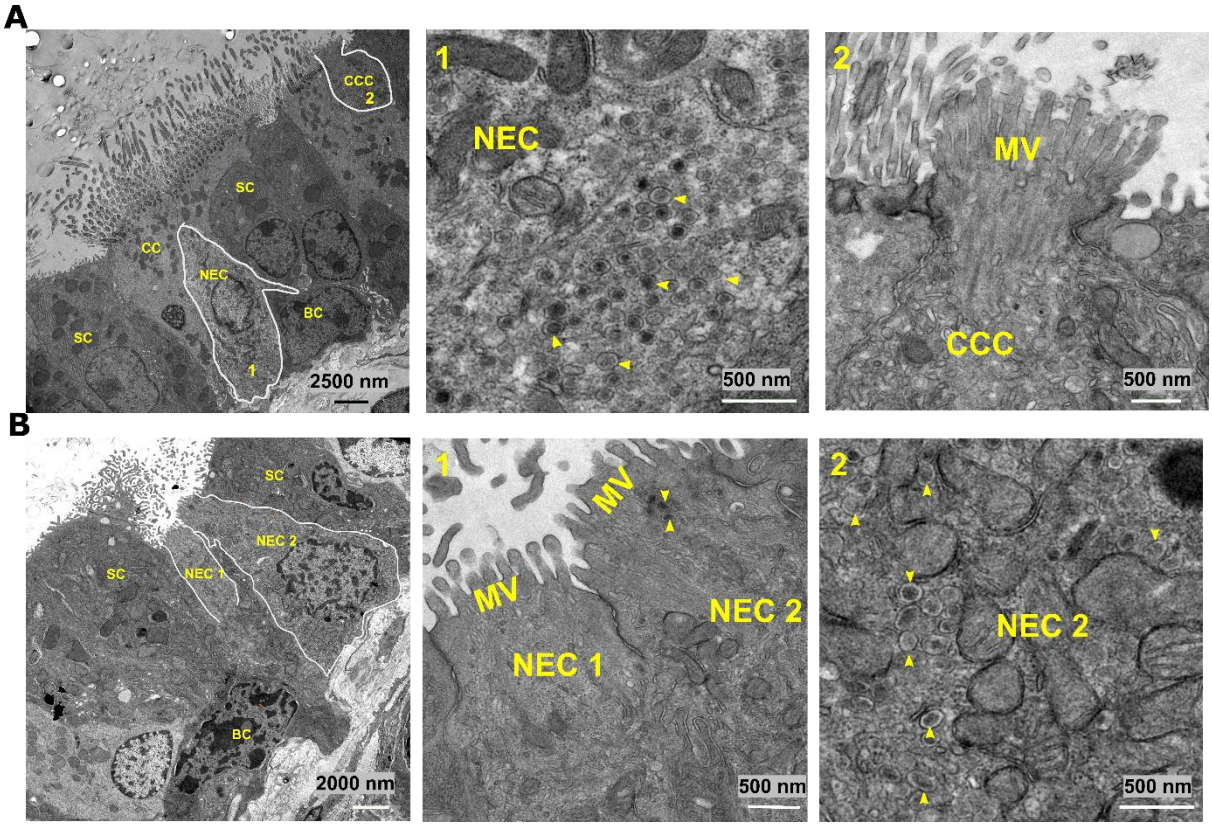

Figure 3.1: Cell types of the tracheal epithelium in a wild-type C57BL/6Rj and a *Pou2f3*$^{-/-}$ mouse.
Transmission electron microscopy. ***(A)*** Showing different cell types of the tracheal epithelium in a wild-type C57BL/6Rj, including ciliated cell (CC), secretory cell (SC), basal cell (BC), neuroendocrine cell (NEC), and cholinergic chemosensory cell (brush cell) (CCC). 1 is a higher magnification of the basal region of NEC, showing the numerous dense core vesicles (arrowheads). 2 is a higher magnification of the apical region of CCC showing their microvilli (MV). ***(B)*** Showing different cell types of the tracheal epithelium in a *Pou2f3*$^{-/-}$ mouse, including secretory cell (SC), basal cell (BC), and two neuroendocrine cells (NEC). 1 is a higher magnification of the apical regions of NEC 1 and NEC 2, showing their microvilli (MV) and some dense core vesicles in the apical region of NEC 2 (arrowheads). 2 is a higher magnification of the basal region of NEC 2, showing the numerous dense core vesicles (arrowheads).

3.1.1.1 Ultrastructure of cholinergic chemosensory cells (brush cells)

In transmission electron microscopy, the cholinergic chemosensory cells were identified as flask-shaped cells. Their nuclei were oval or rounded in shape and located basally (n=9 cells obtained from five mice; all from C57BL/6Rj) (Figures 3.2 and 3.3).

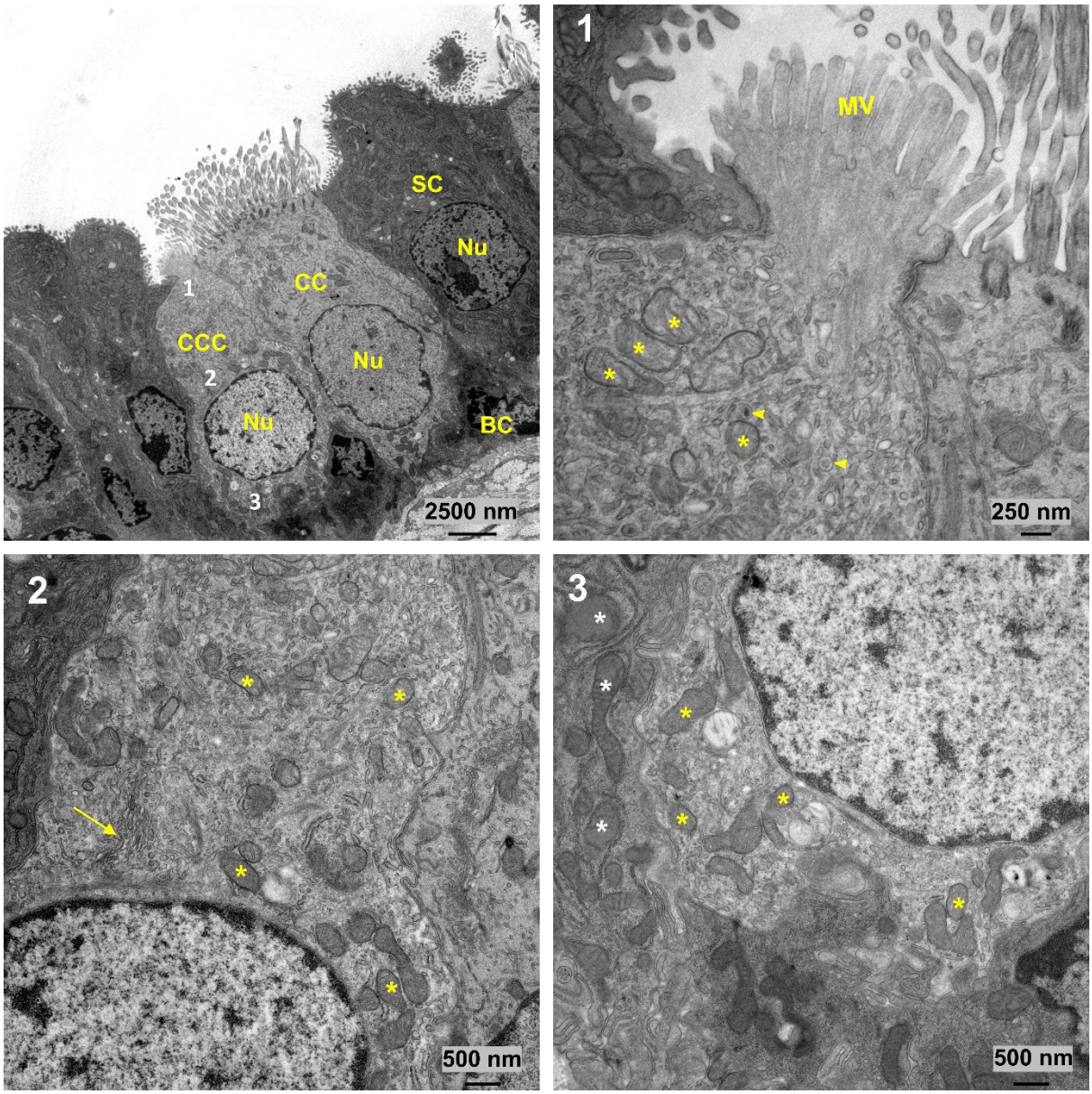

Figure 3.2: Tracheal cholinergic chemosensory cell in a wild-type C57BL/6Rj mouse (1). Transmission electron microscopy, showing a ciliated cell (CC), secretory cells (SC), basal cells (BC), and a cholinergic chemosensory cell (CCC). The CCC has a flask shape with an oval or round basal nucleus (Nu). 1 is a higher magnification of the apical region of the CCC showing a tuft of long, tightly packed microvilli (MV) protruding from its small apical part. Few dense core vesicles are visible (arrowheads) in the apical region; mitochondria are indicated by yellow asterisks. 2 is a higher magnification of the middle region of CCC showing its small mitochondria (yellow asterisks) and perinuclear Golgi apparatus (arrow). 3 is a higher magnification of the basal region of CCC showing its small mitochondria (yellow asterisks) and larger mitochondria in the neighboring secretory cells (white asterisks).

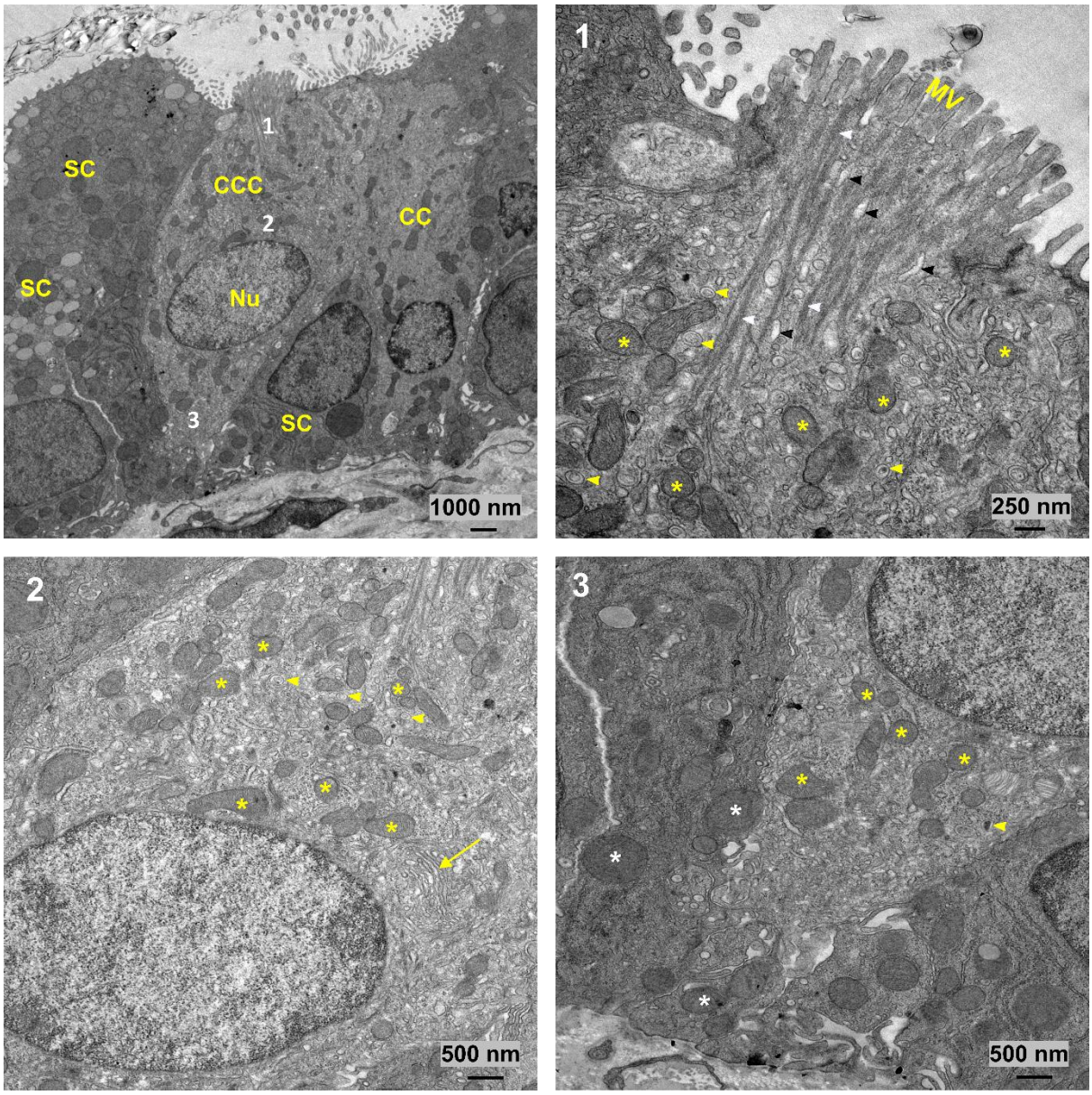

Figure 3.3: Tracheal cholinergic chemosensory cell in a wild-type C57BL/6Rj mouse (2). Transmission electron microscopy, showing secretory cells (SC), a ciliated (CC), and a cholinergic chemosensory cell (CCC). The CCC has a flask shape and an oval to round basal nucleus (Nu). 1 is a higher magnification of the apical region of CCC showing a tuft of long, tightly packed microvilli (MV) protruding from its small apical part. Bundles of microfilaments (white arrowheads) extend from the root of the microvilli into the cytoplasm. Few dense core vesicles (yellow arrowheads) are visible in the apical region. Clear tubulo-vesicular membranous structures are found in the apical region (black arrowheads). Mitochondria are indicated by yellow asterisks. 2 is a higher magnification of the middle region of CCC showing its small mitochondria (yellow asterisks) and perinuclear Golgi apparatus (arrow). Few dense core vesicles are visible (yellow arrowheads). 3 is a higher magnification of the basal region of CCC showing its small mitochondria (yellow asterisks) and larger mitochondria in the neighboring secretory cell (white asterisks). A dense core vesicle is indicated by a yellow arrowhead.

The most distinctive feature was the presence of a tuft of long microvilli protruding from their small apical parts (luminal surface). The average apical cell width was 1206/1443±203 nm (median/mean±SEM, n=9 cells obtained from five C57BL/6Rj mice). Cholinergic chemosensory cell luminal surface was smaller than of ciliated cell (the average apical cell width was 6143/5877±300 nm, median/mean±SEM, n=28 cells obtained from five C57BL/6Rj mice, p=0.0005, Kruskal-Wallis test) and secretory cells (the average apical cell width was 7100/7697±581 nm, median/mean±SEM, n=30 cells obtained from five C57BL/6Rj mice, p<0.0001, Kruskal-Wallis test). However, both neuroendocrine and cholinergic chemosensory cells had a small luminal surface and the difference in the average apical cell width between them was insignificant (the average apical cell width of neuroendocrine cell was 1753/1685±45 nm, median/mean±SEM, n=9 cells obtained from five mice: 4 *Pou2f3*$^{-/-}$ mice (eight cells) and one C57BL/6Rj mouse (one cell), p>0,9999, Kruskal-Wallis test). The average microvillus length of cholinergic chemosensory cells was 624/633±26 nm (median/mean±SEM), the average width was 95/102±5 nm (median/mean±SEM), and these microvilli were tightly packed to each other with an average distance between adjacent microvilli of 23.7/ 24.6±2 nm (median/mean±SEM) (Figures 3.2, 3.3 and 3.4A-D).

Cholinergic chemosensory and neuroendocrine cells had smaller mitochondria compared to ciliated and secretory cells (173 mitochondria were evaluated from nine cholinergic chemosensory cells obtained from five mice; all from C57BL/6Rj, 340 mitochondria from 10 neuroendocrine cells obtained from seven mice; *Pou2f3*$^{-/-}$=4 mice and C57BL/6Rj=3 mice, 300 mitochondria from 28 ciliated cells obtained from five C57BL/6Rj mice, and 312 mitochondria from 30 secretory cells obtained from five C57BL/6Rj mice). The average short axis (mitochondrial diameter) measured 269/283±6 nm in cholinergic chemosensory cells, 190/197±3 nm in neuroendocrine cells, 411/450±9 nm in ciliated cells, and 539/591±14 nm in secretory cells (median/mean±SEM, p<0.0001, Kruskal-Wallis test), while the long axis measured 457/558±25 nm in cholinergic chemosensory cells, 333/417±14 nm in neuroendocrine cells, 731/795±19 nm in ciliated cells, and 919/965±20 nm in secretory cells (median/mean±SEM, p<0.0001, Kruskal-Wallis test). However, neuroendocrine cells had smaller mitochondria compared to cholinergic chemosensory cells. The mitochondrial short axis (mitochondrial diameter) and long axis were significantly shorter than mitochondrial axes in cholinergic chemosensory cells (p<0.0001, Kruskal-Wallis test). (Figures 3.2, 3.3, 3.4E, 3.5 and 3.6).

A few dense core vesicles (0-42/cell, n=9 cells from five mice; all from C57BL/6Rj) were observed mostly in the apical region within the cytoplasm of some cholinergic chemosensory cells, with average short and long central axes diameters of 94/98 and 122/123 nm (median/mean±SEM), respectively (in total 97 vesicles were evaluated, which were found in 7 cells) (Figure 3.4F).

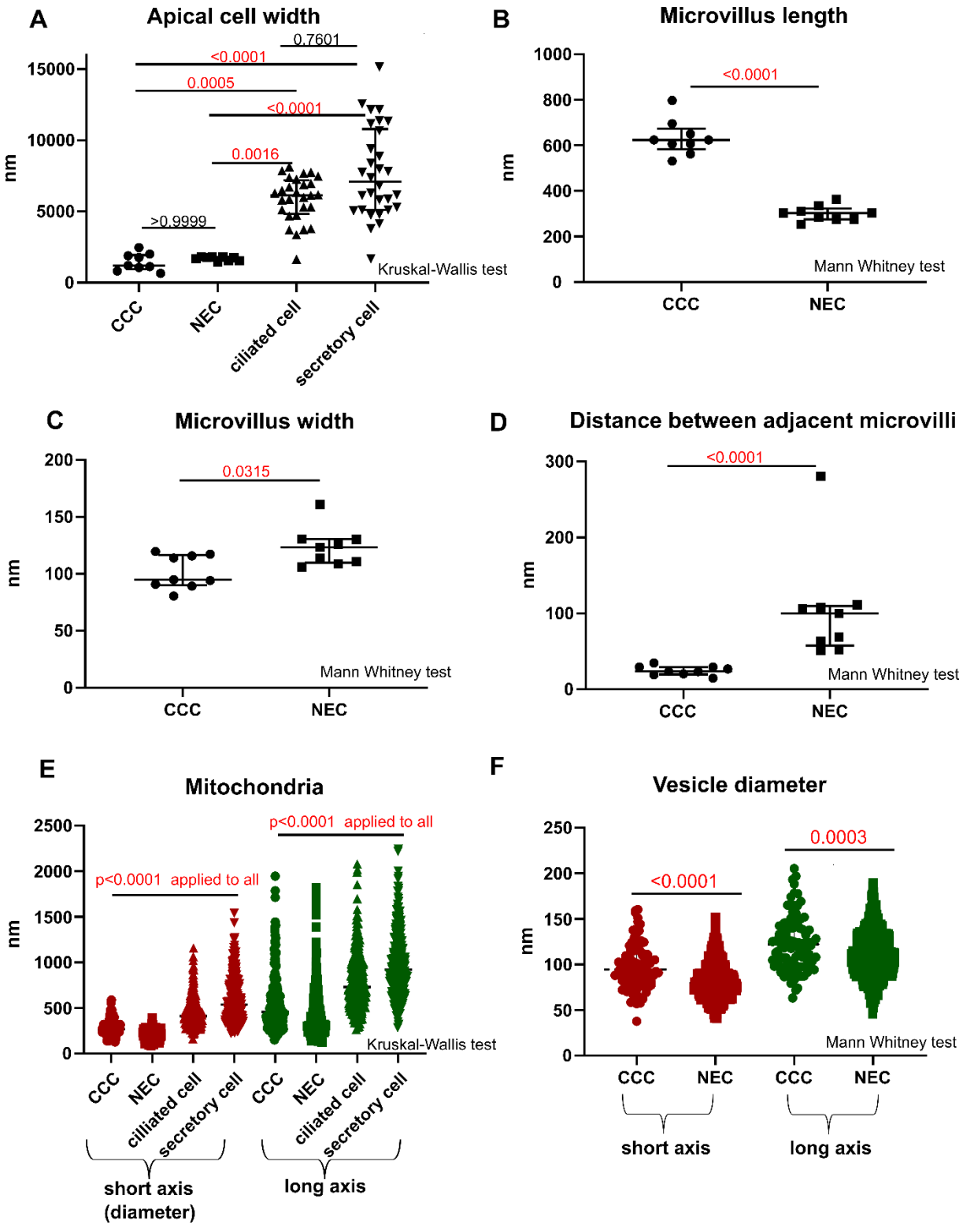

Figure 3.4: Ultrastructural features of tracheal epithelial cell types.
Scatter dot plots with median and interquartile range bars. ***(A)*** Apical cell width, each dot represents one cell. ***(B)*** Microvillus length in cholinergic chemosensory cells (CCC) and neuroendocrine cells (NEC). Each dot represents the average microvillus length of each cell. ***(C)*** Microvillus width in CCC and NEC. Each dot represents the average microvillus width of each cell. ***(D)*** Distance between adjacent microvilli in CCC and NEC. Each dot represents the average distance between adjacent microvilli of each cell. ***(E)*** Mitochondrial diameter (short axis) and long axis measurements in CCC, NEC, ciliated and secretory cells. Each dot represents the measurement of mitochondrial diameter (short axis) or long axis of one mitochondrion, the data were pooled from nine CCC and 10 NEC, 28 ciliated cells and 30 secretory cells. ***(F)*** Vesicle diameter (short and long axes) in CCC and NEC. Each dot represents the measurement of short or long axes of one vesicle, the data were pooled from seven CCC and 10 NEC.

Microfilaments were observed extending from the root of the microvilli into the cytoplasm. In addition, bundles of filaments were often detected in the cytoplasm. Clear tubulo-vesicular membranous structures were found in the apical region (Figures 3.2 and 3.3).

3.1.1.2 Ultrastructure of neuroendocrine cells

Solitary neuroendocrine cells were pyramidal or flask-shaped cells. Their nuclei were irregular to triangular, sometimes with indentation and located basally (n=11 cells, obtained from seven mice: *Pou2f3*$^{-/-}$=4 mice (eight cells) and C57BL/6Rj=3 mice (three cells)) (Figures 3.5 and 3.6).

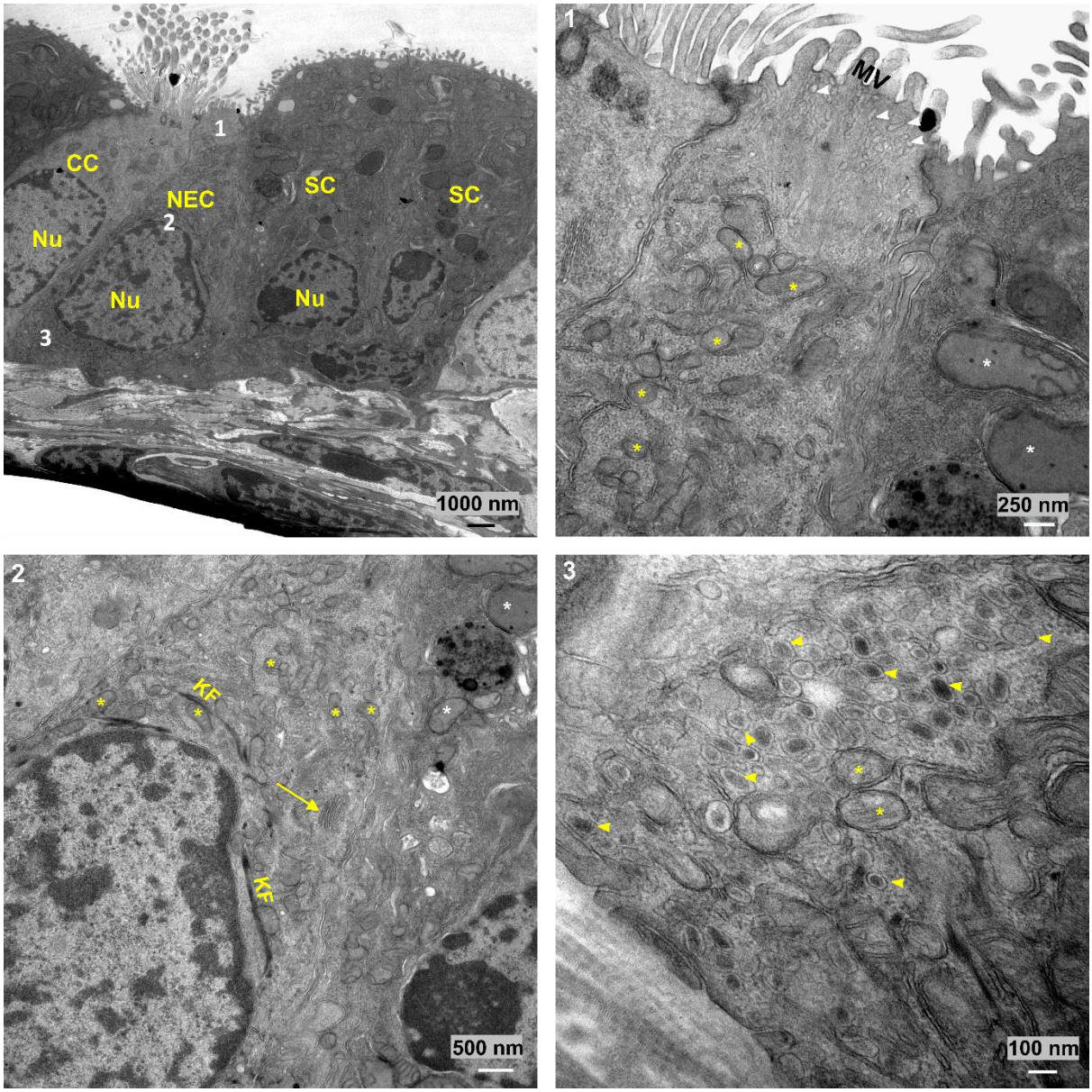

Figure 3.5: Tracheal neuroendocrine cell in a wild-type C57BL/6Rj mouse (1).
Transmission electron microscopy, showing secretory cells (SC), a ciliated cell (CC), and a neuroendocrine cell (NEC). The NEC is pyramidal in shape, has a triangular basal nucleus (Nu). 1 is a higher magnification of the apical region of the NEC, showing short, thick, and spaced microvilli (MV) protruding from its small apical part. Clear tubulo-vesicular membranous structures are found in the apical region (white arrowheads). Mitochondria of the NEC (yellow asterisks) are smaller than those of the neighboring secretory cell (white asterisks); see also panel 2, which represents a higher magnification of the middle region of the NEC. Perinuclear Golgi apparatus (arrow) and keratin filaments (KF) are visible. 3 is a higher magnification of the basal region of the NEC, showing small mitochondria (yellow asterisks) and numerous dense core vesicles (yellow arrowheads) with variable densities.

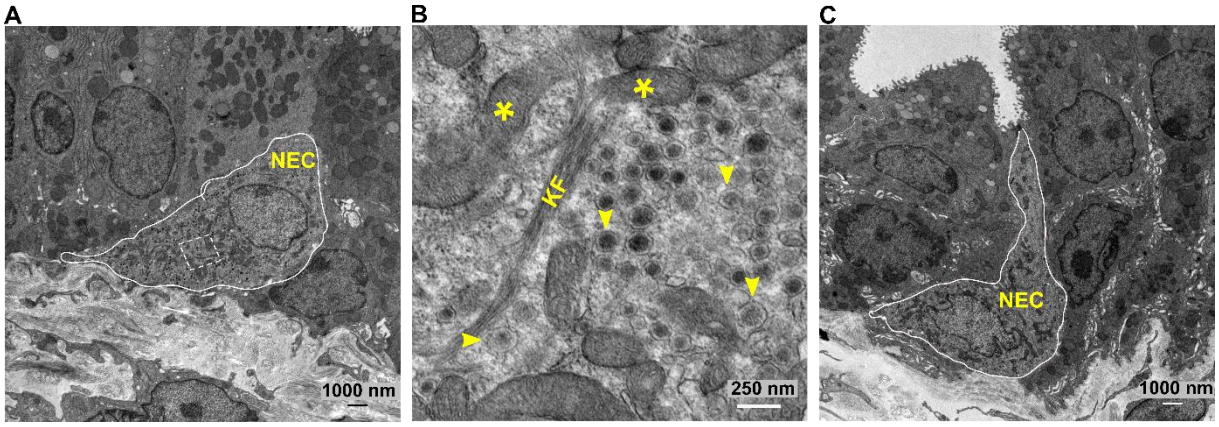

Figure 3.6: Tracheal neuroendocrine cell in a wild-type C57BL/6Rj mouse (2).
Transmission electron microscopy. ***(A)*** Neuroendocrine cell (NEC), not reaching the lumen in this plane of section. ***(B)*** A higher magnification of the region in the white box in A, showing small mitochondria (yellow asterisk), numerous dense core vesicles (yellow arrowheads), and keratin filaments (KF). ***(C)*** The cell was followed in the subsequent sections to see its apical part, but it is still covered partially by the neighboring cells. The nucleus is irregular in shape with indentation.

The apical part (not always visible in sections) was discriminated by its short, thick, and spaced microvilli protruding into the lumen. The average apical cell width was 1753/1685±45 nm (median/mean±SEM, n=9 cells obtained from five mice, *Pou2f3*$^{-/-}$=4 mice (eight cells) and C57BL/6Rj=1 mouse (one cell)). Neuroendocrine cell luminal surface was smaller than of ciliated cell (the average apical cell width was 6143/5877±300 nm, median/mean±SEM, n=28 cells obtained from five C57BL/6Rj mice, p=0.0016, Kruskal-Wallis test) and secretory cells (the average apical cell width was 7100/7697±581 nm, median/mean±SEM, n=30 cells obtained from five C57BL/6Rj mice, p<0.0001, Kruskal-Wallis test). The average microvillus length of neuroendocrine cells was 303/301±11 nm (median/mean±SEM, n=9 cells obtained from five mice, *Pou2f3*$^{-/-}$=4 mice (eight cells) and C57BL/6Rj=1 mouse (one cell)). Microvilli of neuroendocrine cells were shorter than microvilli of cholinergic chemosensory cells (the average microvillus length was 624/633±26 nm, median/mean±SEM, n=9 cells obtained from five C57BL/6Rj mice) (p<0.0001, Mann Whitney test). The average microvillus width of neuroendocrine cells was 123/123±6 nm (median/mean±SEM). Microvilli of neuroendocrine cells were wider than microvilli of cholinergic chemosensory cells (the average microvillus width was 95/102±5 nm, median/mean±SEM) (p=0.0315, Mann Whitney test). Neuroendocrine cell microvilli were spaced from each other with an average distance of 100/105±24 nm (median/mean±SEM), compared to tightly packed microvilli of cholinergic chemosensory cells (an average distance between adjacent microvilli of 23.7/24.6±2 nm, median/mean±SEM) (p<0.0001, Mann Whitney test) (Figures 3.4A-D and 3.5).

Neuroendocrine cell had smaller mitochondria compared to ciliated, secretory, and cholinergic chemosensory cells (section 3.1.1.1), (Figures 3.4E, 3.5 and 3.6).

Bundles of filaments were often detected in the cytoplasm of neuroendocrine cells. Clear tubulo-vesicular membranous structures were found in the apical region. (Figure 3.5).

The most distinctive feature was the presence of numerous vesicles with variable densities (dense core vesicles) which were concentrated in the basal region (Figures 3.5 and 3.6). In total, 930 vesicles were evaluated from 10 cells (obtained from seven mice; *Pou2f3*$^{-/-}$=4 mice (seven cells) and C57BL/6Rj=3 mice (three cells)). The frequency distribution of their short axis diameters was broad and mono-modal (an average of 81 nm, a median of 79 nm, and a range from 40 to 155 nm). The frequency distribution of their long axis diameters was broad and mono-modal, with an average of 111 nm, a median of 108 nm, and a range from 45 nm to 190 nm (Figures 3.4F, 3.7A and 3.7B). The average roundness among all vesicles was 0.75 (1=ideal circle and 0=elongated shape, roundness=4*[area]/π*[long axis^2], in this case roundness=short axis diameter/long axis diameter) (Figure 3.7C). Neuroendocrine cells had smaller vesicles compared to cholinergic chemosensory cells, their average short and long axes in neuroendocrine cells (81 and 111 nm, respectively) were significantly shorter than the corresponding axes in cholinergic chemosensory cell vesicles (98 and 123 nm, respectively) ($p<0.0001$ and $p=0.0003$, respectively, Mann Whitney test) (Figure 3.4F).

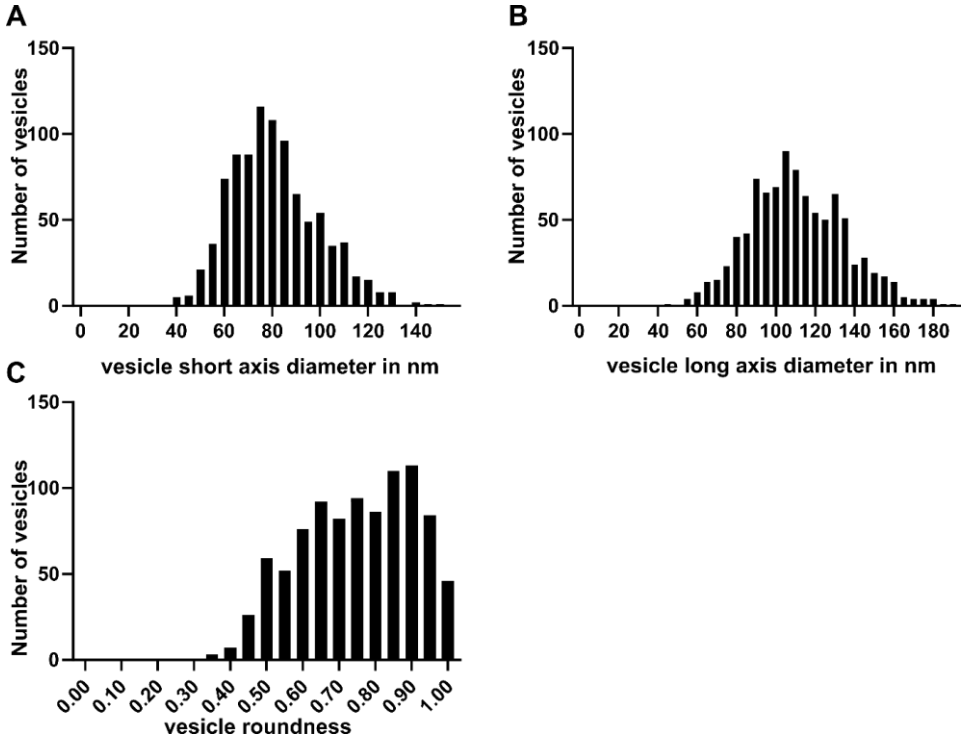

Figure 3.2: Vesicle size and roundness in tracheal neuroendocrine cells.
A total of n=930 vesicles were evaluated, data were pooled from 10 neuroendocrine cells which were obtained from seven mice: *Pou2f3*$^{-/-}$=4 mice (seven cells) and C57BL/6Rj=three mice (three cells).

3.1.1.3 Identification of cholinergic chemosensory (brush) cells and neuroendocrine cells by scanning electron microscopy

In scanning electron microscopy, cholinergic chemosensory cells and neuroendocrine cells were identified based on their luminal surface appearance, which was identified previously by transmission electron microscopy. They were rare, had a small apical surface, and exhibited a characteristic surface morphology, which was different from ciliated and secretory cells. Ciliated cells were identified by their large luminal surface, with cilia and long microvilli. Secretory cells were identified by their large surface, with scattered short microvilli; sometimes their apical surface showed a dome-like appearance (Figure 3.8).

In scanning electron microscopy, cholinergic chemosensory and neuroendocrine cells were differentiated from each other by the appearance of their microvilli. Cholinergic chemosensory cell microvilli appeared longer and thinner compared to the microvilli in neuroendocrine cells. The average microvillus length of cholinergic chemosensory cells was 537/548±22 nm (median/mean±SEM, n=5 cells obtained from three C57BL/6Rj mice), while the average microvillus length of neuroendocrine cells was 251/241±11 nm (median/mean±SEM, n=5 cells

obtained from three C57BL/6Rj mice), (p=0.0079, Mann Whitney test). The average microvillus width of cholinergic chemosensory cells was 78/77±2 nm (median/mean±SEM, n=5 cells), while the average microvillus width of neuroendocrine cells was 102/99±2 nm (median/mean±SEM, n=5 cells) (p=0.0079, Mann Whitney test) (Figure 3.8).

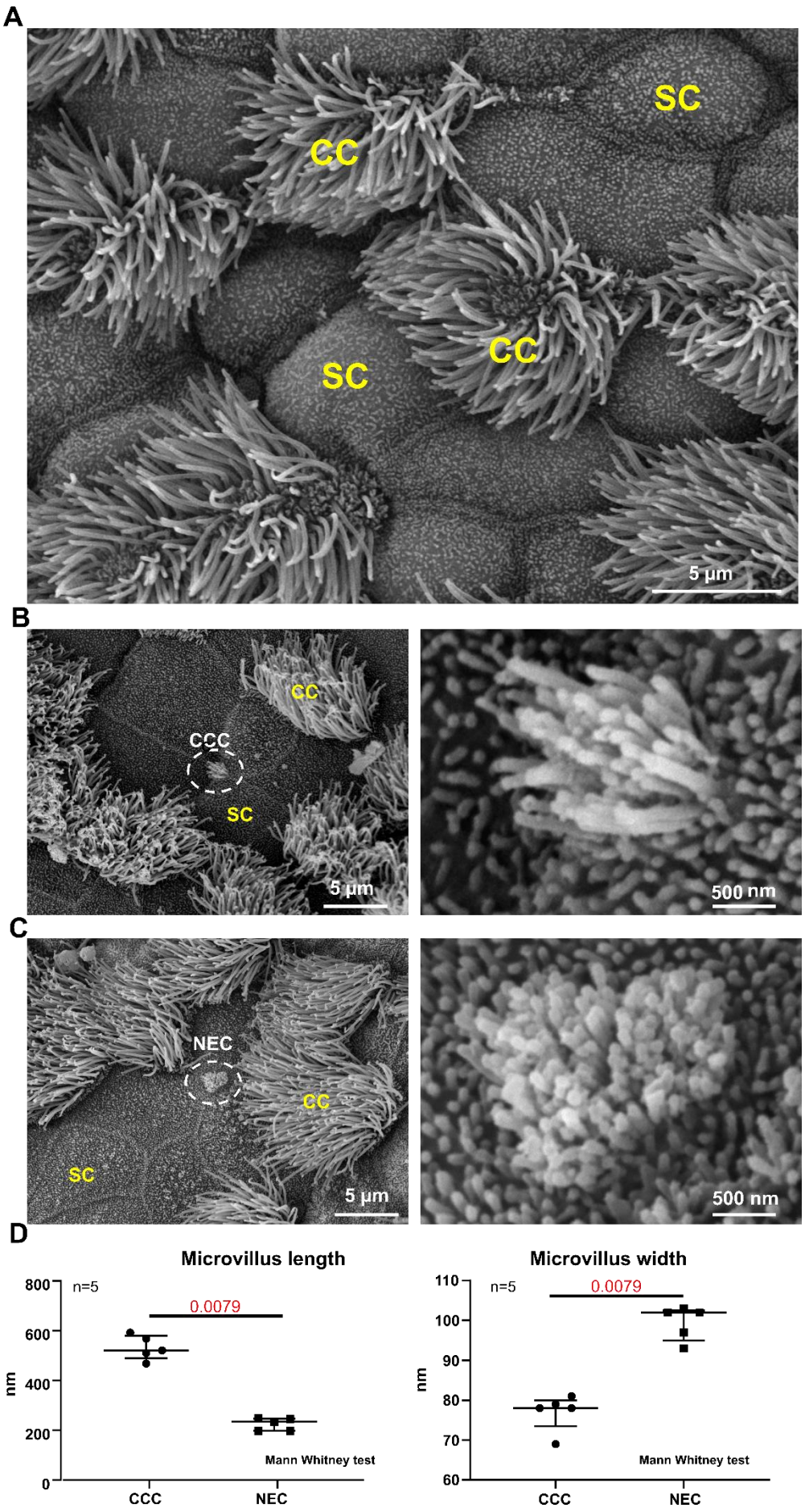
A
SC
CC
CC
SC
5 µm
B
CC
CCC
SC
5 µm
500 nm
C
NEC
CC
SC
5 µm
500 nm
D
Microvillus length
n=5
0.0079
nm
800
600
400
200
0
Mann Whitney test
CCC
NEC
Microvillus width
n=5
0.0079
nm
110
100
90
80
70
60
Mann Whitney test
CCC
NEC

Figure 3.8. Identification of cholinergic chemosensory and neuroendocrine cells in a wild-type C57BL/6Rj mouse by scanning electron microscopy.
(A-C) Scanning electron micrographs of the luminal surface of the tracheal epithelium. ***(A)*** An overview, showing the apical surfaces of ciliated (CC) and secretory cells (SC). ***(B)*** Left panel, apical part of a cholinergic chemosensory cell (CCC, inside the white circle). CC and SC are also present. The right panel is a higher magnification of the microvilli at the CCC surface. ***(C)*** Left panel, apical part of a neuroendocrine cell (NEC, inside the white circle). CC and SC are also present. The right panel is a higher magnification of the microvilli at the NEC surface. The microvilli of the NEC are shorter than those of the CCC. ***(D)*** Scatter dot plots with median and interquartile range bars. The left panel shows the microvillus length in cholinergic chemosensory cells (CCC) and neuroendocrine cells (NEC). Each dot represents the average microvillus length of each cell. The right panel shows the microvillus width in CCC and NEC. Each dot represents the average microvillus width of each cell.

3.1.2 Villin is expressed in a subpopulation of neuroendocrine cells in the murine trachea

3.1.2.1 Immunohistochemistry reveals villin-immunoreactivity in PGP9.5- and CGRP-immunoreactive cells

Based on the previous electron microscopic observation, that the rare microvillous cells in tracheas of *Pou2f3*$^{-/-}$ mice exhibited neuroendocrine cell features, tracheal cryosections from wild-type mice (C57BL/6RJ) were immunolabeled with antibodies against villin and neuroendocrine cell-specific markers (PGP9.5 or CGRP). Immunolabeling revealed co-labeling of villin and PGP9.5 or CGRP. In addition, both villin and PGP9.5 or CGRP single positive cells were also detected (Figures 3.9 and 3.10). The villin-immunoreactive cells were polarized, flask-shaped epithelial cells. Villin-immunoreactivity was in the apical region of the cells (Figures 3.9 and 3.10).

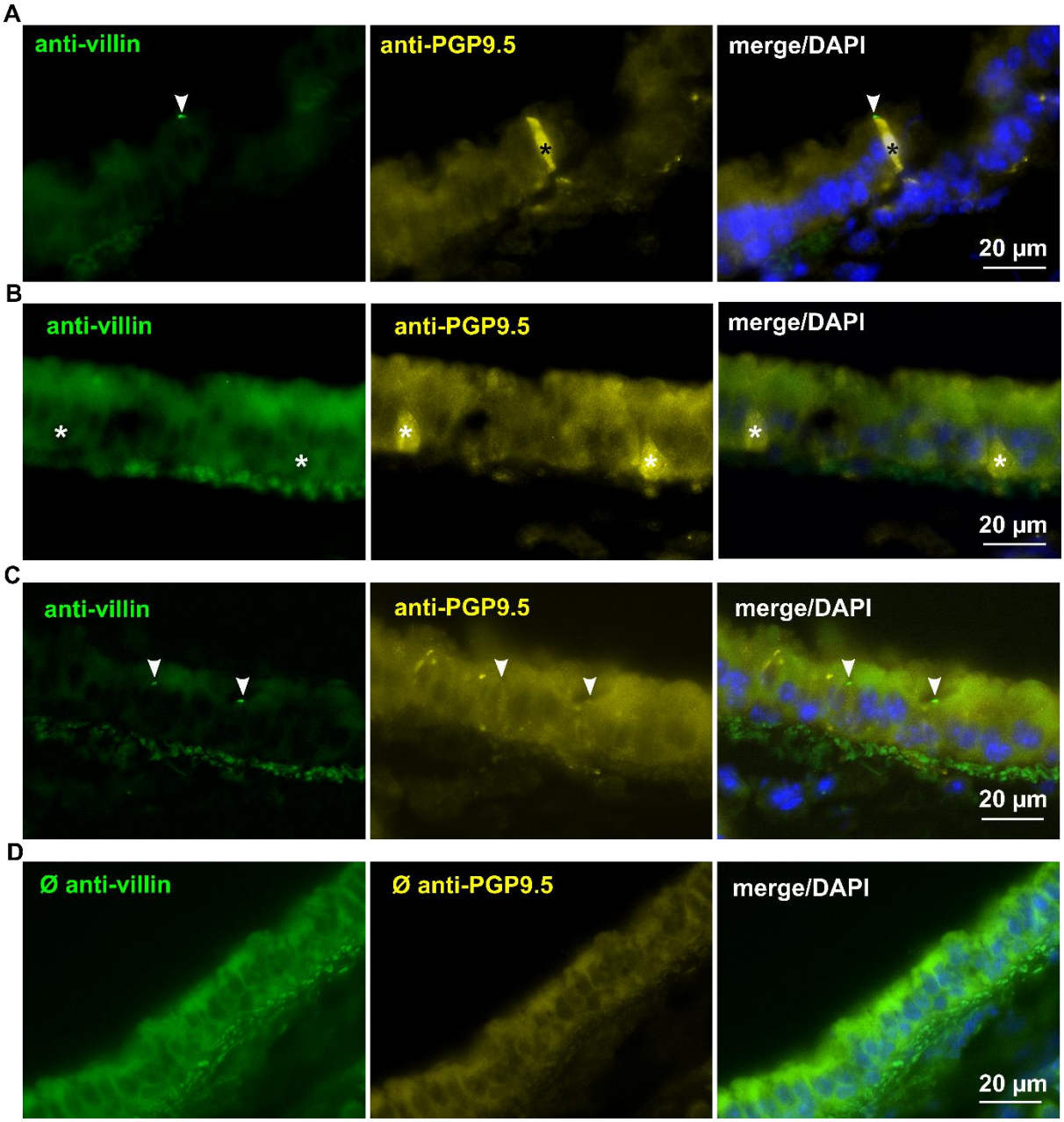

Figure 3.9: Villin- and PGP9.5-immunoreactivity in tracheal epithelium.
(A-D) Immunohistochemistry of tracheal cryosections from a C57BL/6RJ animal. ***(A-C)*** Immunolabeled with antibodies against villin (rabbit, monoclonal villin was used in the figures unless otherwise indicated) and PGP9.5 chicken polyclonal UCHL1 (PGP9.5) was used in this figure. ***(A)*** Shows an epithelial cell double-positive for villin (arrowhead, tip) and PGP9.5 (asterisk, whole cell). ***(B)*** Single PGP9.5^{+} cells (asterisks), not immunoreactive to villin-antibody. ***(C)*** Single villin^{+} cells (arrowheads), not immunoreactive to PGP9.5-antibody. ***(D)*** No immunoreactivity is observed when all primary antibodies were omitted. Images captured with color camera; true colors are shown.

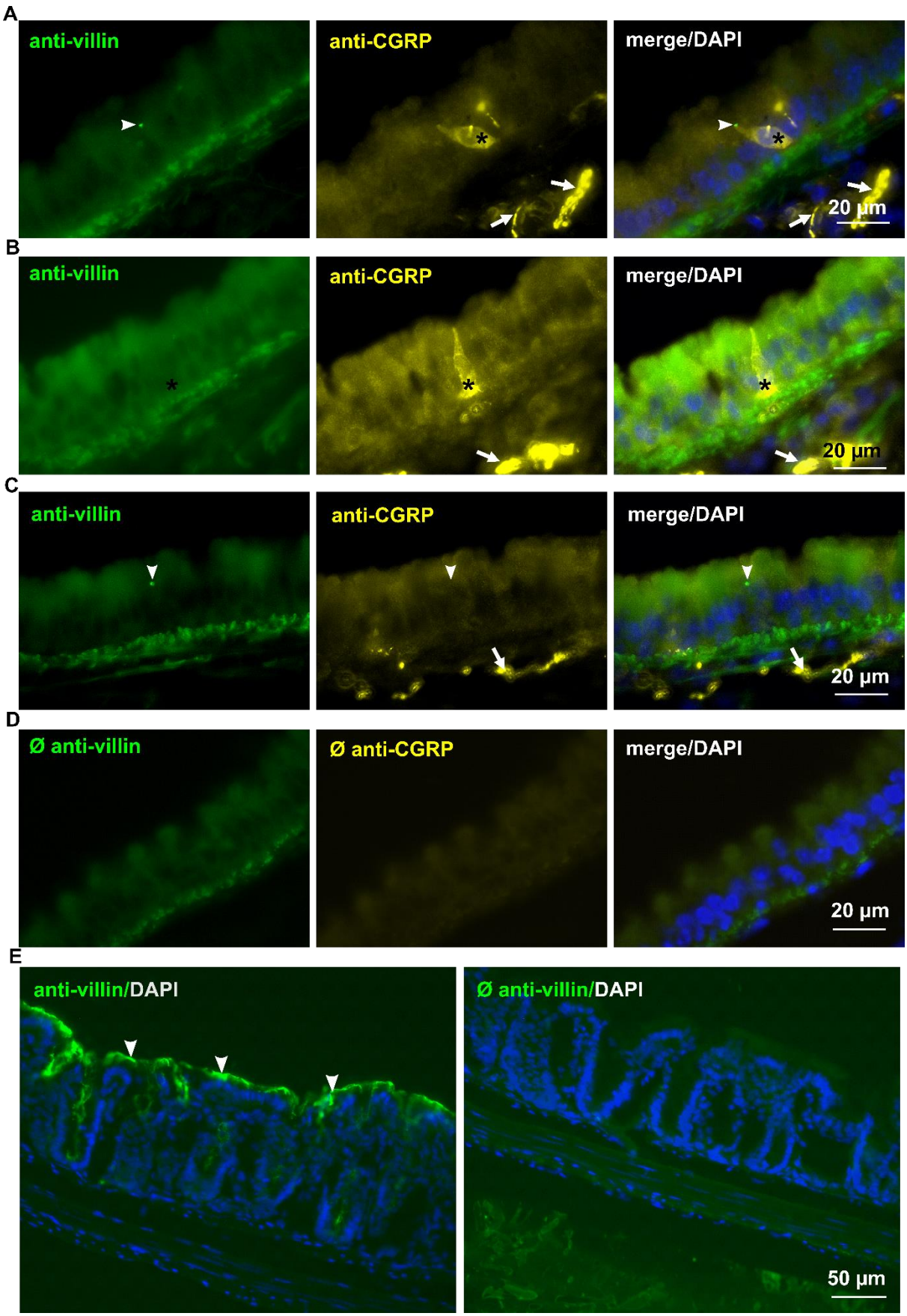

Figure 3.10: Villin- and CGRP-immunoreactivities in tracheal epithelium and villin-positive tissue control.

(A-D) Immunohistochemistry of tracheal cryosections from a C57BL/6RJ animal. ***(A-C)*** Immunolabeled with antibodies against villin and CGRP (goat polyclonal αCGRP). ***(A)*** Shows an epithelial cell double-positive for villin (arrowhead, tip) and CGRP (asterisk, whole cell but the intensity of the staining is concentrated basally). CGRP-immunoreactive nerve fibers are labeled by arrow. ***(B)*** Single $CGRP^+$ cell (asterisk), not immunoreactive to villin antibody. CGRP-immunoreactive nerve fibers are labeled by arrow ***(C)*** Single $villin^+$ cell (arrowhead), not immunoreactive to CGRP antibody. CGRP-immunoreactive nerve fibers are labeled by arrow ***(D)*** No immunoreactivity is observed when all primary antibodies were omitted. ***(E)*** Immunohistochemistry of colon cryosections (C57BL/6RJ; positive control) immunolabeled with the same primary and secondary antibodies used for villin staining in this figure and figures 3.9 and 3.26, showing villin-immunoreactivity of the brush border of colonocytes (arrowheads) (left image). No immunoreactivity is observed when the primary antibody (villin) was omitted (right image). Images captured with color camera; true colors are shown.
.

Tracheal cryosections from *Pou2f3*$^{-/-}$ mice were stained with antibodies against the neuroendocrine cell-specific marker CGRP and villin. Immunolabeling revealed also co-labeling of villin and CGRP (Figure 3.11).

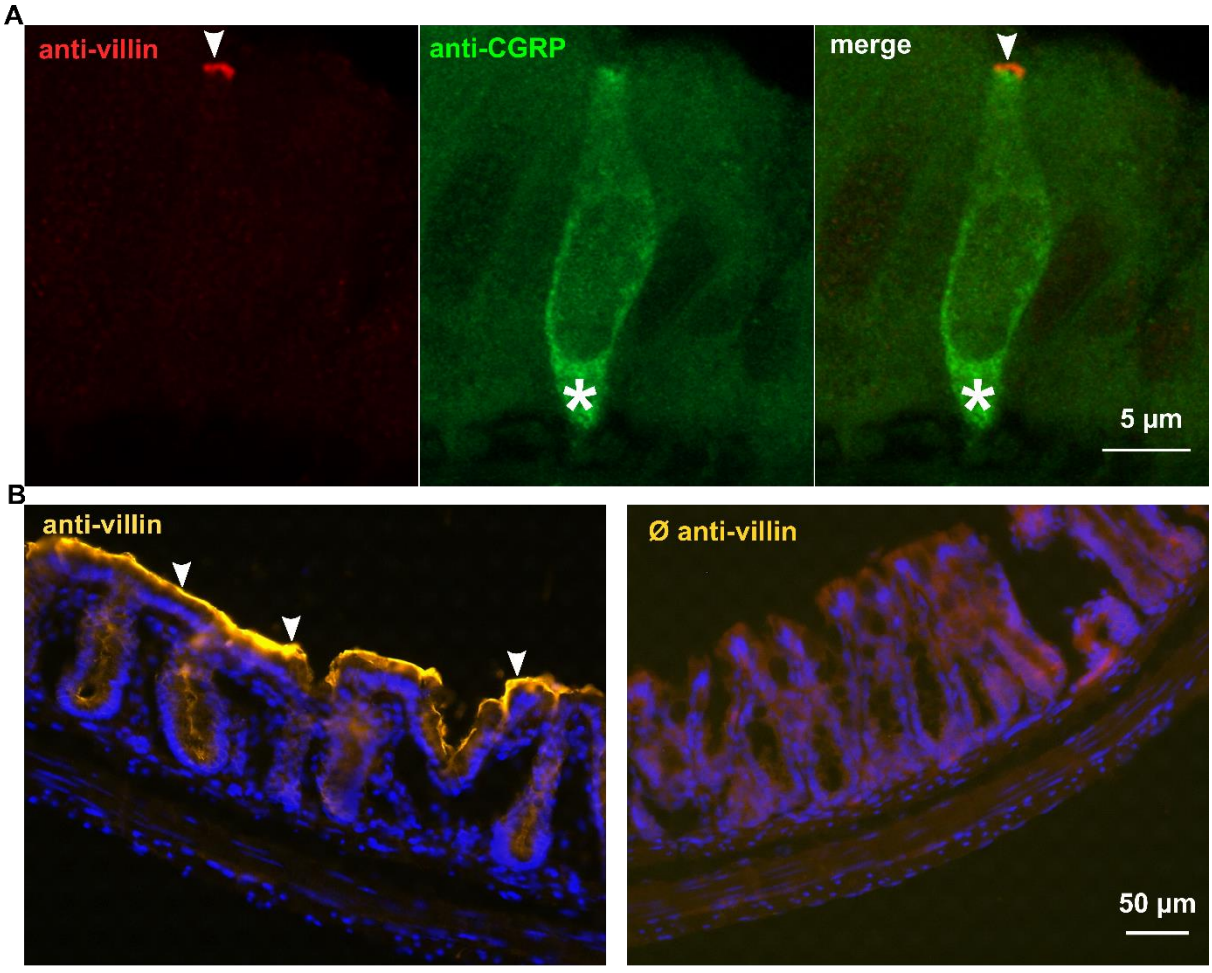

Figure 3.11: Villin-immunoreactivity in *Pou2f3*$^{-/-}$ tracheal epithelium and villin-positive tissue control.
(A) CLSM, double-labeling immunohistochemistry of tracheal cryosection from a *Pou2f3*$^{-/-}$ animal, labeling villin^{+} cells in red and CGRP^{+} in green (goat polyclonal αCGRP); co-labeling of a single epithelial cell for villin at the tip (arrowhead) and the whole cell, but the intensity of the staining was concentrated basally for CGRP (asterisk). Maximum intensity projection of z-stack of confocal optical sections ***(B)*** Immunohistochemistry of colon cryosections from (C57BL/6RJ) (positive control) immunolabeled with the same primary and secondary antibodies used for villin staining in A, showing villin-immunoreactivity of the brush border of colonocytes (arrowheads) (left image). No immunoreactivity is observed when the primary antibody (villin) was omitted (right image), images captured with color camera; true colors are shown. Rabbit polyclonal villin-1 (N-terminal) antibody was used only in this figure.

Different villin antibodies were used in the experiments, which resulted in a similar outcome of co-labeling of villin and neuroendocrine cell markers (Figures 3.9, 3.10 and 3.11). To confirm the specificity of the applied antibody against villin, the colon was used as a positive control for all villin antibodies used in the experiments, showing labeling of the brush border of colonocytes (Figures 3.10E and 3.11B). The omission of the primary antibodies was used to validate specific labeling of the used secondary antibodies (Figures 3.9D, 3.10D, 3.10E and 3.11B).

3.1.2.2 *Vil1* promoter-drives Cre-recombinase expression in solitary tracheal epithelial cells

Hemizygous *Vil1-cre* mice were bred with homozygous *ROSA*$^{mT/mG}$ mice. Tissues from *Vil1-Cre*$^{+}$*/ROSA*$^{mT/mG}$ male and female progeny from these crosses were used for immunohistochemical analysis (n=6). In *Vil1-Cre*$^{+}$*/ROSA*$^{mT/mG}$ mice, all cells express tdTomato except when Cre is expressed, which causes eGFP expression. Tissues from *Vil1-Cre*$^{-}$*/ROSA*$^{mT/mG}$ animals were used as a control (n=6), where all cells express tdTomato and no eGFP expression.

The colon and small intestine were used as a positive control; native eGFP fluorescence was detected in the whole epithelium in *Vil1-Cre*$^{+}$*/ROSA*$^{mT/mG}$ animals. When sections were immunolabeled with an antibody against eGFP and utilizing Cy5-conjugated secondary antibodies, all native eGFP^{+} cells were immunoreactive to eGFP antibody; no additional cells were visible. As expected, in *Vil1-Cre*$^{-}$*/ROSA*$^{mT/mG}$ animals, no eGFP signal was detected with and without eGFP immunolabeling. Red tdTomato-fluorescence (visualized with filters suited for Cy3 or Texas Red) was present in every cell which was not green in *Vil1-Cre*$^{+}$*/ROSA*$^{mT/mG}$ animals. As expected, in *Vil1-Cre*$^{-}$*/ROSA*$^{mT/mG}$ animals, all cells showed red fluorescence using

these filters (Figure 3.12A-D). Double immunolabeling with eGFP and villin antibodies revealed that Cre-recombinase expression had occurred in villin-immunoreactive epithelial cells (Figure 3.12E).

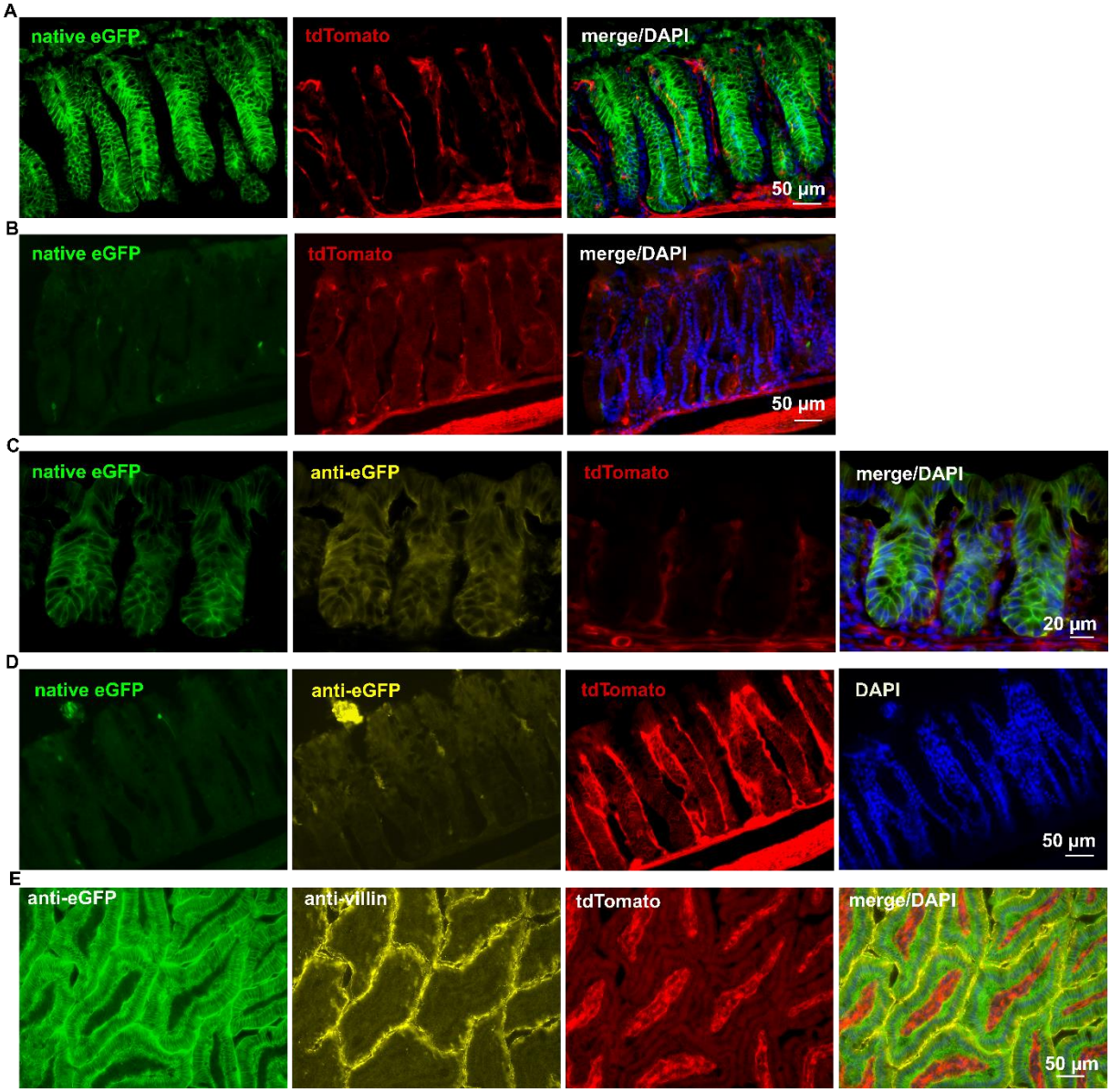

Figure 3.12. The *Vil1* promoter drives Cre-recombinase expression in colonocytes and enterocytes.
(A) Cryosection from a *Vil1-Cre*$^{+}$*/ROSA*$^{mT/mG}$ mouse colon shows native villin-eGFP (green) fluorescence in the epithelium and no tdTomato (red) co-expression. ***(B)*** Cryosection from a *Vil1-Cre*$^{-}$*/ROSA*$^{mT/mG}$ mouse colon shows no native villin-eGFP (green) expression in the epithelium. However, tdTomato (red) is expressed in the whole epithelium. ***(C)*** Immunohistochemistry of a cryosection from a *Vil1-Cre*$^{+}$*/ROSA*$^{mT/mG}$ mouse colon labeled with an antibody against eGFP and utilizing Cy5-conjugated secondary antibodies shows that all native villin-eGFP^{+} (green) cells are immunoreactive to eGFP antibody (yellow); no additional cells are visible. There is no tdTomato (red) co-expression. ***(D)*** Immunohistochemistry of a cryosection from a *Vil1-Cre*$^{-}$*/ROSA*$^{mT/mG}$ mouse colon with an antibody against eGFP and utilizing Cy5-conjugated secondary antibodies shows no native villin-eGFP^{+} cells and no

eGFP-immunoreactivity. However, tdTomato (red) is expressed in the whole epithelium. ***(E)*** Immunohistochemistry of a cryosection from a *Vil1-Cre*$^{+}$*/ROSA*$^{mT/mG}$ mouse duodenum labeled with antibodies against eGFP and villin, showing that Cre-recombinase expression had occurred in villin-immunoreactive epithelial cells. Images captured with monochrome camera; false colors are shown.

In tracheal cryosections from *Vil1-Cre*$^{+}$*/ROSA*$^{mT/mG}$ animals, native eGFP was detected in single rare pyramidal or flask-shaped cells and no eGFP expression was observed outside the epithelium (Figure 3.13A). When sections were immunolabeled with an antibody against eGFP and utilizing Cy5-conjugated secondary antibodies, all native eGFP^{+} cells were immunoreactive to eGFP antibody; no additional cells were visible (Figure 3.13B).

Double immunolabeling with eGFP and villin antibodies revealed that Cre-recombinase expression had occurred in a portion, but not all villin-immunoreactive epithelial cells (Figures 3.13C and 3.13D).

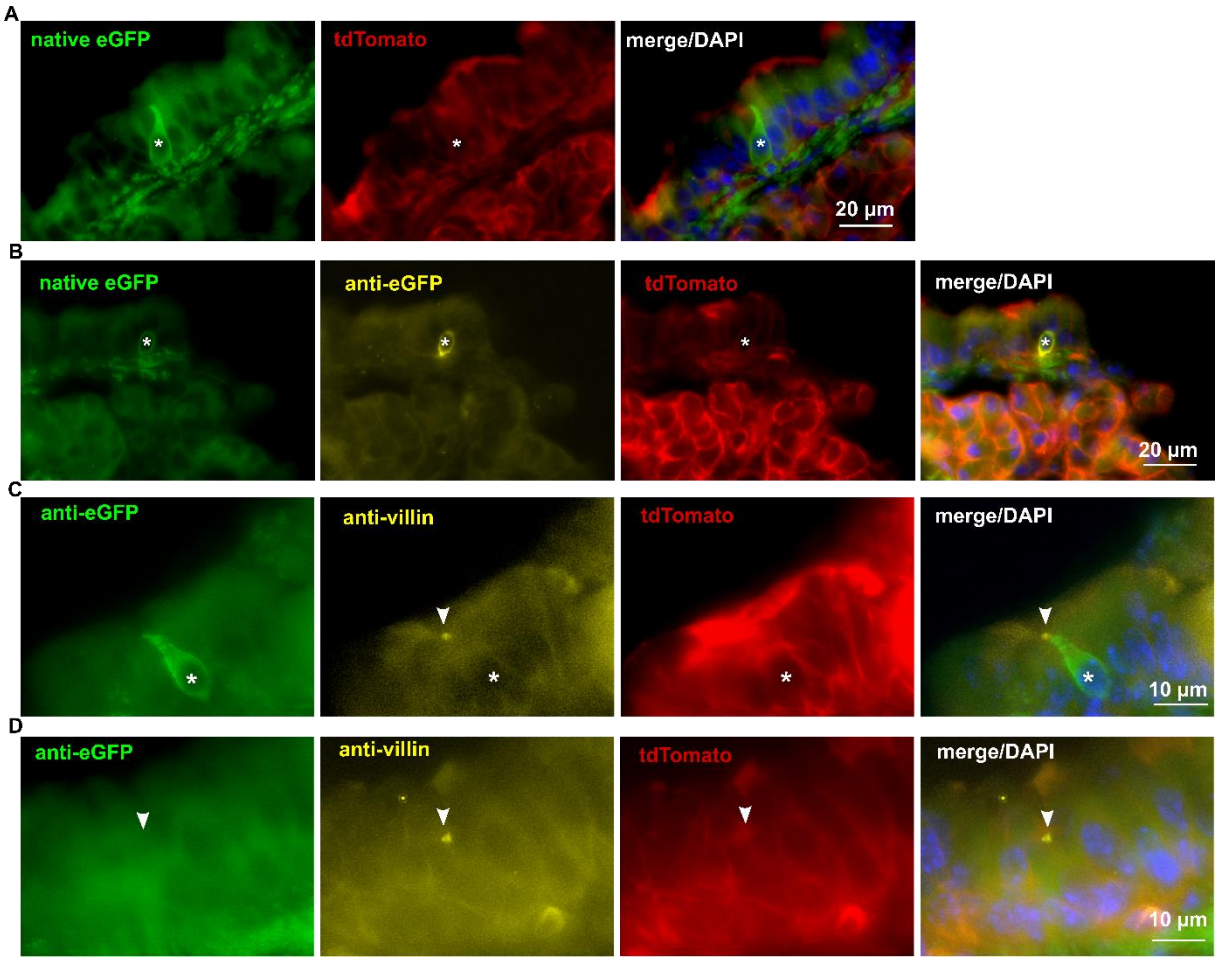

Figure 3.13: The *Vil1* promoter drives Cre-recombinase expression in solitary tracheal epithelial cells.

(A-D) Cryosection from a *Vil1-Cre*$^{+}$*/ROSA*$^{mT/mG}$ mouse trachea. ***(A)*** Shows native villin-eGFP (green) fluorescence in a flask-shaped epithelial cell (asterisk), and no tdTomato (red) co-expression in the same cell. ***(B)*** Immunohistochemistry with an antibody against eGFP and utilizing Cy5-conjugated secondary antibodies. A native villin-eGFP^{+} (green) cell (asterisk) is immunoreactive to eGFP antibody (yellow). There is no tdTomato (red) co-expression in the same cell. ***(C and D)*** Immunohistochemistry with antibodies against eGFP and villin. ***(C)*** Shows that Cre-recombinase expression (asterisk) had occurred in villin-immunoreactive epithelial cell (arrowhead). ***(D)*** Shows villin-immunoreactive epithelial cell (arrowhead), however, this cell does not show Cre-recombinase activity. Images captured with monochrome camera; false colors are shown.

3.1.2.2.1 *Vil1-Cre* activity is detected in a subpopulation of tracheal neuroendocrine cells

Tracheal cryosections from *Vil1-Cre*$^{+}$*/ROSA*$^{mT/mG}$ mice were double-immunolabeled with antibodies against eGFP (to enhance fluorescence of villin-eGFP^{+} cells) and PGP9.5 or CGRP (neuroendocrine cell-specific markers). Immunolabeling revealed villin-eGFP^{+} within a subpopulation of PGP9.5- or CGRP-immunoreactive cells. Rarely, single villin-eGFP^{+} cells were observed (Figure 3.14A-D).

A tracheal whole mount from *Vil1-Cre*$^{+}$*/ROSA*$^{mT/mG}$ mouse (n=1) was immunolabeled with an antibody against the neuroendocrine cell-specific marker CGRP. Immunolabeling revealed villin-eGFP^{+} in a subpopulation of CGRP-immunoreactive cells (Figure 3.14E).

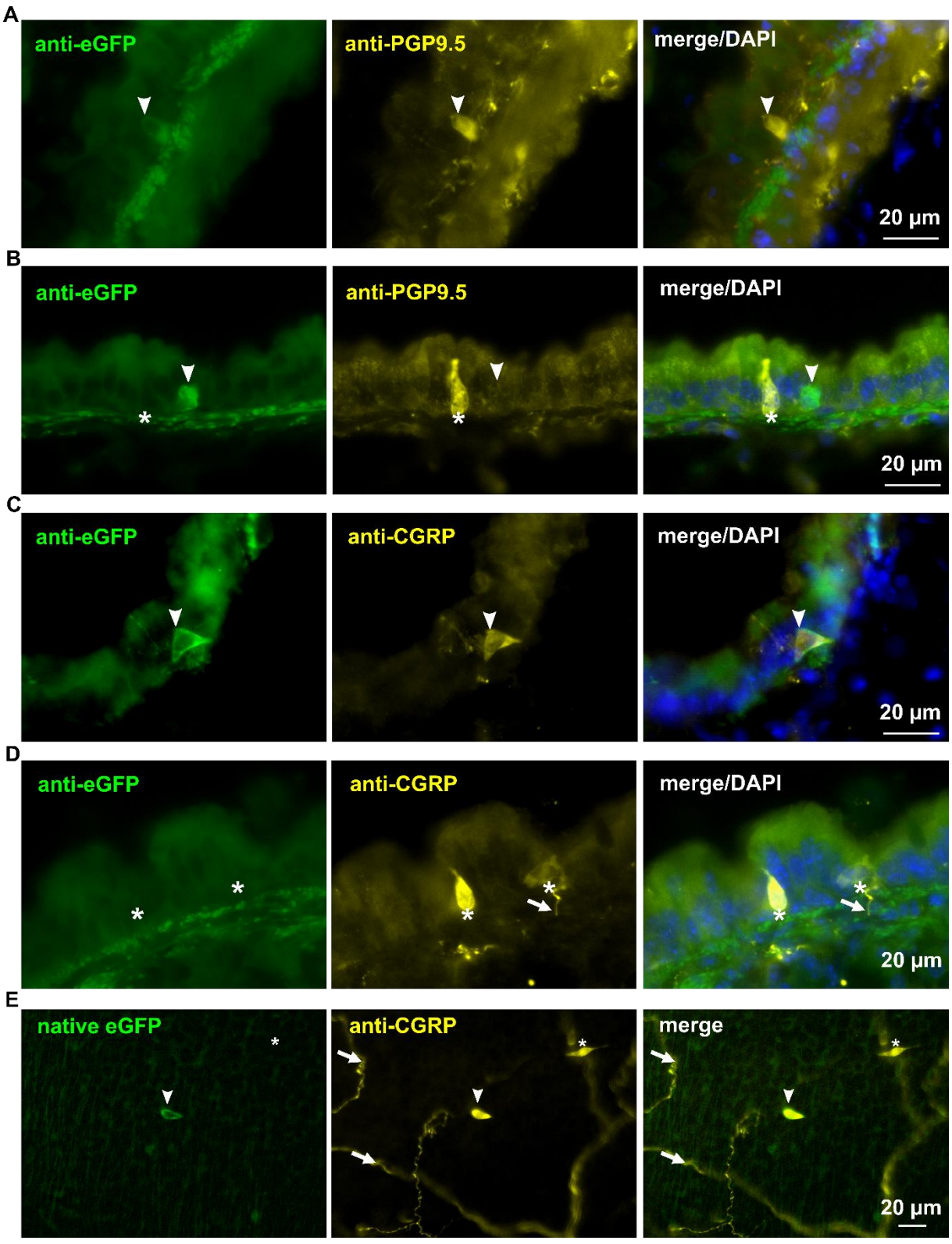

Figure 3.14: *Vil1-Cre* activity is detected in a subpopulation of tracheal neuroendocrine cells.
(A and B) Immunohistochemistry of tracheal cryosections from a *Vil1-Cre*$^{+}$*/ROSA*$^{mT/mG}$ mouse, double-labeled with antibodies against eGFP (green) (to enhance fluorescence of villin-eGFP^{+} cells) and PGP9.5 (yellow), labeling neuroendocrine cells (rabbit polyclonal PGP9.5 antibody was used in the figures unless otherwise indicated). ***(A)*** Shows villin-eGFP^{+} epithelial cell co-

labeled with PGP9.5 antibody (arrowhead). ***(B)*** Shows villin-eGFP^{+} epithelial cell, not co-labeled with PGP9.5 antibody (arrowhead), and a PGP9.5^{+}/villin-eGFP^{-} epithelial cell (asterisk). (***C and D)*** Immunohistochemistry of tracheal cryosections from a *Vil1-Cre^{+}/ROSA$^{mT/mG}$* mouse, double-labeled with antibodies against eGFP (green) (to enhance fluorescence of villin-eGFP^{+} cells) and CGRP (yellow), labeling neuroendocrine cells (rabbit polyclonal αCGRP antibody was used in the figures unless otherwise indicated). ***(C)*** Shows villin-eGFP^{+} epithelial cell co-labeled with CGRP antibody (arrowhead). ***(D)*** Shows CGRP^{+}/villin-eGFP^{-} epithelial cells (asterisks). CGRP^{+} nerve fibers are indicated by arrows. ***(E)*** Tracheal whole mount immunohistochemistry from a *Vil1-Cre^{+}/ROSA$^{mT/mG}$* mouse, labeled with an antibody against CGRP labeling neuroendocrine cells and CGRP^{+} nerve fibers (nerve fibers indicated by arrow), shows native villin-eGFP (green) expression in an epithelial cell (arrowhead), which is also CGRP-immunoreactive (yellow). However, a CGRP^{+}/villin-eGFP^{-} cell is also present (asterisk). Images captured with monochrome camera; false colors are shown.

3.1.2.2.2 *Vil1-Cre* activity is not detected in tracheal cholinergic chemosensory cells

Tracheal cryosections from *Vil1-Cre^{+}/ROSA$^{mT/mG}$* mice were double-immunolabeled with antibodies against eGFP (to enhance fluorescence of villin-eGFP^{+} cells) and TRPM5. Immunolabeling revealed that villin-eGFP^{+} cells were not immunoreactive to TRPM5 antibody (Figures 3.15A and 3.15B).

A tracheal whole mount from a *Vil1-Cre^{+}/ROSA$^{mT/mG}$* mouse (n=1) was immunolabeled with an antibody against TRPM5 (cholinergic chemosensory cell-specific marker). Immunolabeling revealed that villin-eGFP^{+} cells were not immunoreactive to TRPM5 antibody (Figure 3.15C).

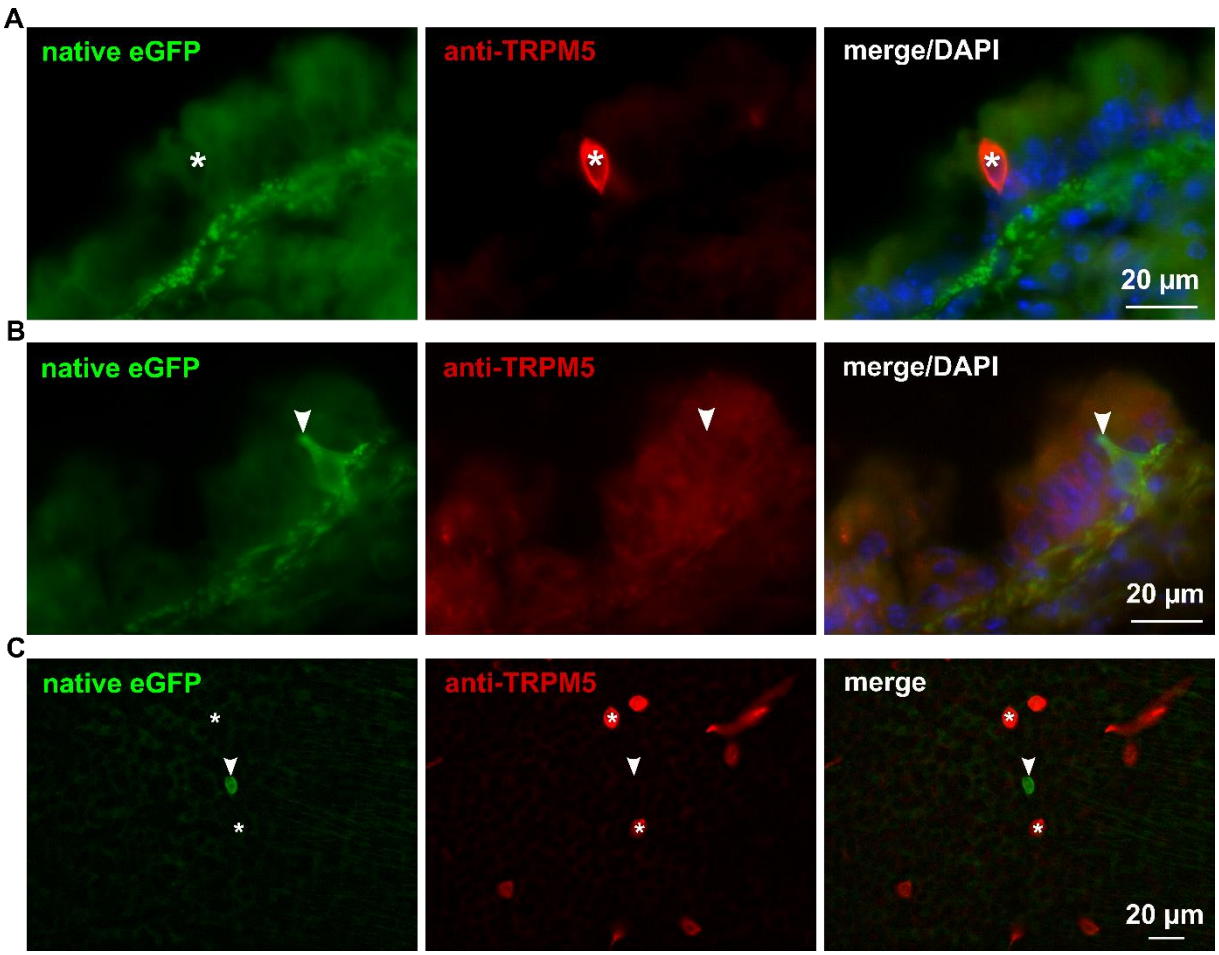

Figure 3.15: *Vil1-Cre* activity is not detected in tracheal cholinergic chemosensory cells. ***(A and B)*** Immunohistochemistry of tracheal cryosections from a *Vil1-Cre*$^{+}$*/ROSA*$^{mT/mG}$ mouse, double-labeled with antibodies against eGFP (green) (to enhance fluorescence of villin-eGFP^{+} cells) and TRPM5 (red), labeling cholinergic chemosensory cells. ***(A)*** Shows TRPM5^{+} cell with no villin-eGFP-immunoreactivity (asterisk). ***(B)*** Shows villin-eGFP^{+} epithelial cell with no TRPM5-immunoreactivity (arrowhead). ***(C)*** Tracheal whole mount immunohistochemistry from a *Vil1-Cre*$^{+}$*/ROSA*$^{mT/mG}$ mouse, labeled with an antibody against TRPM5, labeling cholinergic chemosensory cells (asterisks, red), shows native villin-eGFP (green) expression in an epithelial cell (arrowhead), not co-labeled with TRPM5 antibody. Images captured with monochrome camera; false colors are shown.

3.1.2.3 RT-PCR reveals expression of *Vil1*- and *Calca*-mRNAs in the trachea

Villin and CGRP proteins were detected in the tracheal epithelium by immunohistochemistry (section 3.1.2.1). To validate the presence of villin and CGRP at the mRNA level in the trachea and more specifically in the epithelium, RT-PCR of whole tracheal samples and samples obtained from abraded tracheal epithelium was performed. RT-PCR revealed expression of *Vil1*- and *Calca*-mRNAs in the trachea and in the tracheal epithelium (Figure 3.16). The *Calca* gene encodes the precursor of the neuropeptide CGRP.

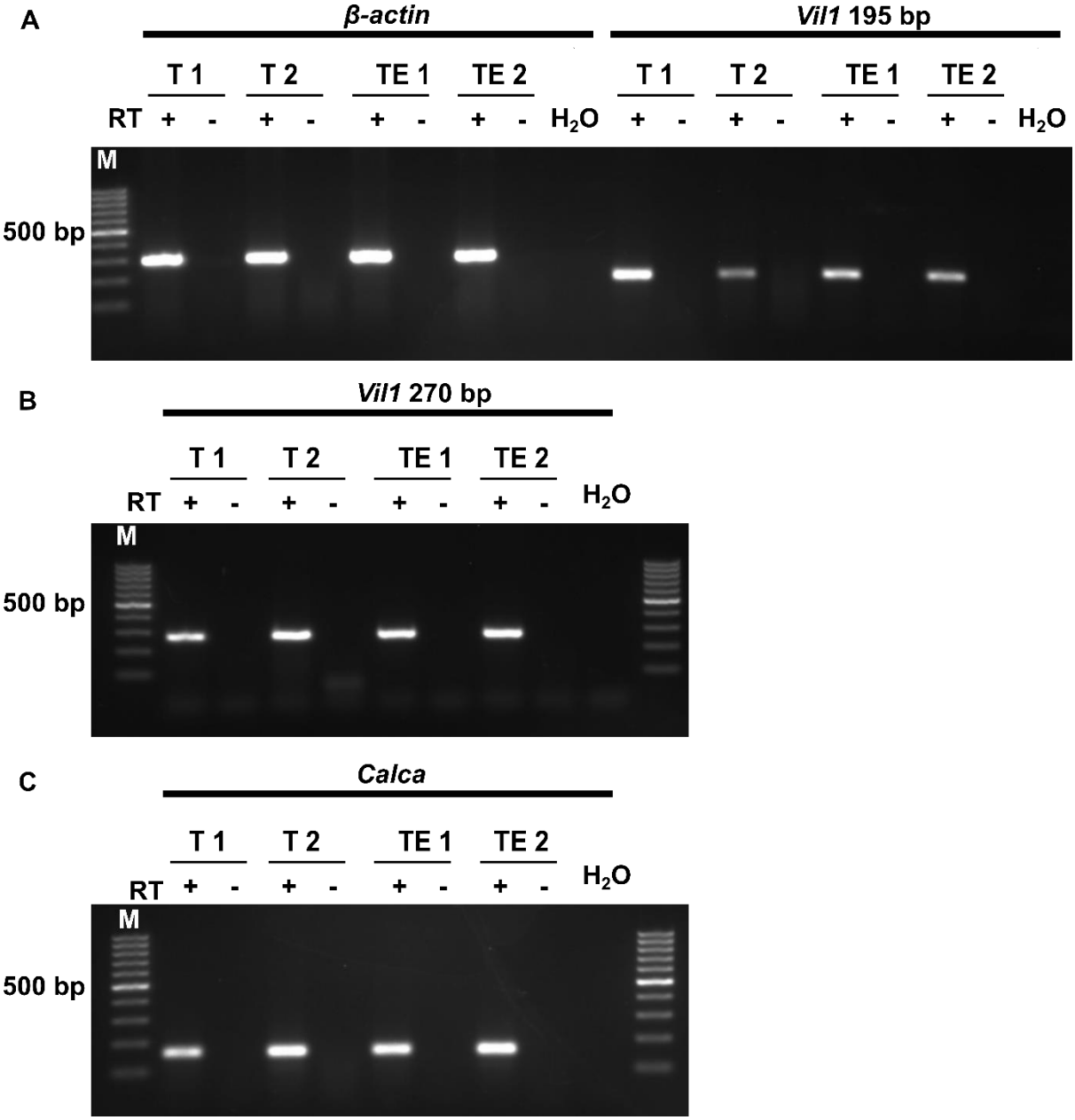

Figure 3.16: *Vil1*- and *Calca*-mRNAs are expressed in the trachea.
PCR experiments with cDNA obtained from whole trachea (T) (n=2) and tracheal epithelium (TE) (n=2) of C57BL/6RJ animals. Primers for *β-actin* (300 bp), *Vil1* (195 bp), *Vil1* (270 bp) and *Calca* (158 bp) were used. Controls were RNA samples processed without reverse transcriptase (RT) and water (H_2O) without adding cDNA. ***(A)*** Amplicons of *β-actin* and *Vil1* (product length=195 bp) are detected in all tracheal samples. ***(B)*** Amplicons of *Vil1* (product length=270 bp) is detected in all tracheal samples. ***(C)*** Amplicons of *Calca* is detected in all tracheal samples.

3.1.2.4 *In silico*-analysis of publicly available sequencing data reveals *Vil1*-mRNA expression in tracheal neuroendocrine cells

The immunohistochemical finding was validated and supplemented by *in silico*-analysis of published sequencing data of murine tracheal epithelial cells [5]. We were able to reproduce

the clustering according to the results reported by Plasschaert and coworkers and could identify eight distinct cell clusters, namely basal, secretory, Krt4/13^{+}, ciliated, ionocytes, cholinergic chemosensory cells (brush/tuft), cycling basal and neuroendocrine cells (Figure 3.17A).

This analysis revealed that *Vil1*-mRNA was expressed predominantly in neuroendocrine cells. They were the major source of *Vil1*-mRNA in the mouse airway epithelium, as its expression was negligible in other epithelial cell types. According to this data set, 28.3% (15/53) of neuroendocrine cells were expressing *Vil1*-mRNA, while it was expressed in only 0.2% (5/3220) of basal cells, 0.4% (9/2373) of secretory cells, 0.1% (1/701) of ciliated cells, 0.3% (3/939) of Krt4/13^{+}, and 2.9% (2/70) of cholinergic chemosensory cells (Figures 3.17B and 3.17C).

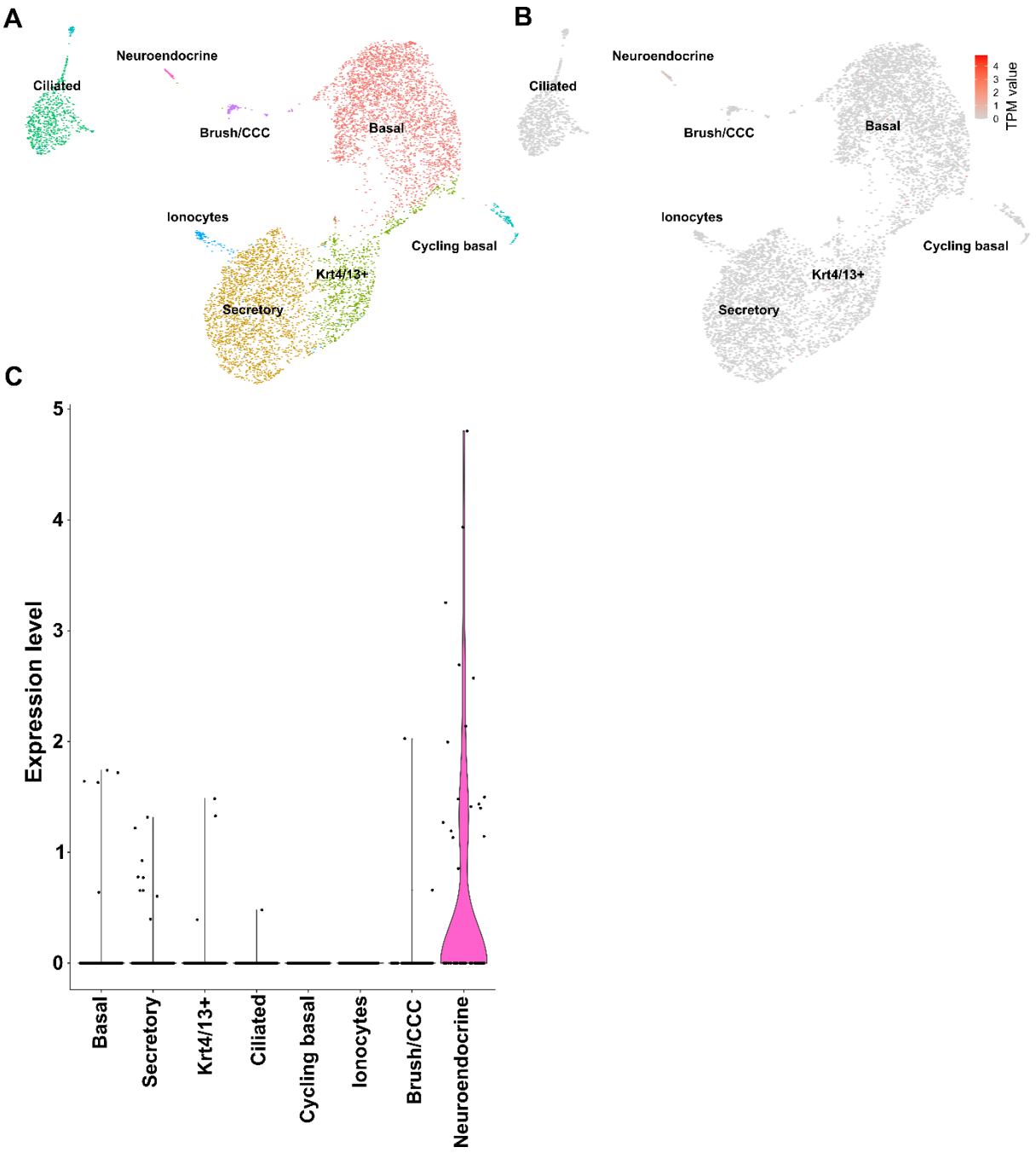

Figure 3.17: *In silico*-analysis of single cell mRNA sequencing data reveals *Vil1*-mRNA expression predominantly in neuroendocrine cells of the tracheal epithelium.
(A-C) *In silico*-analysis of published sequencing data of murine tracheal epithelial cells [5]. ***(A)*** SPRING plot (UMAP) shows eight distinct cell clusters, namely basal, secretory, Krt4/13^{+}, ciliated, ionocytes, cholinergic chemosensory (brush/tuft), cycling basal and neuroendocrine cells. ***(B and C)*** SPRING and violin plots, respectively, showing *Vil1*-mRNA is predominantly expressed within the neuroendocrine cell cluster.

3.1.2.5 Neuroendocrine cell phenotypes based on villin expression in the murine trachea

Immunolabeling of tracheal sections from wild-type mice (C57BL/6RJ) with antibodies against the neuroendocrine cell marker PGP9.5 and villin defined 2 phenotypes of tracheal

neuroendocrine cells; solitary villin^{+}/PGP9.5^{+} (63.6%, 316/497 cells, median=3.5, mean±SEM=3.2±0.75 cells/mm of basement membrane) and solitary villin^{-}/PGP9.5^{+} neuroendocrine cells (26.6%, 132/497 cells, median=1.2, mean±SEM=1.4±0.48 cells/mm of basement membrane). In this approach, additional 9.8% (49/497 cells, median=0.5, mean±SEM=0.5 cell/mm of basement membrane) of immunoreactive cells were single positive for villin (10 coronal sections/trachea, n=4 animals) (Figures 3.9, 3.18A and 3.18B).

However, immunolabeling of tracheal sections from *Vil1-Cre*$^{+}$*/ROSA*$^{mT/mG}$ reporter mice with antibodies against PGP9.5 and eGFP (to enhance fluorescence of villin-eGFP^{+} cells), showed that 32.8% were solitary PGP9.5^{+}/villin-eGFP^{+} (120/366 cells) and 50% were solitary PGP9.5^{+}/villin-eGFP^{-} (183/366 cells). In this approach, additional 17.2% were single positive for eGFP (63/366 cells) (6-8 coronal sections/trachea, n=4 animals) (Figure 3.18C).

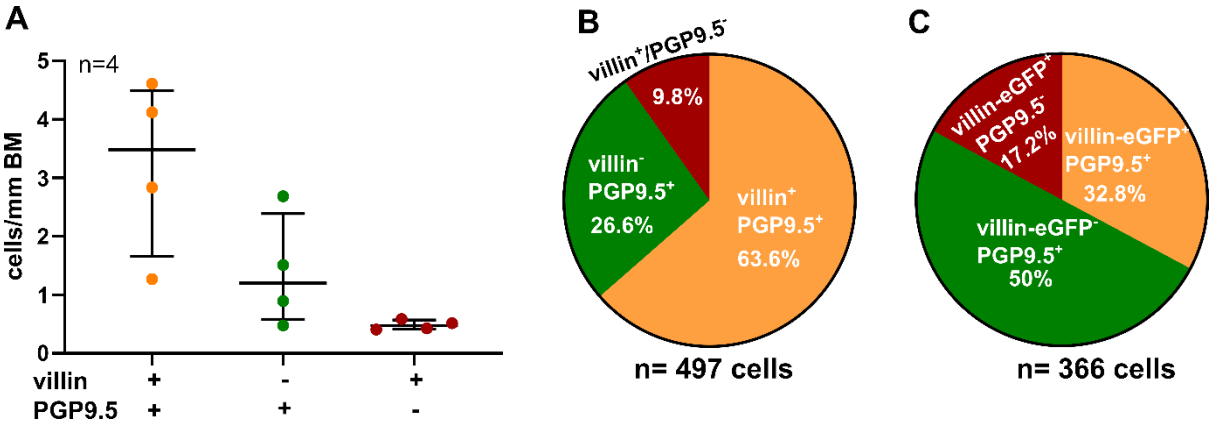

Figure 3.18: Tracheal neuroendocrine cell phenotypes based on villin expression.
(A) Scatter dot plot with median and interquartile range bars, showing mean value for each investigated trachea. Tracheal cryosections from wild-type mice (C57BL/6RJ) were double-labeled with antibodies against PGP9.5 and villin. Quantification of immunoreactive cells in tracheal cryosections (10 coronal sections/trachea, n=4 tracheas), showing the number of villin^{+}/PGP9.5^{+}, villin^{-}/PGP9.5^{+} and villin^{+}/PGP9.5^{-} cells/mm of basement membrane (BM). ***(B)*** Pie chart showing the percentage of phenotypes related to the pooled total number of immunoreactive cells recorded in experiment illustrated in A. ***(C)*** Pie chart showing the percentage of phenotypes related to the pooled total number of immunoreactive cells in tracheal cryosections from *Vil1-Cre*$^{+}$*/ROSA*$^{mT/mG}$ reporter mice.

3.1.3 Villin expression in murine broncho-pulmonary neuroendocrine cells

3.1.3.1 Broncho-pulmonary neuroendocrine cells are not villin-immunoreactive

Immunolabeling of lung sections from wild-type mice (C57BL/6RJ) with antibodies against the neuroendocrine cell marker CGRP and villin showed no villin-immunoreactivity in CGRP-

immunoreactive broncho-pulmonary epithelial cells below the bifurcation, neither in solitary broncho-pulmonary neuroendocrine cells, nor in neuroepithelial bodies (n=4) (Figure 3.19).

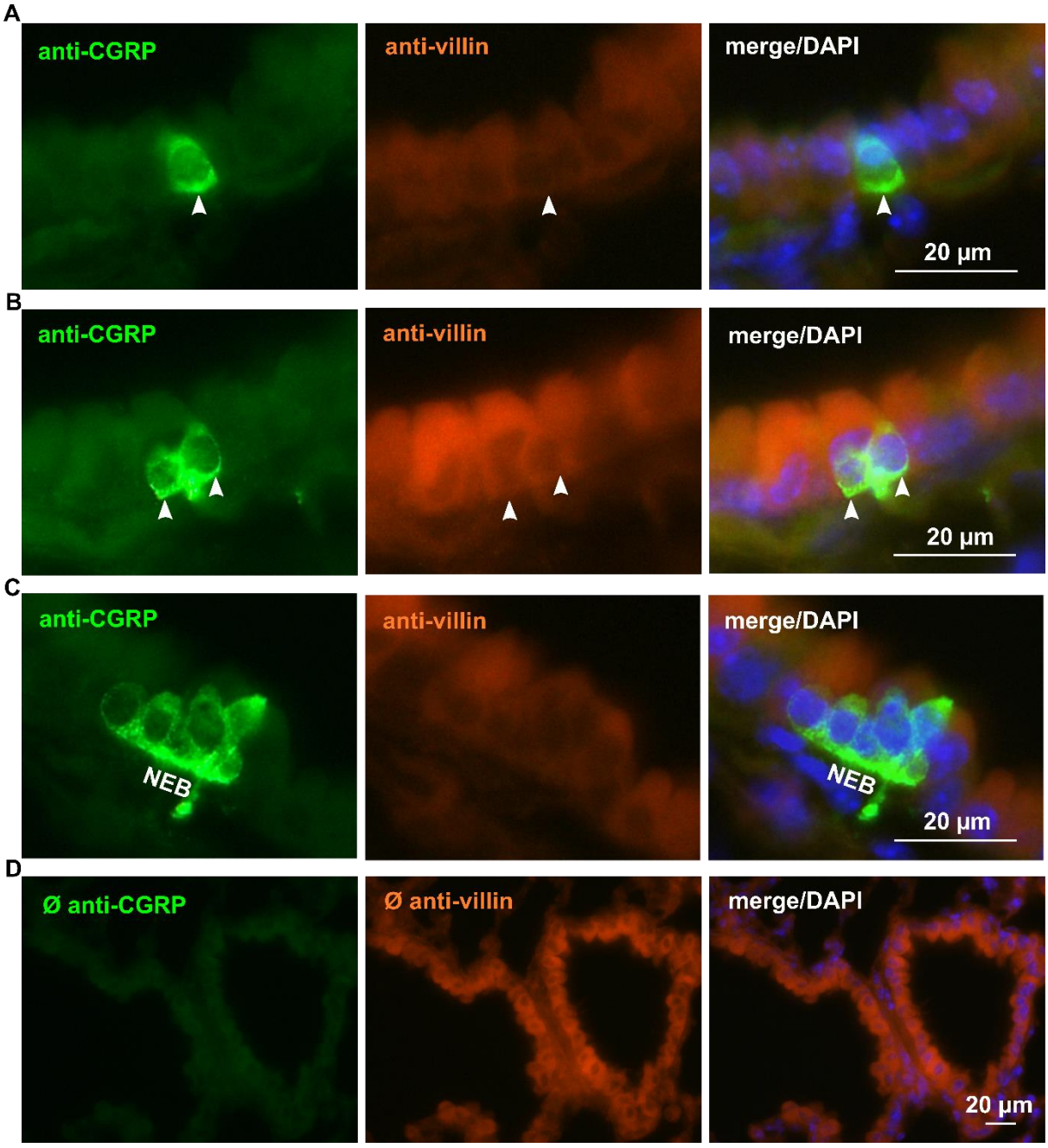

Figure 3.19: Broncho-pulmonary neuroendocrine cells are not villin-immunoreactive. ***(A-C)*** Immunohistochemistry of lung cryosections from wild-type mice (C57BL/6RJ), double-labeled with antibodies against villin in orange and CGRP in green (goat polyclonal αCGRP). ***(A)*** Shows solitary neuroendocrine cell ($CGRP^+$) with no villin-immunoreactivity (arrowhead). ***(B)*** Shows a neuroepithelial body consisting of two $CGRP^+$ cells, both are not villin-immunoreactive (arrowheads). ***(C)*** Shows a neuroepithelial body (NEB) consisting of more than 5 cells ($CGRP^+$), all cells are not villin-immunoreactive. ***(D)*** No immunoreactivity is observed when all primary antibodies were omitted. Images captured with color camera; true colors are shown.

3.1.3.2 *Vil1* promoter drives Cre-recombinase expression in broncho-pulmonary epithelial cells

In lung cryosections from *Vil1-Cre*$^{+}$*/ROSA*$^{mT/mG}$ animals (n=6), native eGFP was detected in a single or cluster of pyramidal/flask-shaped cells (Figure 3.20). When sections were immunolabeled with an antibody against eGFP and utilizing Cy5-conjugated secondary antibodies, all native eGFP^{+} cells were immunoreactive to eGFP antibody; no additional cells were visible (Figure 3.20A). As expected, in *Vil1-Cre*$^{-}$*/ROSA*$^{mT/mG}$ animals (n=6), no eGFP signal was detected with and without eGFP immunolabeling (Figure 3.20B). Red tdTomato-fluorescence (visualized with filters suited for Cy3 or Texas Red) was present in every cell which was not green in *Vil1-Cre*$^{+}$*/ROSA*$^{mT/mG}$ animals. As expected, in *Vil1-Cre*$^{-}$*/ROSA*$^{mT/mG}$ animals, all cells showed red fluorescence using these filters (Figure 3.20).

Double immunolabeling with eGFP and villin antibodies (Figure 3.20C-E) revealed that Cre-recombinase expression occurred in a cluster or single cells, but most of them were not villin-immunoreactive. Villin-immunoreactivity was observed very rarely in villin-eGFP^{+} cells (Figure 3.20E).

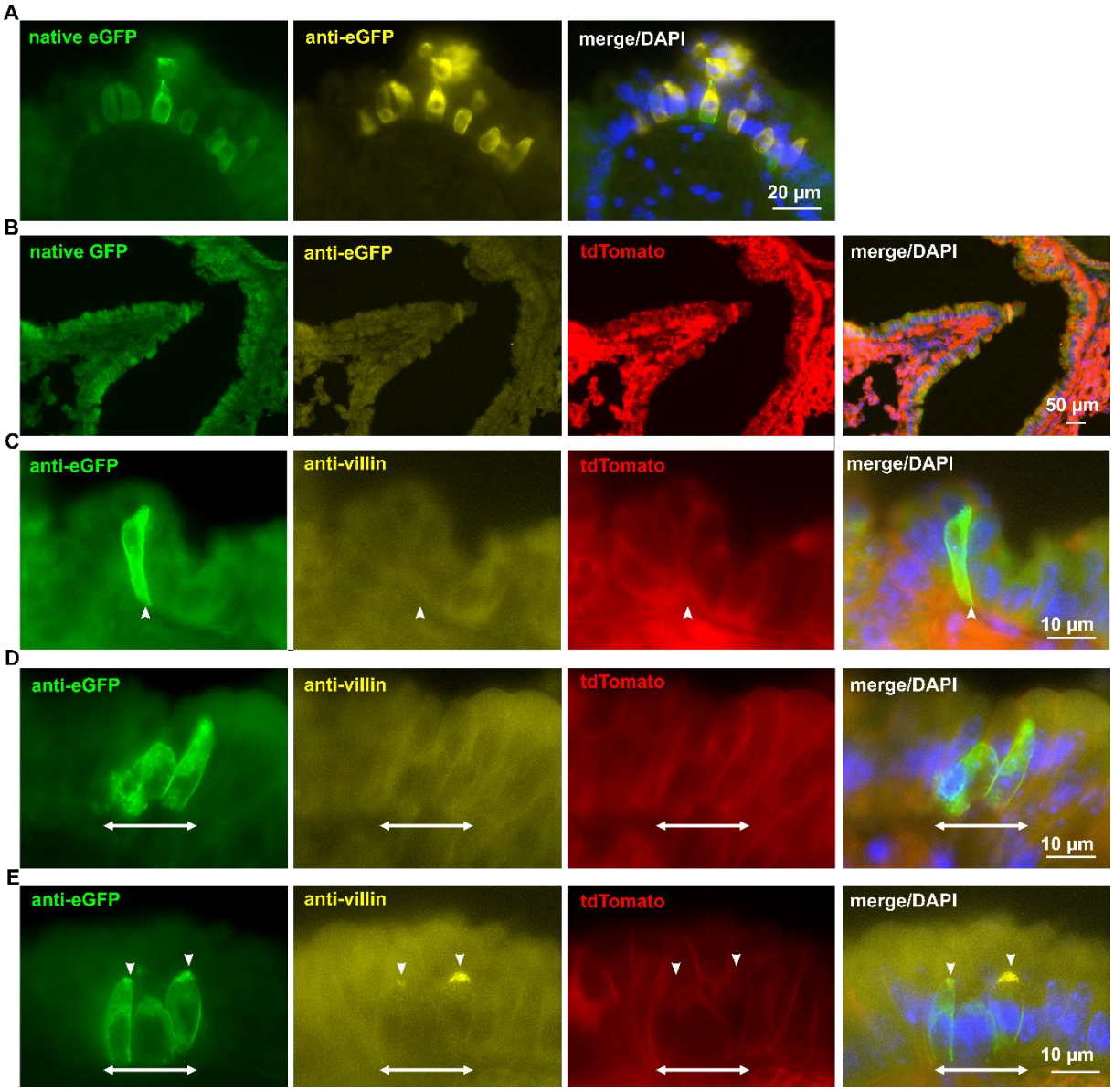

Figure 3.20: The *Vil1* promoter drives Cre-recombinase expression in broncho-pulmonary epithelial cells.
(A and C-E) Immunohistochemistry of lung cryosections from *Vil1-Cre*$^{+}$*/ROSA*$^{mT/mG}$ mice. ***(A)*** Labeled with an antibody against eGFP and utilizing Cy5-conjugated secondary antibodies, shows a cluster of native villin-eGFP^{+} (green) cells that are immunoreactive to eGFP antibody (yellow). ***(B)*** Immunohistochemistry of lung cryosection from a *Vil1-Cre*$^{-}$*/ROSA*$^{mT/mG}$ mouse shows no native villin-eGFP (green) expression in the epithelium. However, tdTomato (red) is expressed in the whole epithelium. ***(C-E)*** Double-labeled with antibodies against eGFP and villin. ***(C)*** Shows a single villin-eGFP^{+} cell with no villin-immunoreactivity. ***(D)*** Shows a cluster of villin-eGFP^{+} cells, all cells are not villin-immunoreactive. ***(E)*** Shows cluster of villin-eGFP^{+} cells (3 cells), two of them are co-labeled with villin antibody (arrowheads). Images captured with monochrome camera; false colors are shown.

3.1.3.2.1 *Vil1-Cre* activity is detected in a subpopulation of broncho-pulmonary neuroendocrine cells

Lung cryosections from *Vil1-Cre*$^{+}$*/ROSA*$^{mT/mG}$ mice (n=6) were double-immunolabeled with antibodies against eGFP (to enhance fluorescence of villin-eGFP^{+} cells) and CGRP (neuroendocrine cell-specific marker). Immunolabeling revealed villin-eGFP^{+} in a subpopulation of CGRP-immunoreactive cells (Figure 3.21).

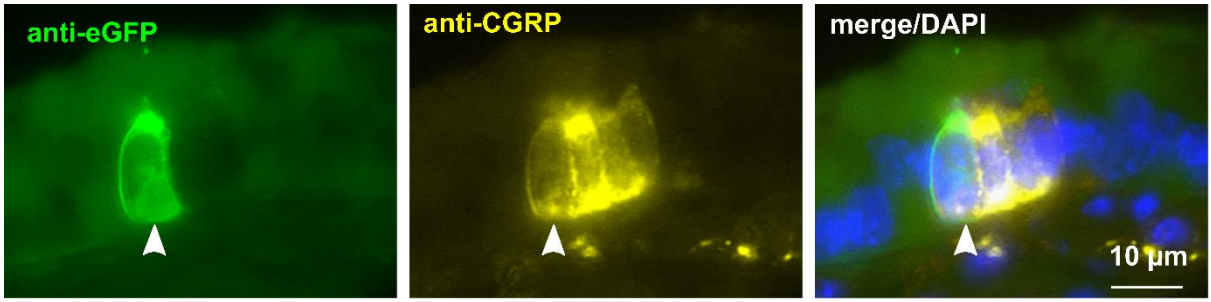

Figure 3.21: *Vil1-Cre* activity is detected in a subpopulation of broncho-pulmonary neuroendocrine cells.
Immunohistochemistry of lung cryosection from a *Vil1-Cre*$^{+}$*/ROSA*$^{mT/mG}$ mouse, double-labeled with antibodies against eGFP (green) (to enhance fluorescence of villin-eGFP^{+} cells) and CGRP (yellow) labeling neuroendocrine cells. Villin-eGFP^{+} epithelial cell co-labeled with CGRP antibody (arrowhead). Images captured with monochrome camera; false colors are shown.

3.1.3.3 RT-PCR reveals expression of *Vil1*- and *Calca*-mRNAs within the lung

Villin was not detected in the lung by immunohistochemistry (section 3.1.3.1), but *Vil1-Cre* activity was detected in the broncho-pulmonary neuroendocrine cells (CGRP-immunoreactive cells) (section 3.1.3.2). To assess the presence of villin and CGRP at the mRNA level within the lung, RT-PCR for pieces of lung samples were performed. RT-PCR revealed expression of *Vil1*- and *Calca*-mRNAs within the lung (Figure 3.22). The *Calca* genes encodes the precursor of the neuropeptide CGRP.

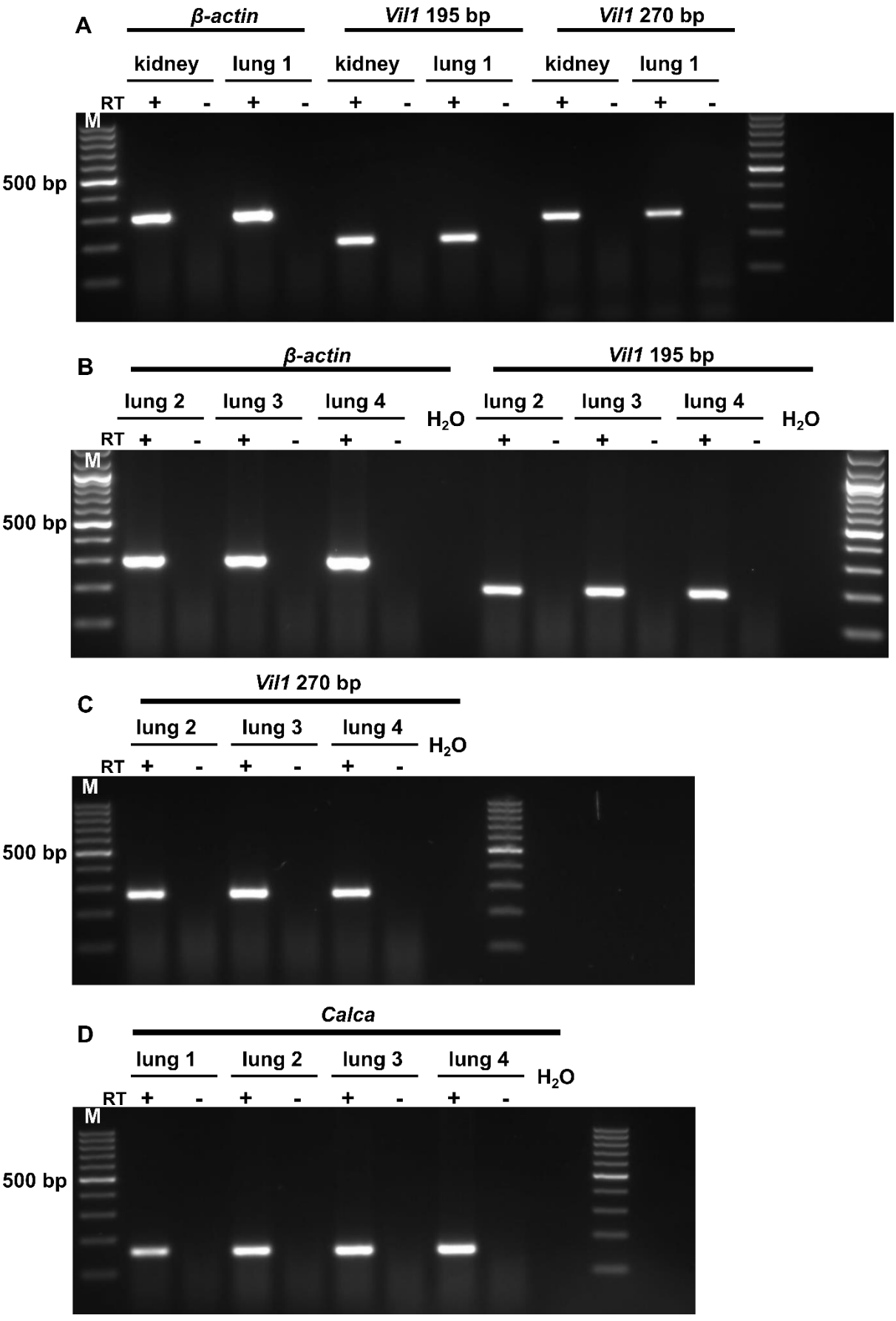
A
β-actin
Vil1 195 bp
Vil1 270 bp
kidney
lung 1
kidney
lung 1
kidney
lung 1
RT + - + - + - + - + - + -
M
500 bp
B
β-actin
Vil1 195 bp
lung 2
lung 3
lung 4
H2O
lung 2
lung 3
lung 4
H2O
RT + - + - + - + - + - + -
M
500 bp
C
Vil1 270 bp
lung 2
lung 3
lung 4
H2O
RT + - + - + -
M
500 bp
D
Calca
lung 1
lung 2
lung 3
lung 4
H2O
RT + - + - + - + -
M
500 bp

Figure 3.22: *Vil1*- and *Calca*-mRNAs are expressed in the lung.
PCR experiments with cDNA obtained from kidney as a positive control for villin expression (n=1) and lung (n=4) of C57BL/6RJ animals. Primers for *β-actin* (300 bp), *Vil1* (195 bp), *Vil1* (270 bp) and *Calca* (158 bp) were used. Controls were RNA samples processed without reverse transcriptase (RT) and water (H_2O) without adding cDNA. ***(A)*** Amplicons of *β-actin*, *Vil1* (product size=195 bp) and *Vil1* (product size=270 bp) are detected in kidney and first lung sample. ***(B)*** Amplicons of *β-actin* and *Vil1* (product size=195 bp) are detected in the other three lung samples. ***(C)*** Amplicons of *Vil1* (product size=270 bp) is detected in the other three lung samples. ***(D)*** Amplicons of *Calca* is detected in all lung samples.

3.2 CXCL13 expression in neuroendocrine cells in the murine lower airways

3.2.1 CXCL13 is expressed in a subpopulation of neuroendocrine cells in the murine trachea

3.2.1.1 Immunohistochemistry reveals CXCL13-immunoreactivity in PGP9.5-, CGRP- and villin-immunoreactive cells

CXCL13-immunoreactive cells were identified in the tracheal epithelium of mice (Figure 3.23). In whole mount tracheal preparations, the cell density decreased by more than 50% from cranial (larynx) to caudal (bifurcation) (Figure 3.23A and B), as it has been reported for cholinergic chemosensory cells and solitary neuroendocrine cells [24, 81]. As described for ciliated [166] and cholinergic chemosensory cells and nerve fibers [7], the density of CXCL13-immunoreactive cells was higher in the intercartilage regions (approximately doubled compared to regions overlying cartilage) (Figure 3.23A and C). Neuroendocrine cells, characterized by immunoreactivity to PGP9.5, showed the same distribution pattern with preferential occurrence overlying ligaments between cartilage rings (Figure 3.23C) and marked cranio-caudal gradient (Figure 3.23B). Some of the CXCL13-immunoreactive cells received contacts from peptidergic CGRP positive sensory nerve fibers (Figure 3.23D).

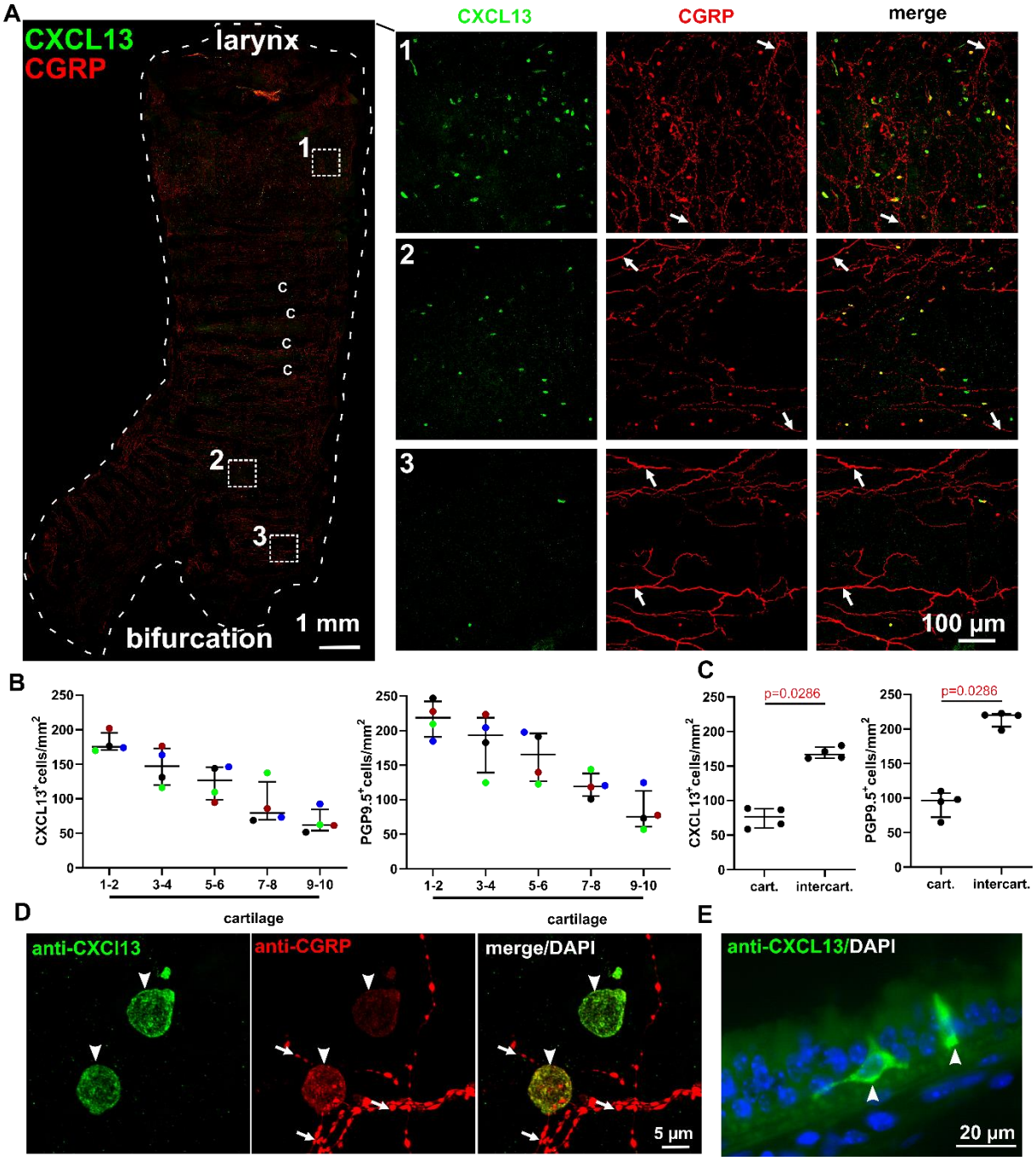

Figure 3.23: CXCL13 expression and distribution in the murine tracheal epithelium of C57BL/6RJ animals.
(A and D) Immunohistochemistry of tracheal whole mounts, CLSM, maximum intensity projection of z-stack of confocal optical sections, double-labeled with antibodies against CXCL13 (green) and CGRP (red), labeling single neuroendocrine cells and nerve fibers. ***(A)*** The density of neuroendocrine cells, CXCL13-immunoreactive cells and nerve fibers is higher between the cartilage rings (C). The density of neuroendocrine cells and CXCL13-immunoreactive cells decreases from cranial (larynx) (1) to caudal (bifurcation) (3). $CGRP^+$ nerve fibers are visible throughout the whole trachea (arrow). ***(B and C)*** Scatter dot plots with median and interquartile range bars, showing the cell densities quantified on tracheal whole mounts double-labeled for CXCL13 and PGP9.5 (neuroendocrine cell marker). The density of immunoreactive cells continuously declines along the cranio-caudal axis (B). The

immunoreactive cells dominate in intercartilage regions (C). In (B), counts include both the area overlying a cartilage and the next intercartilage region; colour coding along the carnio-caudal axis identifies data from the same trachea. ***(D)*** $CXCL13^+$ cells are in contact with $CGRP^+$ nerve fibers (arrow). CGRP- and CXCL13-co-labeling is indicated by arrowheads. ***(E)*** Immunohistochemistry of a tracheal cryosection with an antibody against CXCL13 shows immunoreactive triangular or flask-shaped cells with processes in the epithelium, image captured with monochrome camera; false colors are shown.

The immunoreactive cells were polarized, flask-shaped epithelial cells (Figures 3.23E and 3.24A). Further investigation was done to define the major cell type which is the source of CXCL13 in the tracheal epithelium. The general distribution and the shape of these cells hinted at cholinergic chemosensory or neuroendocrine cells, as they had comparable density. Quantification of whole mount tracheal preparations from *Chat*-eGFP reporter mice immunolabeled with antibodies against eGFP (to enhance fluorescence of ChAT-$eGFP^+$ cells; cholinergic chemosensory cells) and PGP9.5 (neuroendocrine cell-specific marker) revealed that the density of cholinergic chemosensory cells (median=278, mean±SEM=313.7±50.2 cells/mm^2) is slightly higher than neuroendocrine cells (median, 220, mean±SEM=224.6±9.9 cells/mm^2) ($p=0.065$, Mann Whitney test, n=6 animals) (Figures 3.24B and 3.24C). (This quantification was done by Alexander Perniss, Institute for Anatomy and Cell Biology, Justus Liebig University, Giessen, Germany). Tracheal whole mount preparations and cryosections from *Chat*-eGFP reporter mice were triple-stained with antibodies against eGFP (to enhance fluorescence of ChAT-$eGFP^+$ cells; cholinergic chemosensory cells), PGP9.5 (neuroendocrine cell-specific marker), and CXCL13. Immunolabeling revealed co-labeling of CXCL13 and PGP9.5, but no co-labeling was observed between CXCL13 and ChAT-eGFP (Figures 3.24A, 3.24B and 3.24D).

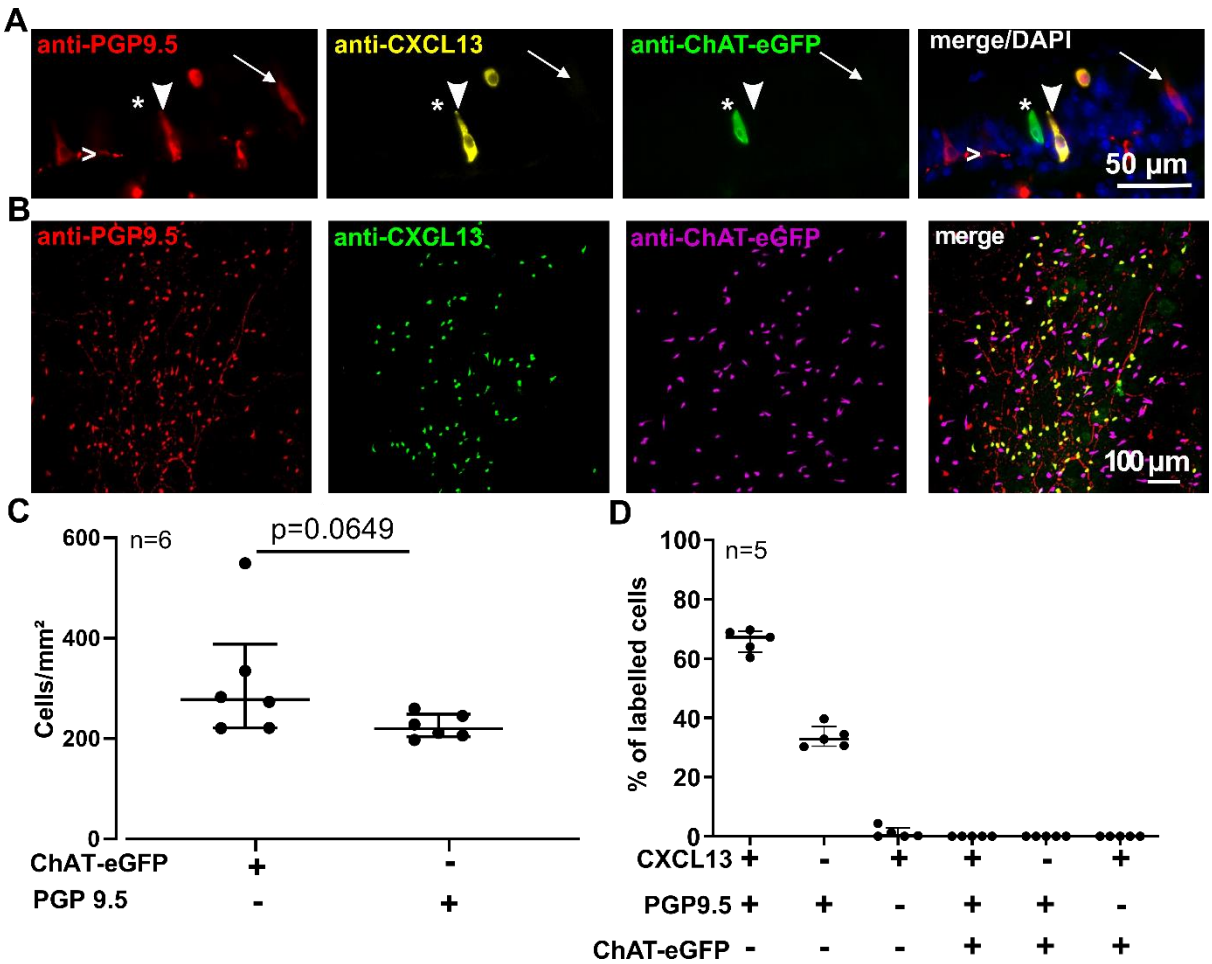

Figure 3.34: CXCL13- and/or PGP9.5-immunoreactivity in the tracheal epithelium of *Chat*-eGFP mice.
(A) Immunohistochemistry of a tracheal cryosection. In the tracheal epithelium, single flask-shaped cells are double-labeled with antibodies against PGP9.5 and CXCL13 (arrowhead) or immunoreactive to PGP9.5 only (arrow). $EGFP^+$ cells (asterisk) are not labeled with antibodies against CXCL13 or PGP9.5. $PGP9.5^+$ nerve fibers are labeled by (>). Image captured with monochrome camera; false colors are shown. ***(B)*** Tracheal whole mount immunohistochemistry, CLSM, maximum intensity projection of z-stack of confocal optical sections. ChAT-$eGFP^+$ cells (magenta) (cholinergic chemosensory cells) are not labeled with antibodies against CXCL13 (green). $CXCL13^+$ cells are labeled with antibodies against PGP9.5 (red) (neuroendocrine cells). ***(C and D)*** Scatter dot plots with median and interquartile range bars, showing the mean value for each investigated trachea. ***(C)*** Shows quantification of whole mount tracheas from *ChAT*-eGFP reporter mice immunolabeled with antibodies against eGFP (to enhance fluorescence of ChAT-$eGFP^+$ cells) and PGP9.5, showing that the density of cholinergic chemosensory cells is slightly higher than neuroendocrine cells (p=0.0649; Mann-Whitney test; n=6). ***(D)*** Shows quantification of the experiments illustrated in B (tracheal whole mount from *ChAT*-eGFP animals). $CXCL13^+$ cells are predominantly labeled with PGP9.5 antibody (~67% of all evaluated cells). Only less than 1% of all evaluated cells are single $CXCL13^+$. No co-existence of ChAT-eGFP and CXCL13 is observed (n=5).

Tracheal whole mount preparations and sections from wild-type mice (C57BL/6Rj) immunolabeled with antibodies against CXCL13 and the chemosensory cell-specific marker TRPM5 or neuroendocrine cell-specific markers (PGP9.5 and/or CGRP) showed also co-labeling for CXCL13 and PGP9.5 and/or CGRP, but not for CXCL13 and TRPM5 (Figures 3.23A, 3.23D and 3.25). Villin was identified in section 3.1 to be expressed by a subpopulation of neuroendocrine cells, so tracheal sections were immunolabeled with antibodies against villin and CXCL13 to find out if they are also co-expressed. Immunolabeling showed co-labeling of villin and CXCL13; in addition, CXCL13 single positive cells were also detected (Figures 3.26A and 3.26B).

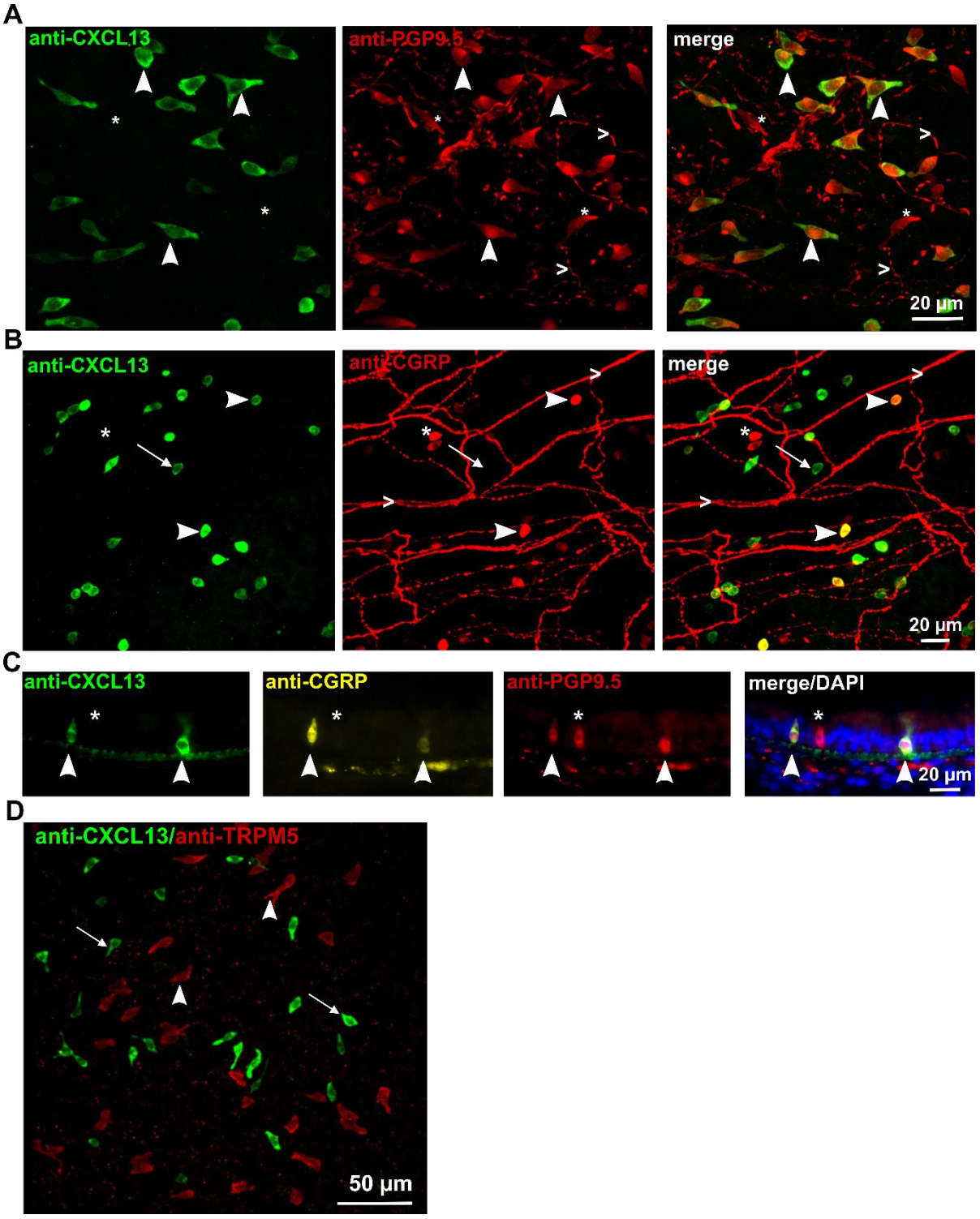

Figure 3.25: CXCL13 is expressed in a subpopulation of neuroendocrine cells in the murine tracheal epithelium of wild-type C57BL/6Rj mice.
(A, B and D) Immunohistochemistry of tracheal whole mounts, CLSM, maximum intensity projection of z-stack of confocal optical sections ***(A)*** CXCL13-immunoreactive cells (green) are labeled with an antibody against PGP9.5 (red) (arrowheads). Single PGP9.5^{+} cells are also found (asterisks). PGP9.5^{+} nerve fibers are indicated by (>). ***(B)*** CXCL13-immunoreactive cells (green) are labeled with an antibody against CGRP (red) (arrowheads). Single CGRP^{+} (asterisk) and single CXCL13^{+} (arrow) cells are also found. CGRP-immunoreactive nerve fibers are indicated by (>). ***(C)*** Immunohistochemistry of a tracheal cryosection shows triple labeling of

single epithelial cells (arrowheads) for CXCL13 (green), CGRP (yellow), and PGP9.5 (red). PGP9.5 single positive cells are also present (asterisk). Image captured with monochrome camera; false colors are shown. ***(D)***. TRPM5-immunoreactive cells (arrowheads) (cholinergic chemosensory cells) are not labeled with antibodies against CXCL13 (green) (arrows).

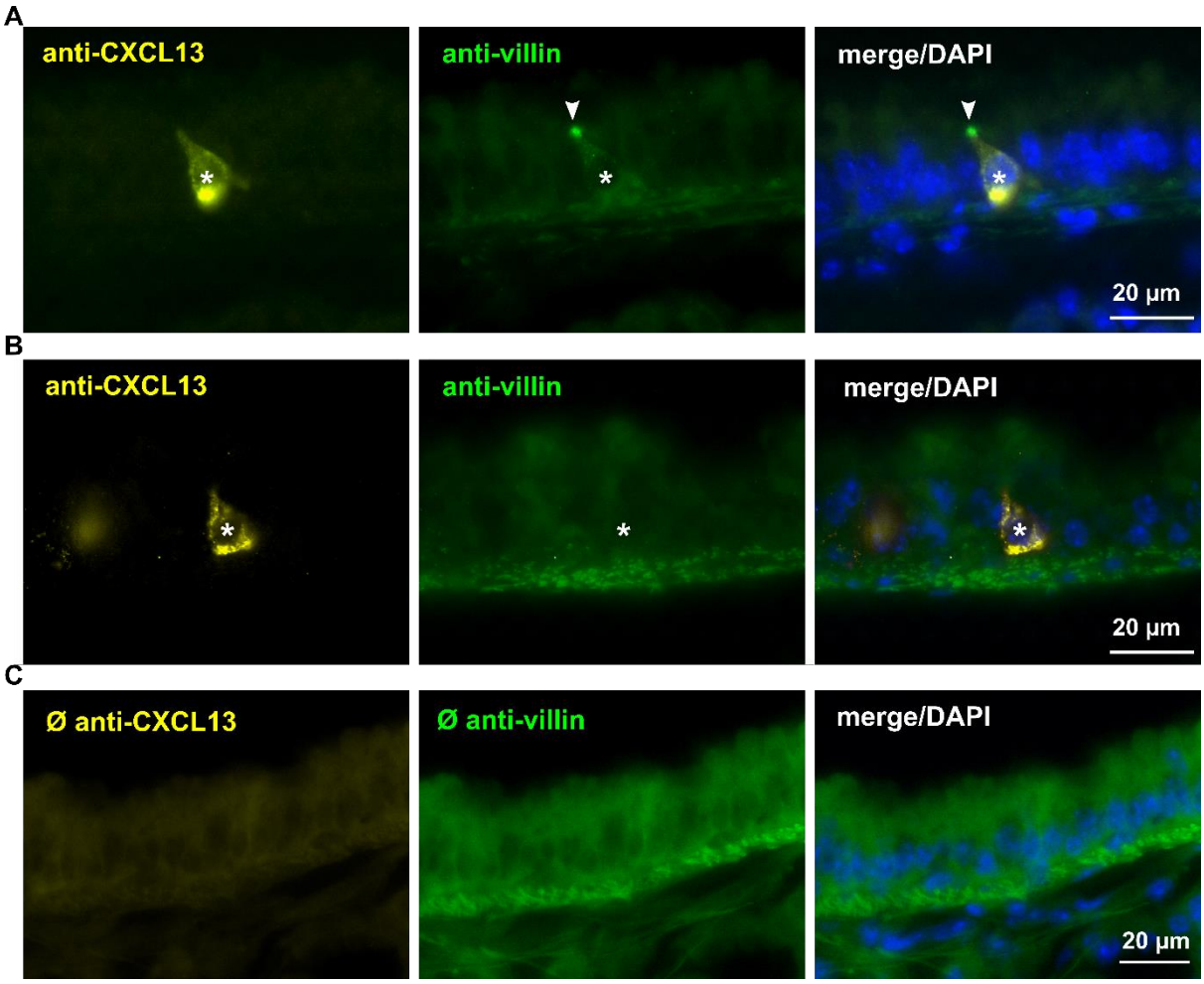

Figure 3.26: Villin- and CXCL13-immunoreactivity in the tracheal epithelium.
(A-C) Immunohistochemistry of tracheal cryosections from a C57BL/6RJ animal. ***(A and B)*** Immunolabeled with antibodies against villin and CXCL13. ***(A)*** shows an epithelial cell double-positive for villin (arrowhead, tip) and CXCL13 (asterisk, whole cell). ***(B)*** Single $CXCL13^{+}$ cell (asterisk), not immunoreactive to villin antibody. ***(C)*** No immunoreactivity is observed when all primary antibodies were omitted. Images captured with color camera; true colors are shown.

High-resolution confocal imaging of immunolabeled tracheal whole mount revealed colocalization of immunoreactivities to CXCL13 and CGRP within the same cell, but with only limited overlap of immunofluorescence signals (Figure 3.27).

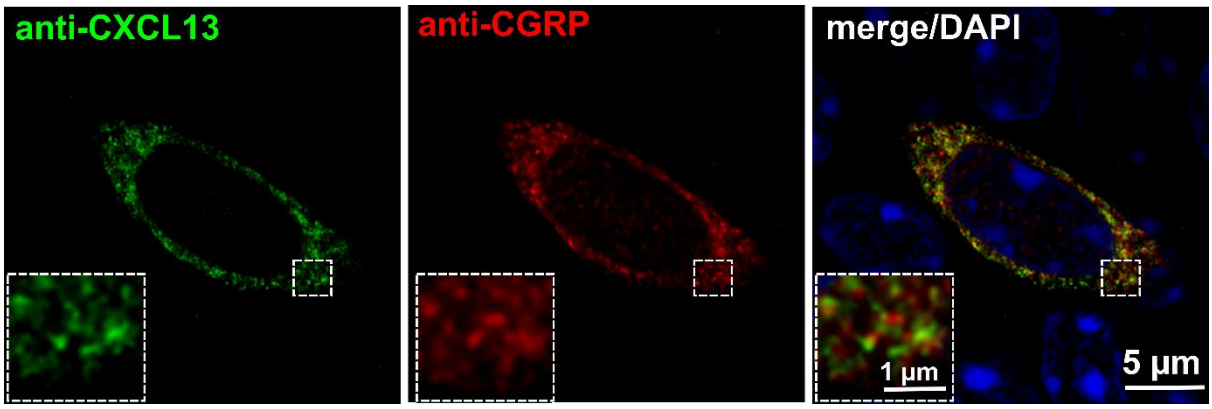

Figure 3.27: High-resolution confocal imaging reveals that CXCL13 and CGRP are present in the same cell, but with minimal fluorescence overlap.
CLSM, single confocal optical section. Immunohistochemistry of tracheal whole mount from C57BL/6RJ animal labeling $CXCL13^+$ cells in green and $CGRP^+$ cells in red, showing colocalization of immunoreactivities to CXCL13 and CGRP within the same cell, but with only limited overlap of immunofluorescence signals. Inset shows a magnified region of the labeled cell.

To confirm the specificity of the applied antibodies against CXCL13, the spleen was used as a positive control, CXCL13 labeled cells in the white pulp, probably follicular dendritic cells (Figure.3.28A). Omission of the primary antibodies was used to validate specific labeling of the secondary antibodies (Figure 3.28B).

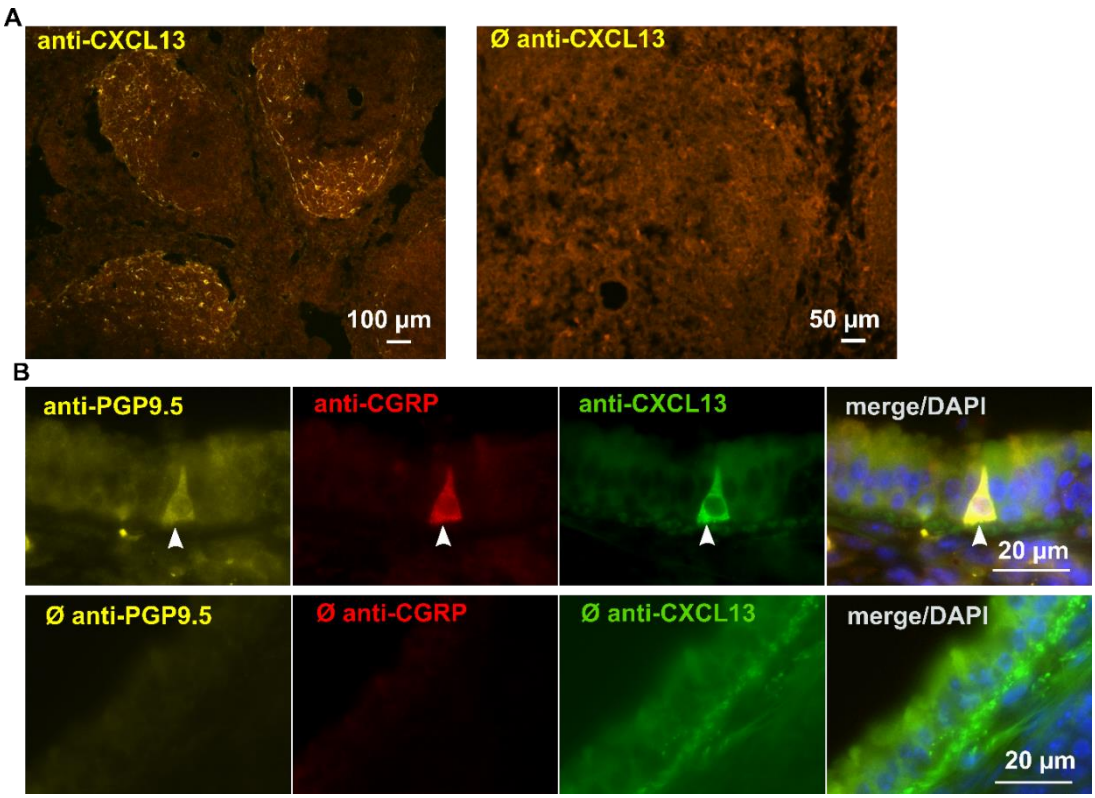

Figure 3.28: Validation of the antibodies used for immunohistochemistry.
(A) Immunohistochemistry of spleen cryosections (positive control) from a C57BL/6RJ animal, showing CXCL13-immunoreactive cells in the white pulp, probably follicular dendritic cells (left image). No staining is observed when the primary antibody (CXCL13) was omitted (right image). Image captured with color camera; true colors are shown. ***(B)*** Immunohistochemistry of tracheal cryosections from a C57BL/6RJ animal, the upper panel shows triple-labeling of a single epithelial cell (arrowhead) for PGP9.5 (yellow), CGRP (red), and CXCL13 (green). No labeling is observed when all primary antibodies were omitted. Image captured with monochrome camera; false colors are shown.

Preabsorption control with the immunizing peptide (full length recombinant CXCL13 protein) completely prevented CXCL13-immunostaining, indicating the specificity of this antibody for the CXCL13 epitope (Figure 3.29).

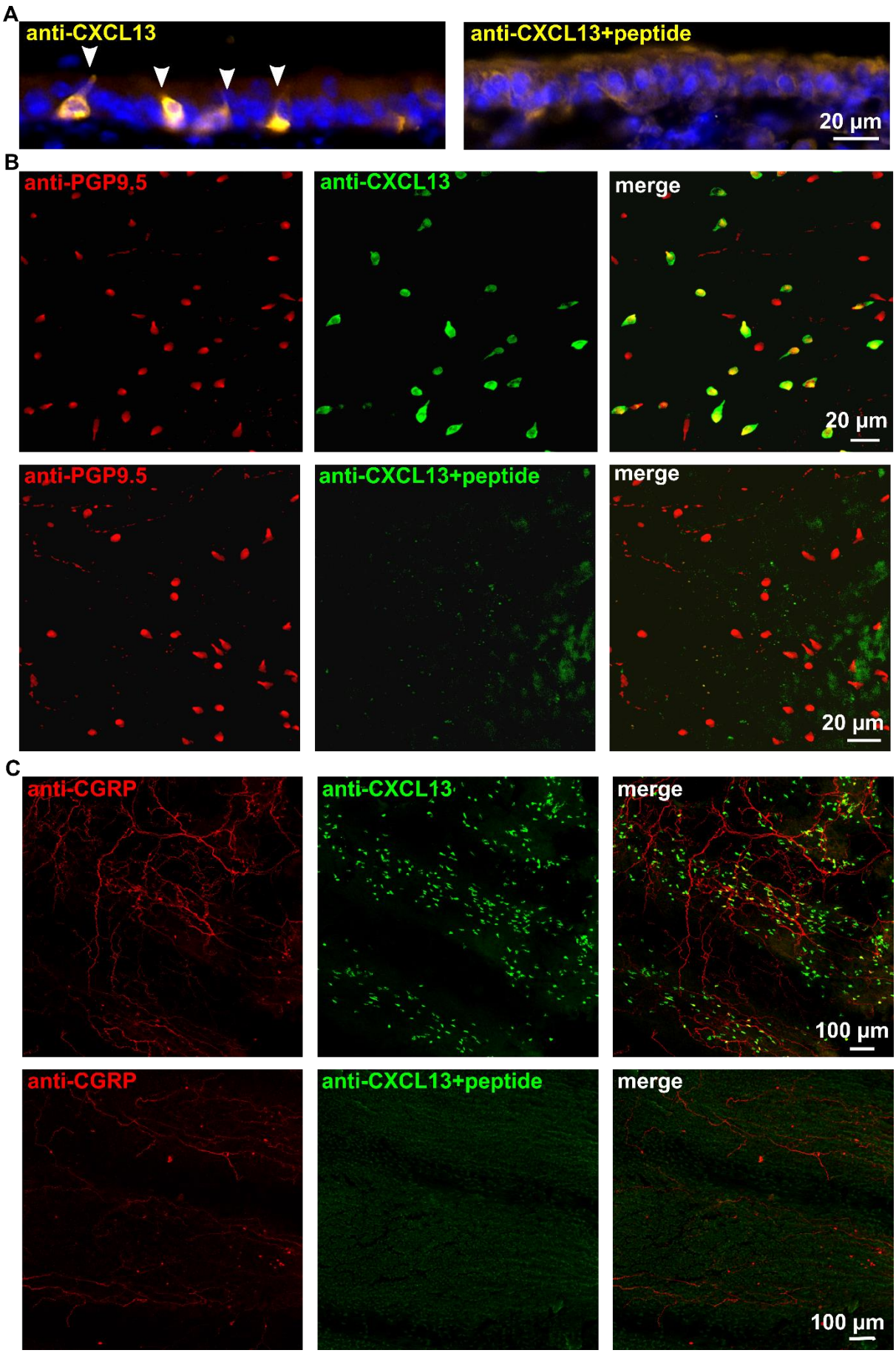
A
anti-CXCL13
anti-CXCL13+peptide
20 µm
B
anti-PGP9.5
anti-CXCL13
merge
20 µm
anti-PGP9.5
anti-CXCL13+peptide
merge
20 µm
C
anti-CGRP
anti-CXCL13
merge
100 µm
anti-CGRP
anti-CXCL13+peptide
merge
100 µm

Figure 3.29: Preabsorption control to validate the CXCL13 antibody used in immunohistochemistry
(A) Immunohistochemistry of tracheal cryosections from a C57BL/6RJ animal. Control experiment (left picture) using an antibody against CXCL13, showing labeling of single cells (arrowheads). Preabsorption with the immunizing peptide (full length recombinant CXCL13 protein) completely blocked CXCL13-immunolabeling (right). Image captured with color camera; true colors are shown. ***(B and C)*** Immunohistochemistry of tracheal whole mounts from a C57BL/6RJ animals, CLSM, maximum intensity projection of z-stack of confocal optical sections Positive control experiments (upper panels in B and C) using antibodies against PGP9.5 (B) or CGRP (C) (red) to identify neuroendocrine cells and antibody against CXCL13 (green), showing double- and single-positive cells. Preabsorption with the immunizing peptide (full length recombinant CXCL13 protein) completely blocked CXCL13-immunolabeling (lower panels in B and C). Immunolabeling with PGP9.5- or CGRP-antibodies was not affected.

3.2.1.2 RT-PCR reveals expression of *Cxcl13*- and *Calca*-mRNAs within the tracheal epithelium

CXCL13 and CGRP proteins were detected in the tracheal epithelium by immunohistochemistry (section 3.2.1.1). To validate the presence of CXCL13 and CGRP at the mRNA level within the tracheal epithelium, RT-PCR for abraded tracheal epithelium were performed. RT-PCR revealed expression of *Cxcl13* and *Calca*-mRNAs within the tracheal epithelium (Figure 3.30). The *Calca* genes encodes the precursor of the neuropeptide CGRP.

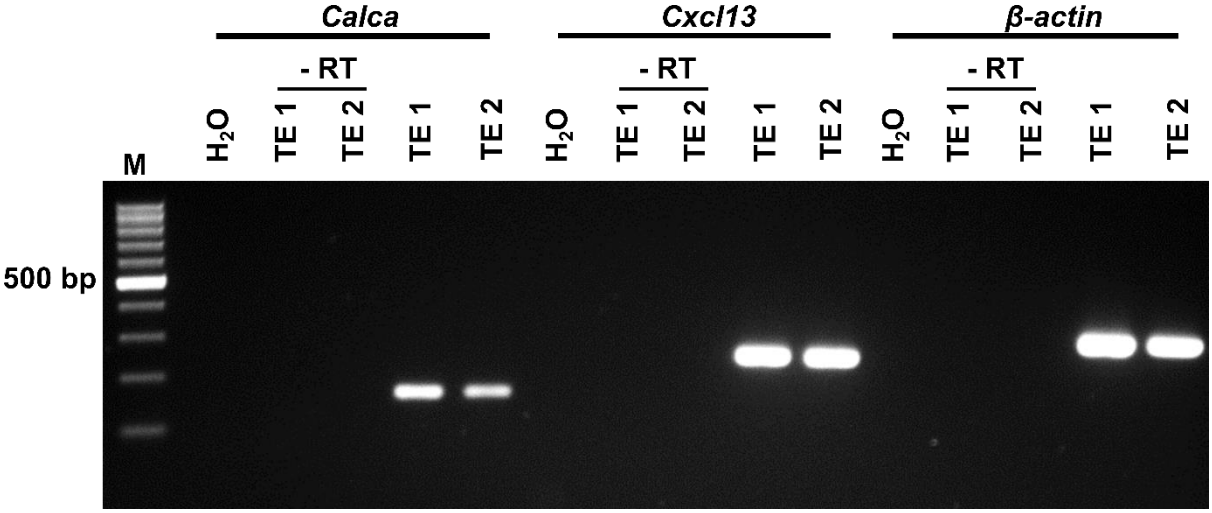

Figure 3.30: *Cxcl13*- and *Calca*-mRNAs are expressed in the tracheal epithelium.
PCR experiments with cDNA obtained from tracheal epithelium of two C57BL/6RJ animal using primers for *Cxcl13* (250 bp), *Calca* (158 bp), and *β-actin* (300 bp). Amplicons of *Calca*, *Cxcl13,* and *β-actin* are detected in both tracheal epithelial samples (TE). Controls=RNA samples processed without reverse transcriptase (-RT) and water (H_2O) without adding cDNA.

3.2.1.3 *In silico*-analysis of publicly available sequencing data reveals *Cxcl13*-mRNA expression in tracheal neuroendocrine cells

The immunohistochemical finding was validated and supplemented by *in silico*-analysis of published sequencing data of murine tracheal epithelial cells [5]. We were able to reproduce the clustering according to the results reported by Plasschaert and coworkers and could identify eight distinct cell clusters, namely basal, secretory, Krt4/13^{+}, ciliated, ionocytes, cholinergic chemosensory (brush/tuft), cycling basal and neuroendocrine cells (Figure 3.31A).

This analysis revealed that *Cxcl13*-mRNA was expressed predominantly in neuroendocrine cells. They were the major source of *Cxcl13*-mRNA in the mouse airway epithelium as its expression was negligible in other epithelial cell types. According to this data set, 68% (36/53) of neuroendocrine cells were expressing C*xcl13*-mRNA, while it was expressed in only 0.3% (9/3220) of basal cells, 0.3% (8/2373) of secretory cells, 0.4% (4/939) of Krt4/13^{+}, 0.6% (4/701) of ciliated cells, 1.6% (3/190) of cycling basal cells, and 4.8% (3/62) of ionocytes (Figures 3.31B and 3.31C).

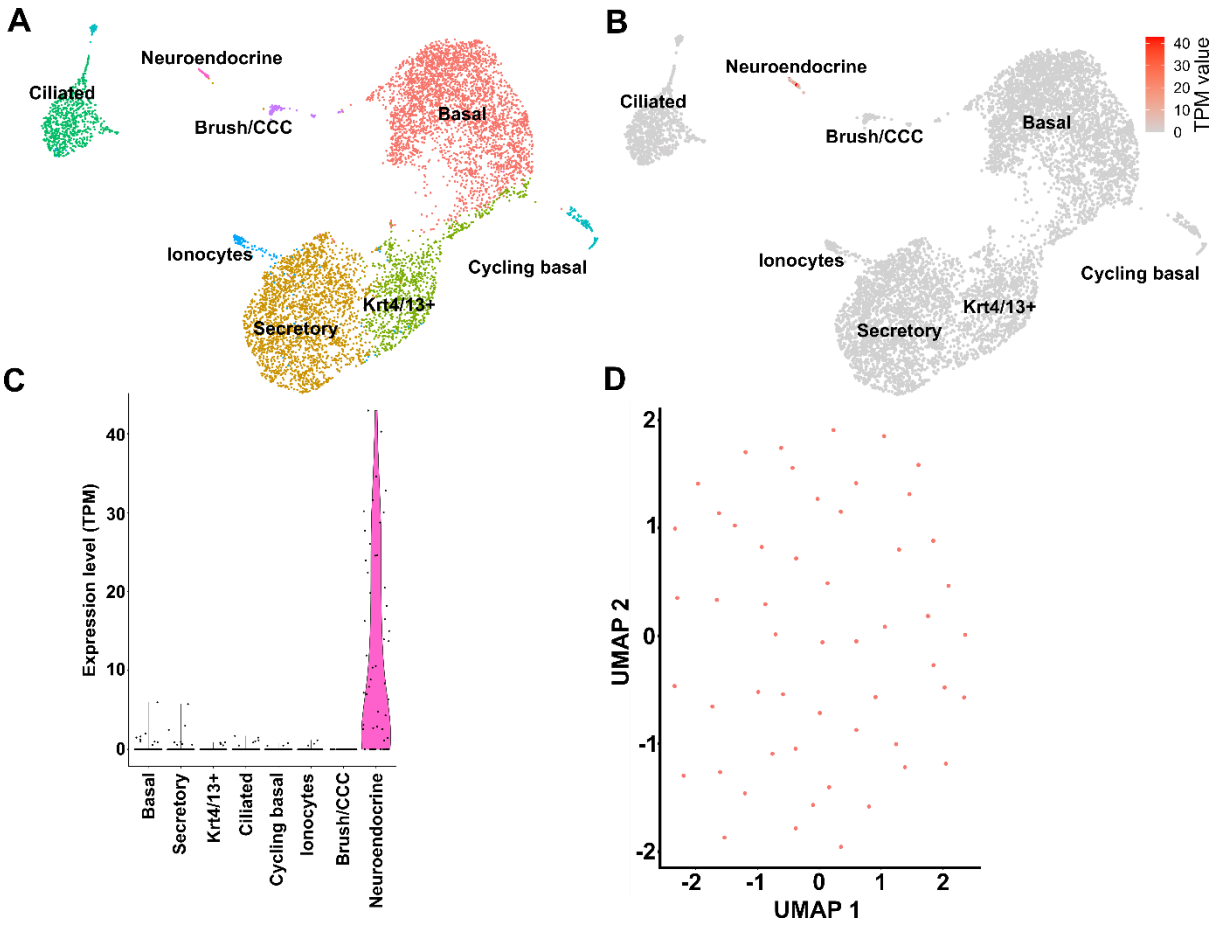

Figure 3.31: *In silico*-analysis of single cell mRNA sequencing data reveals *Cxcl13*-mRNA expression predominantly in neuroendocrine cells of the tracheal epithelium.
(A-D) *In silico*-analysis of published sequencing data of murine tracheal epithelial cells [5]. ***(A)*** SPRING plot (UMAP) shows eight distinct cell clusters, namely basal, secretory, Krt4/13^{+}, ciliated, ionocytes, solitary chemosensory (brush/tuft), cycling basal and neuroendocrine cells. ***(B and C)*** SPRING and violin plots, respectively. *Cxcl13*-mRNA is predominantly expressed within the neuroendocrine cell cluster. ***(D)*** UMAP, each dot represents a single analyzed neuroendocrine cell, no subclustering of neuroendocrine cells was possible based on distinct gene expression patterns.

We were not able to subcluster the neuroendocrine cells based on distinct gene expression patterns (Figure 3.31D). Accordingly, we could not find any difference between *Cxcl13*$^{+}$ and *Cxcl13*$^{-}$ cells when we analyzed the highest expressed genes within all neuroendocrine cells (~100 genes, fold change >1), including commonly used neuroendocrine cell marker genes (e.g., *Ascl1, Uchl1, Calca, Chga, Chgb*) (Figure 3.32A). Further analysis revealed a panel of ~100 genes that showed a different expression level (fold change >2.5) between *Cxcl13*$^{+}$ and *Cxcl13*$^{-}$ cells. Among these genes, we could not find any gene which is known to be involved in CXCL13 signaling pathways, based on published data. *Ptp4A3* (Protein Tyrosine Phosphatase 4A3, PRL-3) was among the genes which were upregulated in *Cxcl13*$^{+}$ cells.

Ptp4A3 seemed to be strongly associated with the $CXCL13^+$ cell population (29/36 versus 3/17 in $CXCL13^-$ cells). Interestingly, *Robo1* was found among the differentially regulated genes, being upregulated in the $CXCL13^+$ cell population (15/36 versus 4/17 in $CXCL13^-$ cells). *Robo* is expressed in lung neuroendocrine cells, where it is required to restrict the number of immune cells in the lung and to cluster neuroendocrine cells into neuroepithelial bodies [18] (Figures 3.32B and 3.32C).

Together, these data demonstrate that neuroendocrine cells are the major source of CXCL13 within the murine tracheal epithelium at both protein and messenger RNA level. However, there are no distinct subpopulations of neuroendocrine cells.

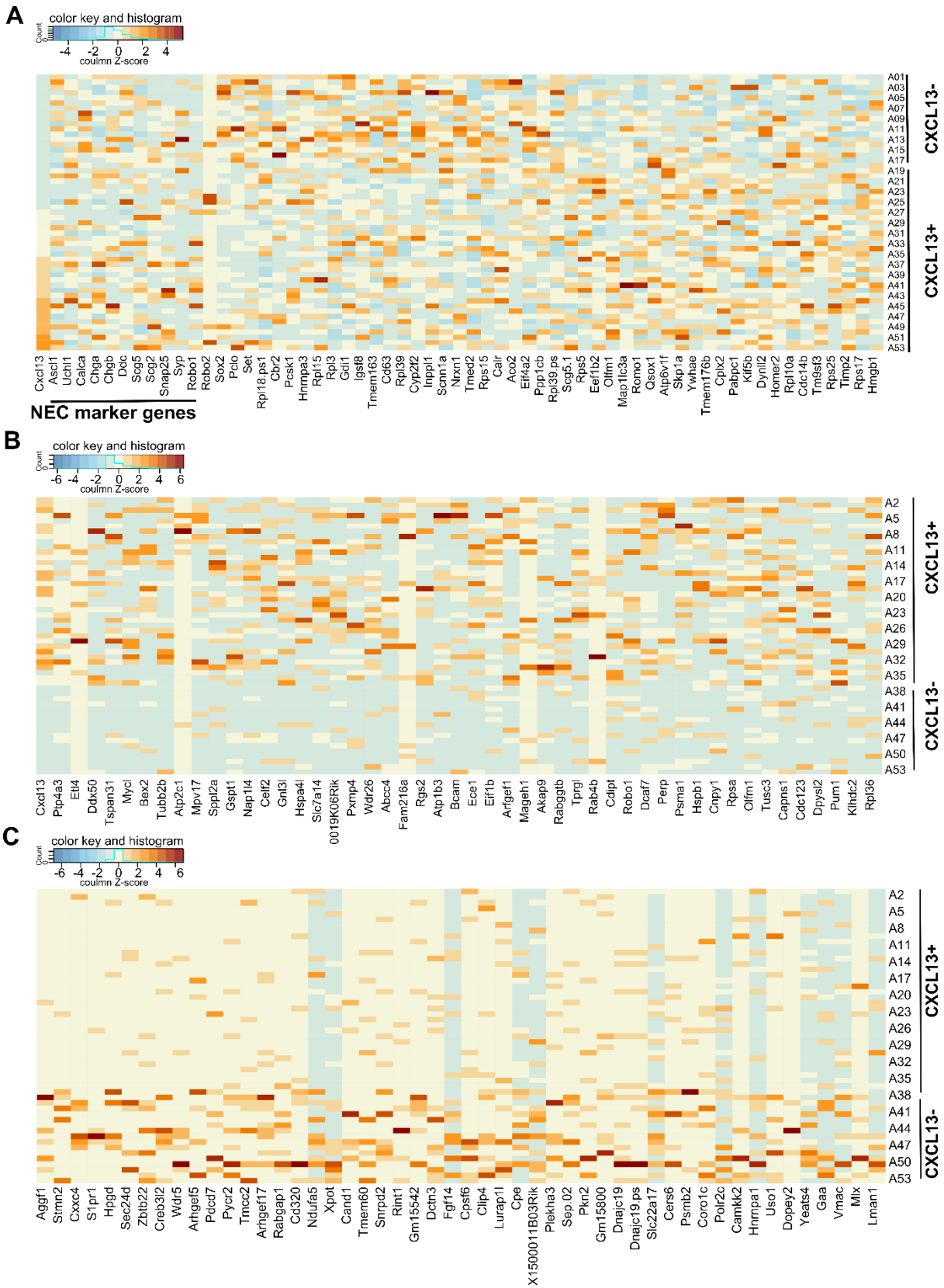

Figure 3.32: Differential gene expression pattern between CXCL13^{+} and CXCL13^{-} neuroendocrine cells.

(A) Heat map shows the most differential expressed genes (fold change >1) between CXCL13^{+} and CXCL13^{-} neuroendocrine cells among the 200 highest expressed genes within the neuroendocrine cell cluster. Typical neuroendocrine cell marker genes (*Ascl1*, *Uchl1*, *Calca*,

Chga, Chgb) are also included***. (B and C)*** Heat maps showing different expression levels (fold change >2.5) of genes between $CXCL13^+$ and $CXCL13^-$ neuroendocrine cells. The upper heat map ***(B)*** shows genes that are upregulated in $CXCL13^+$ cells, lower heat map ***(C)*** shows genes that are downregulated in $CXCL13^+$ cells.

3.2.1.4 CXCL13-immunoreactivity is detected ultrastructurally in neuroendocrine cells

Ultrastructural immunohistochemistry with antibodies against CGRP and CXCL13 showed immunoreactivity in cells with neuroendocrine cell features, like basal accumulations of dense core vesicles (ultrastructural features of the solitary neuroendocrine cell were fully described in section 3.1.1.2).

CGRP-immunoreactive cells contained numerous vesicles; their average short and long central axes diameters were 75 and 90 nm, respectively (69 vesicles, n=2 cells). The DAB reaction product was patchily distributed in the cytoplasm, the nucleus, and in some vesicles (Figure 3.33A). No labeling was detected in the corresponding control without primary antibody (Figure 3.33B).

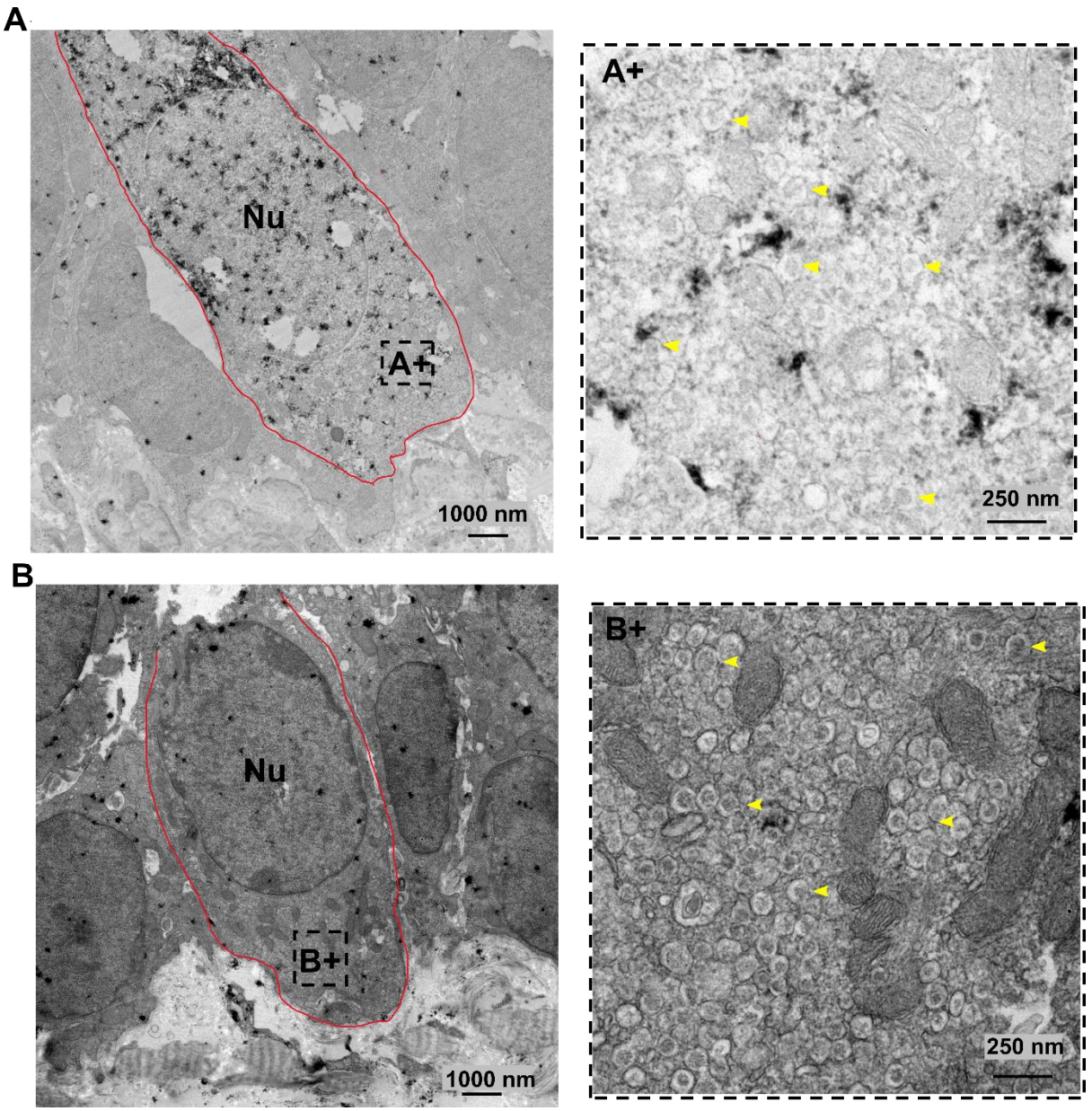

Figure 3.33: CGRP-immunoreactivity is detected ultrastructurally in neuroendocrine cells of C57BL/6RJ animal.
Transmission electron microscopy. ***(A)*** Ultrastructural immunohistochemistry with an antibody against CGRP shows an immunoreactive flask-shaped cell with DAB depositions in the cytoplasm and nucleus (Nu). (A+) is a higher magnification of the boxed area in the basal region of the cell showing dense core vesicles (arrowheads). ***(B)*** Omission of the primary antibody (CGRP), no labeling is visible in a neuroendocrine cell. (B+) is a higher magnification of the boxed area in the basal region of the cell, showing dense core vesicles (arrowheads).

CXCL13-immunoreactive cells also contained numerous vesicles. Their average short and long central axes diameters were 76 and 91 nm, respectively (174 vesicles, n=5 cells). The DAB reaction product was diffusely detected in the cytoplasm and in some vesicles (Figure 3.34).

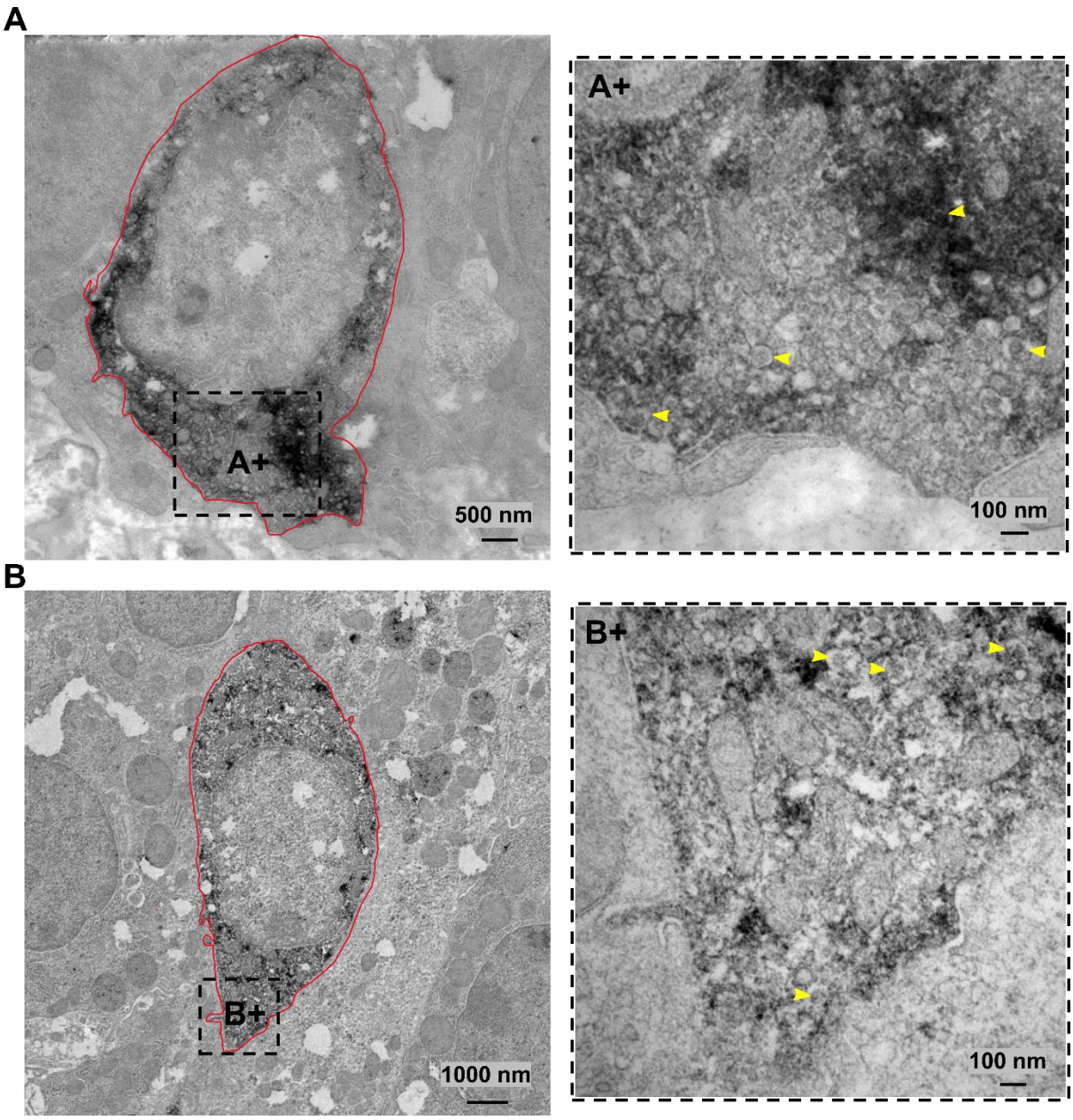

Figure 3.34: CXCL13-immunoreactivity is detected ultrastructurally in neuroendocrine cells of C57BL/6RJ animal.
(A and B) Transmission electron microscopy, ultrastructural immunohistochemistry with an antibody against CXCL13, shows immunoreactive cells with diffuse DAB depositions in the cytoplasm. (A+ and B+) are a higher magnification of the boxed areas in the basal region of the corresponding cell, showing dense core vesicles (arrowheads).

No specific labeling was detected in the corresponding control without CXCL13 primary antibody (Figure 3.35).

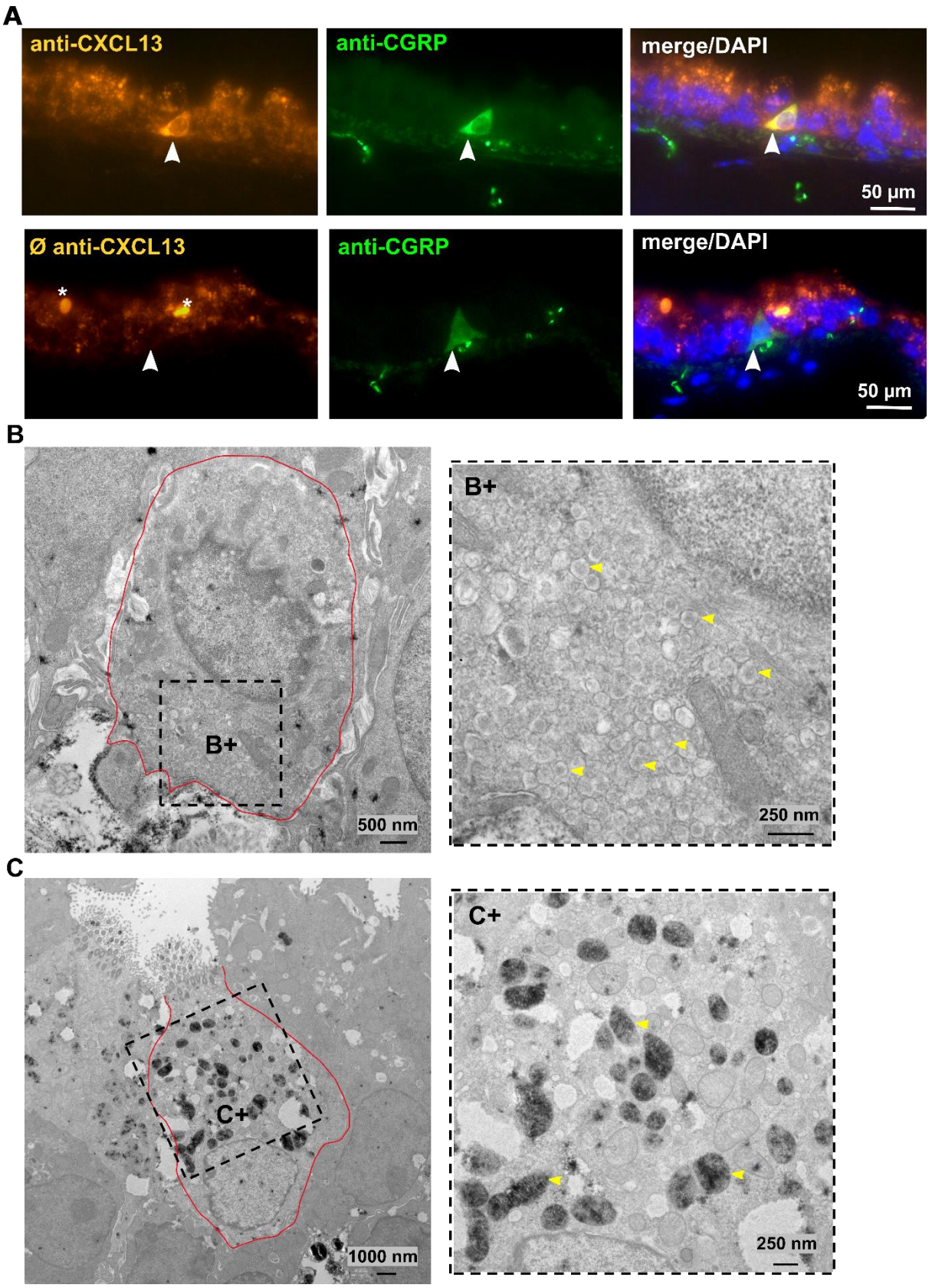

Figure 3.35: Validation of the antibodies used in CXCL13 immunoelectron microscopical experiments (Tracheas from from C57BL/6RJ animals).
Control experiment for the experiments in Figure 3.34, in which biotinylated secondary antibodies were used. ***(A)*** Immunohistochemistry of tracheal cryosections, to test for unspecific

labeling of endogenous biotin. CGRP antibody was used as a marker to identify neuroendocrine cells. The upper panel shows labeling of neuroendocrine cells with antibodies against CXCL13 and CGRP (arrowhead). Lower panel, omission of primary antibody (CXCL13), no unspecific labeling of the neuroendocrine cell ($CGRP^+$, arrowhead) caused by the biotinylated secondary antibody is visible; unspecific labeling is detected in other cell types (asterisk). Images captured with color camera; true colors are shown. ***(B and C)*** Transmission electron microscopy. Omission of the primary antibody (CXCL13). ***(B)*** No labeling is detected in a neuroendocrine cell. (B+) is a higher magnification of the boxed area in the basal region of the cell, showing dense core vesicles (arrowheads). ***(C)*** Ciliated cell with unspecific labeling of mitochondria caused by the secondary (biotinylated antibody) and tertiary reagents (peroxidase-conjugated streptavidin) which were used in this experiment. (C+) is a higher magnification, showing reactive mitochondria (arrowheads).

3.2.2 CXCL13 is expressed by a small subpopulation of solitary and clustered broncho-pulmonary neuroendocrine cells in the mouse lung

CXCL13-immunoreactive cells which were also CGRP-immunoreactive were detected in the epithelium of the extra- and intrapulmonary airways below the bifurcation (Figure 3.36). Broncho-pulmonary CXCL13-immunoreactive epithelial cells were either solitary neuroendocrine cells (Figures 3.36B and 3.36C) or part of neuroepithelial bodies (NEB was considered as a group of ≥ 2 cells) (Figure 3.36A).

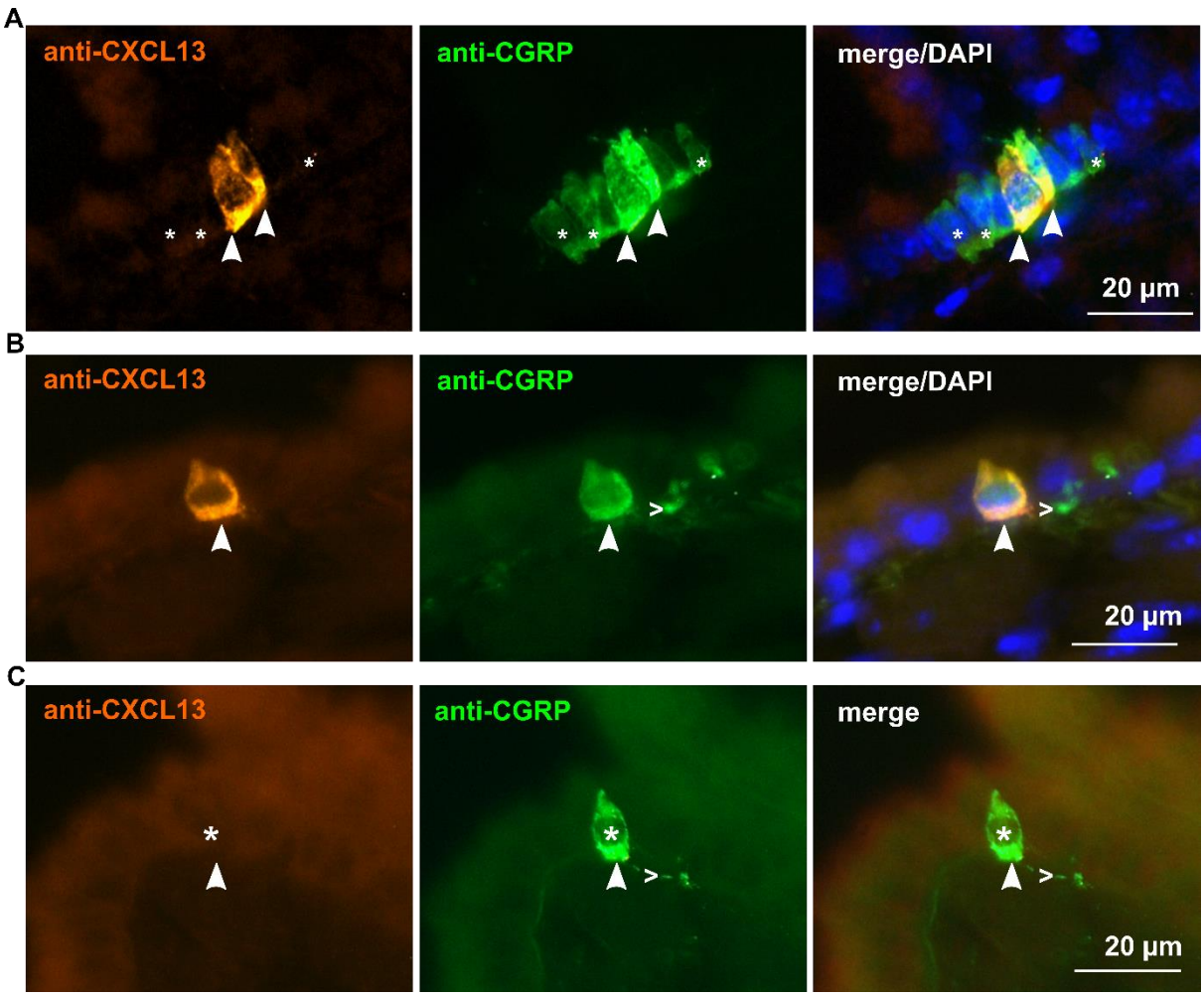

Figure 3.36: CXCL13 is expressed by a small subpopulation of solitary and clustered broncho-pulmonary neuroendocrine cells in the mouse lung of C57BL/6RJ animals.
(A-C) Immunohistochemistry of lung cryosections with antibodies against CXCL13 (orange) and CGRP (green), showing the different phenotypes of broncho-pulmonary neuroendocrine cells. ***(A)*** NEB consisting of more than 5 cells, 2 of them are $CGRP^+/CXCL13^+$ (arrowheads), in addition to $CGRP^+/CXCL13^-$ cells (asterisk). ***(B)*** A solitary neuroendocrine cell in the broncho-pulmonary epithelium co-labeled with antibodies against CXCL13 and CGRP (arrowhead); $CGRP^+$ nerve fibers are indicated by (>). ***(C)*** A solitary neuroendocrine cell in the broncho-pulmonary epithelium is only labeled with an antibody against CGRP (arrowheads). $CGRP^+$ nerve fibers are indicated by (>). Images captured with color camera; true colors are shown.

3.2.3 CXCL13 defines a neuroendocrine cell phenotype in the murine trachea and lung

3.2.3.1 Tracheal neuroendocrine cell phenotypes based on CXCL13 expression

In the trachea, neuroendocrine cells almost always lay solitary and only rarely appeared as a couple of two neighboring cells.

Immunolabeling of tracheal sections with antibodies against the neuroendocrine cell marker CGRP and CXCL13 defined 2 phenotypes of tracheal neuroendocrine cells: solitary $CXCL13^+$ (60.8%, 251/413 cells) and solitary $CXCL13^-$ (26.9%, 111/413) $CGRP^+$ neuroendocrine cells. In this approach, an additional 12.3% (51/413) of immunoreactive cells were single positive for CXCL13, as illustrated in Figures 3.37A and 3.37D.

Immunolabeling of tracheal whole mounts with antibodies against CXCL13 and the neuroendocrine cell markers PGP9.5 or CGRP, respectively, also defined two phenotypes. Taking PGP9.5 as marker, 69.3% (1561/2254 cells, median=99.3, mean±SEM 100.9±16.4 cells/mm^2) were $PGP9.5^+/CXCL13^+$ and 30.7% (693/2254 cells, median=37.6, mean±SEM=44.9±7.5 cells/mm^2) were $PGP9.5^+/CXCL13^-$ (n=5 mice) (Figures 3.25A, 3.37B and 3.37E). Taking CGRP as marker, 73.3%, (1942/2650 cells, median=135.3, 120.9±14.1 cells/mm^2) were $CGRP^+/CXCL13^+$, 21.7% (576/2650 cells, median=34.4; mean±SEM=35.6±5.6 cells/mm^2) were $CGRP^+/CXCL13^-$ and 5% (132/2650 cells, median=8.9, mean±SEM=8.1±3.4 cells/mm^2) were $CGRP^-/CXCL13^+$ (n=5 mice) (Figures 3.25B and 3.37C and 3.37F).

The percentages of $CXCL13^+/CGRP^+$ recorded from tissue sections (60.8%; 251/413 cells) were slightly lower than those recorded from whole mount preparations (73.3%; 1942/2650 cells), but this difference was not statistically significant (p=0.3668, Chi-square test, n=5) (Figures 3.37D, 3.37F and 3.37G).

The percentage of colocalization between CXCL13 and either PGP9.5 or CGRP in whole mount tracheas was comparable (69.3% and 73.3%) (Figures 3.37E, 3.37F and 3.37H).

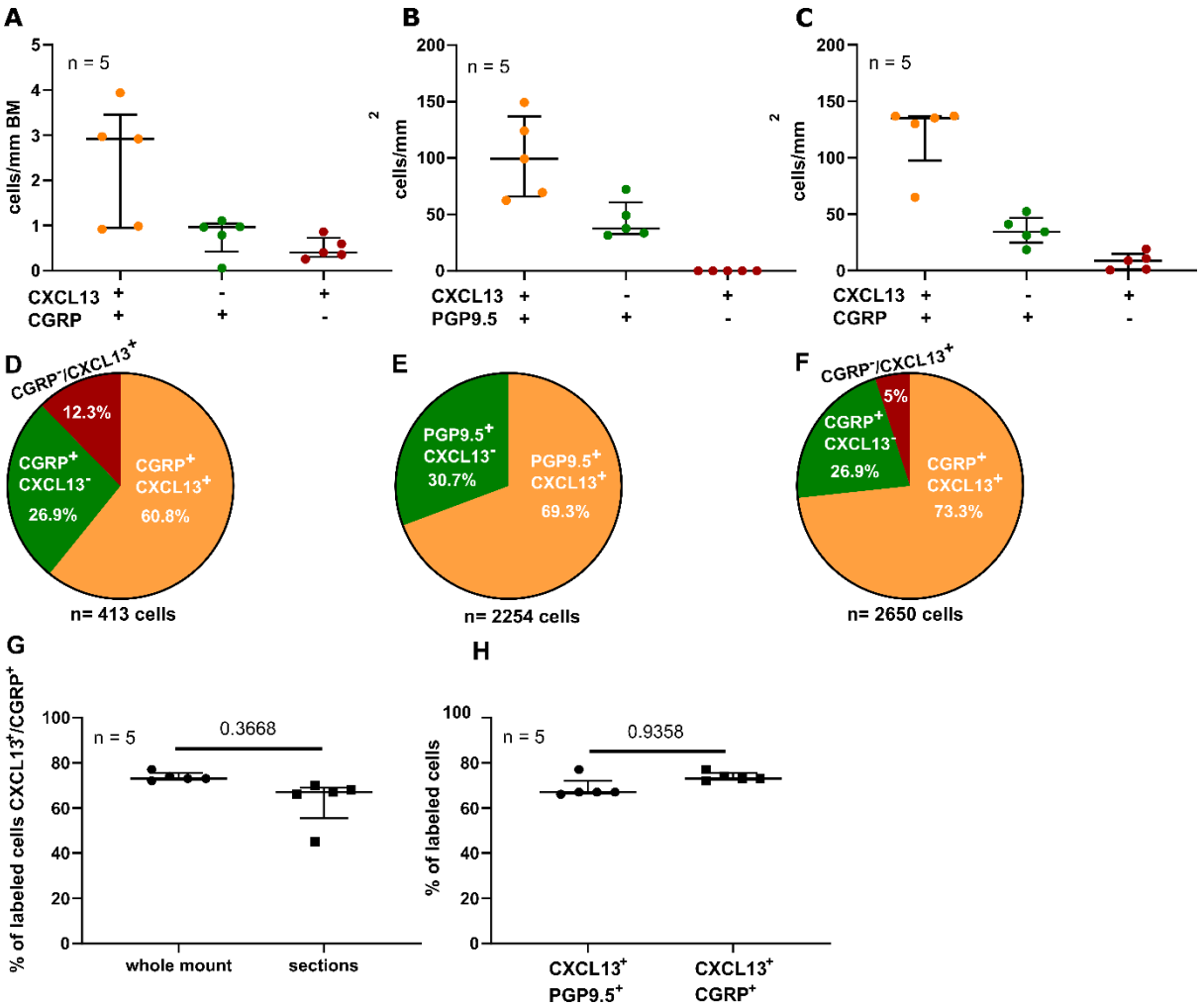

Figure 3.37: Tracheal neuroendocrine cell phenotypes based on CXCL13 expression in C57BL/6RJ animals.

(A-C, G and H) Scatter dot plots with median and interquartile range bars, showing the mean value for each investigated trachea. All tracheas, either in whole mount or in cryosections, were double-labeled with antibodies against CXCL13 and either PGP9.5 or CGRP**.** ***(A)*** Quantification of immunoreactive cells in tracheal cryosections (4 longitudinal sections/trachea, n=5 tracheas), showing the number of cells/mm of the basement membrane (BM). ***(B and C)*** Quantification of immunoreactive cells in tracheal whole mounts (n=5 tracheas), showing the number of cells/mm^2. ***(D-F)*** Pie charts showing the percentages of phenotypes related to the pooled total number of immunoreactive cells recorded in experiments illustrated in A to C, respectively. ***(G)*** Experiments illustrated in A and C were performed using different tracheal preparation techniques (whole mount and tracheal cryosections); no significant difference in the relative frequency of CGRP$^+$/CXCL13$^+$ cells is detected between these techniques (whole mount: median=73, mean±SEM 73.8±0.9%, cryosections: median=67, mean±SEM=63.2±4.6%, p=0.3668, Chi-square test, n=5). ***(H)*** Based on the experiments illustrated in B and C, the relative frequencies of PGP9.5$^+$/CXCL13$^+$ and CGRP$^+$/CXCL13$^+$ cells are comparable (median=67% and 73%, respectively, mean±SEM=68.8±2% and 73.8±0.9%, respectively, p=0.9358, Chi-square test; n=5 tracheas).

3.2.3.2 Broncho-pulmonary neuroendocrine cell phenotypes based on CXCL13 expression

In contrast to the solitary neuroendocrine cells in tracheal epithelium, neuroendocrine cells in broncho-pulmonary epithelium predominantly clustered to neuroepithelial bodies. It was found that only 4.7% of all $CGRP^+$ cells were solitary neuroendocrine cells (73/1548 cells from 5 animals) and 95.3% (1475/1548 cells) of all $CGRP^+$ cells were part of neuroepithelial bodies (Figures 3.36 and 3.38).

Quantitative analysis of lung cryosections showed four phenotypes: (1) solitary neuroendocrine cells which were either $CXCL13^+$ (8.2%, 6/73 cells) or (2) $CXCL13^-$ (91.8%, 67/73 cells), and neuroepithelial bodies in which the cells were (3) $CXCL13^+$ (5.6%, 82/1475 cells) or (4) $CXCL13^-$ (94.4%, 1393/1475 cells) (Figures 3.36 and 3.38). These data were obtained from longitudinal sections including trachea and lung, which were analyzed simultaneously (n=5 mice).

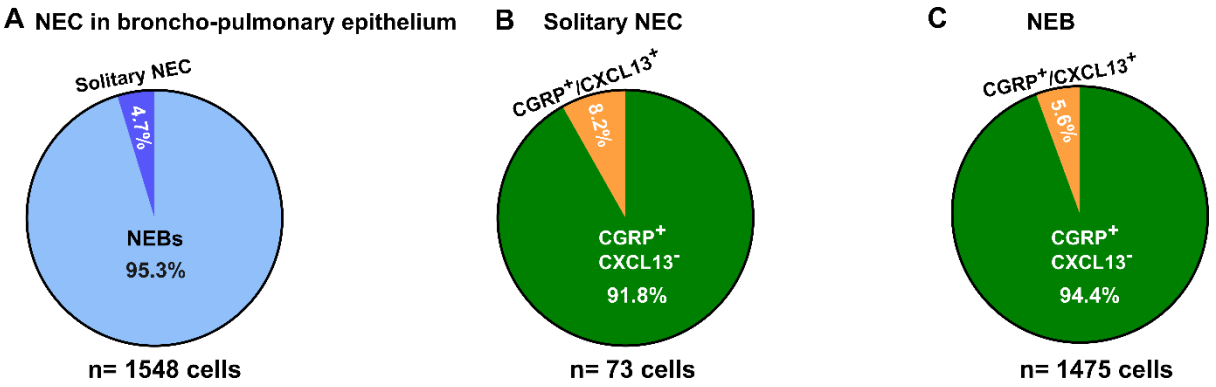

Figure 3.38: Broncho-pulmonary neuroendocrine cell phenotypes based on CXCL13 expression in C57BL/6RJ animals.
(A-C) Lung cryosections were immunolabeled with antibodies against CGRP and CXCL13, cells were pooled from 5 animals**.** ***(A)*** The minority (4.7%) of all $CGRP^+$ cells are solitary neuroendocrine cells and 95.3% of all $CGRP^+$ cells are part of neuroepithelial bodies. ***(B)*** Only 8.2% of all solitary CGRP-immunoreactive cells are co-labeled with CXCL13 antibody. ***(C)*** Only 5.6% of all CGRP-immunoreactive cells within the neuroepithelial bodies are co-labeled with the CXCL13 antibody.

3.3 Impact of Pou2f3 transcription factor on the neuroendocrine cells in the murine tracheal epithelium

3.3.1 Pou2f3 is required for the development of cholinergic chemosensory cells

The development of TRPM5-positive chemosensory cells is critically dependent on the transcription factor Pou2f3. Genetic deletion of *Pou2f3* results in general absence of TRPM5-positive chemosensory cells, including the tracheal epithelium [32]. In oropharyngeal taste buds, the lack of TRPM5-positive type II taste cells is accompanied by increased numbers of type III taste cells in *Pou2f3*$^{-/-}$ mice [152–154]. This set of experiments aimed to determine whether the impact of Pou2f3 on tracheal epithelial development also extends beyond block of generation of TRPM5-positive cells. In our material, quantitative analysis of TRPM5-immunoreactive epithelial cells in tracheal whole mounts showed no difference between *Pou2f3*$^{+/-}$ and wild-type *Pou2f3*$^{+/+}$ mice (median=245 versus 256.4, mean±SEM=219.7±20.8 versus 215.7±41.2 cells/mm², n=5 and 3 mice, respectively, $p>0.999$, Mann Whitney test) (Figure 3.39), whereas no immunoreactivity to TRPM5 was detected at all in *Pou2f3*$^{-/-}$ mice (n=5 mice) (Figures 3.39C and 3.39D). (This quantification was done by Alexander Perniss, Institute for Anatomy and Cell Biology, Justus Liebig University Giessen, Germany).

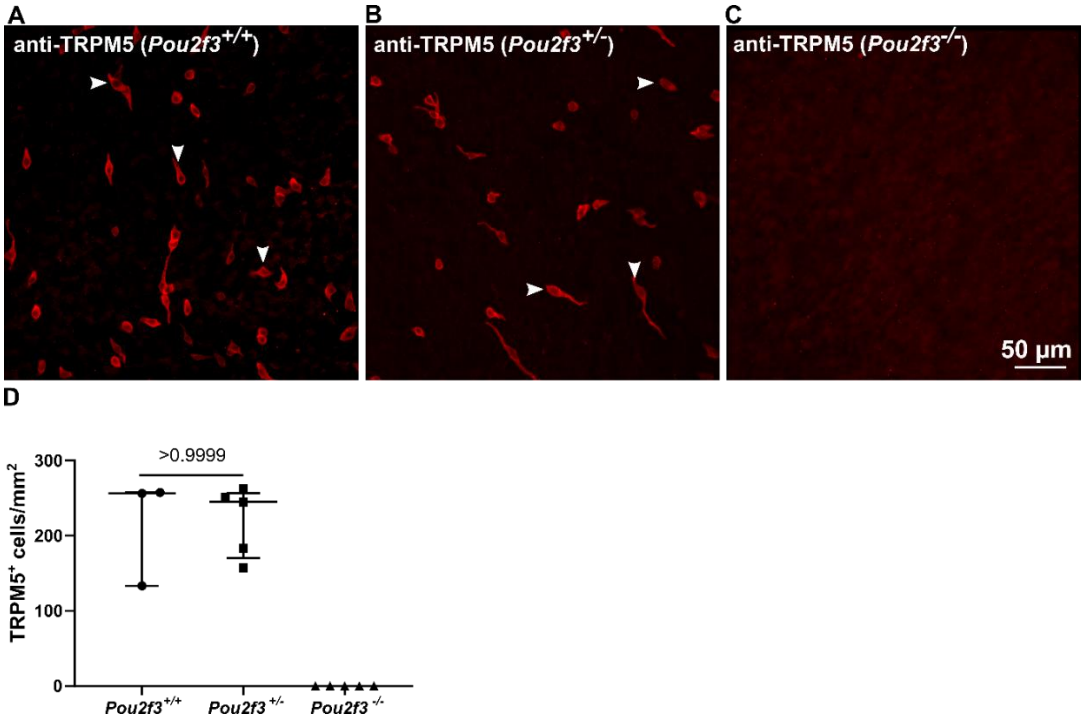

Figure 3.39: Cholinergic chemosensory cells in the tracheal epithelium of *Pou2f3*$^{+/+}$, *Pou2f3*$^{+/-}$ and *Pou2f3*$^{-/-}$ mice.
(A-C) CLSM, maximum intensity projection of z-stack of confocal optical sections. Tracheal whole mount immunohistochemistry from *Pou2f3*$^{+/+}$, *Pou2f3*$^{+/-}$ and *Pou2f3*$^{-/-}$ mice with an antibody against TRPM5, labeling cholinergic chemosensory cells***. (A and B)*** TRPM5-immunoreactive cells (arrowheads). ***(C)*** No immunoreactivity to TRPM5 in a *Pou2f3*$^{-/-}$ mouse. ***(D)*** Scatter dot plot with median and interquartile range bars, showing mean value for each investigated trachea for the experiment illustrated in A, B and C. Quantification of immunoreactive cells in tracheal whole mounts, shows no difference between *Pou2f3*$^{+/-}$ and wild-type *Pou2f3*$^{+/+}$ mice (Mann Whitney test). No immunoreactivity to TRPM5 is detected in *Pou2f3*$^{-/-}$ mice (n=5).

3.3.2 Neuroendocrine cell hyperplasia in *Pou2f3*$^{+/-}$ and *Pou2f3*$^{-/-}$ mice

The neuroendocrine cell population of the trachea was analyzed by counting PGP9.5-, CGRP- and CXCL13-immunoreactive epithelial cells in tracheal whole mounts (Figures 3.40-3.42).

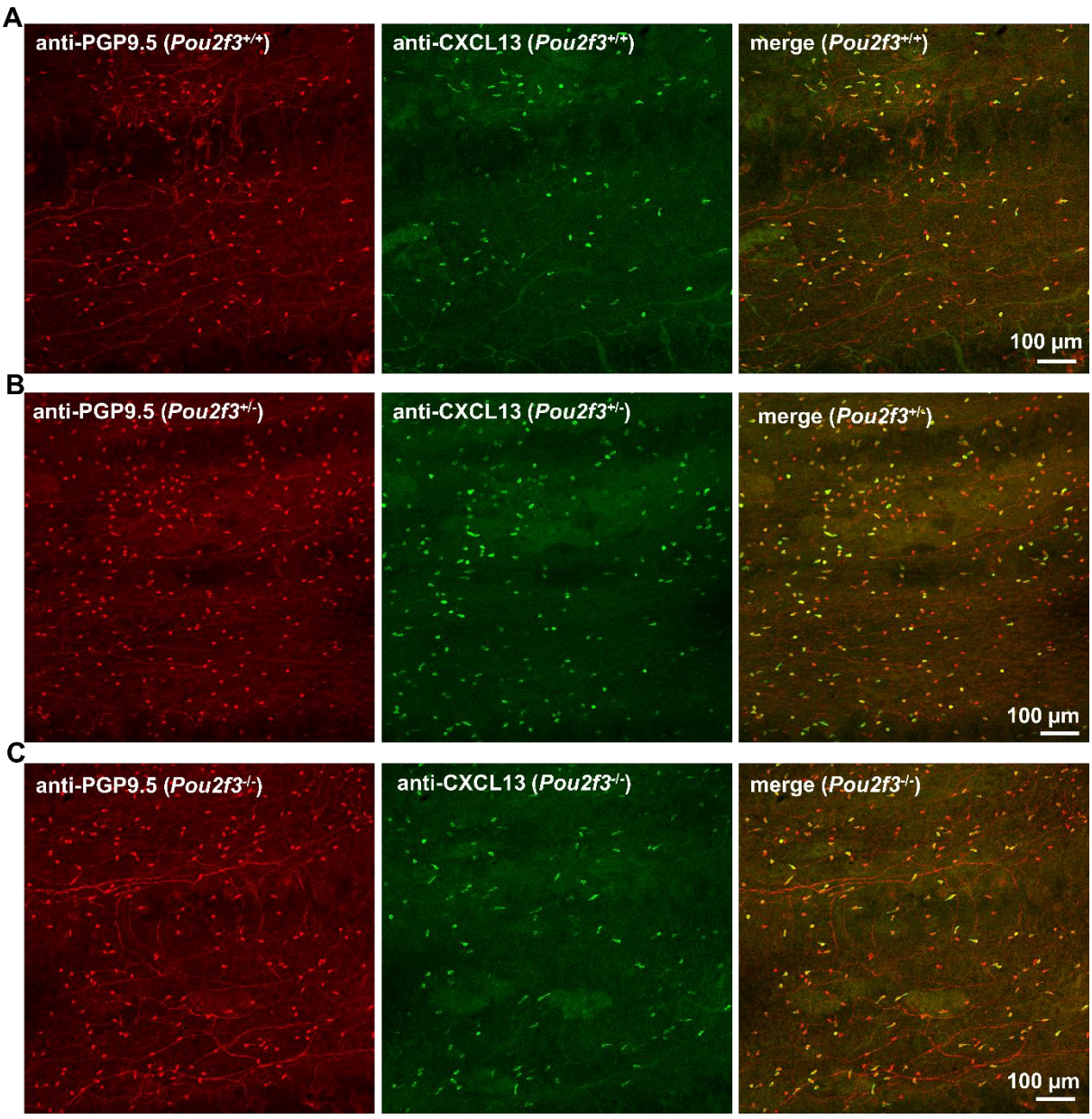

Figure 3.40: Neuroendocrine cell hyperplasia in *Pou2f3*$^{+/-}$ and *Pou2f3*$^{-/-}$ mice.
(A-C) CLSM, single confocal optical section, tracheal whole mount immunohistochemistry with antibodies against PGP9.5 and CXCL13, labeling neuroendocrine cells, showing immunoreactive cells from the same region (3rd and 4th intercartilage regions). Less immunoreactive cells in *Pou2f3*$^{+/+}$ (A) than in *Pou2f3*$^{+/-}$ (B) and *Pou2f3*$^{-/-}$ mice (C).

3.3.2.1 PGP9.5-immunoreactive tracheal epithelial cells

PGP9.5-immunoreactive cells were increased in in *Pou2f3*$^{+/-}$ (median=307.6, mean±SEM=323.1±22.7 cells/mm², n=9, p=0.0003, Kruskal-Wallis test) and *Pou2f3*$^{-/-}$ mice (median=285.3, mean±SEM=301.7±26.2 cells/mm², n=11, p=0.0046, Kruskal-Wallis test) compared to wild-type *Pou2f3*$^{+/+}$ mice (median=193.4, mean±SEM=198.8±9.6 cells/mm², n=11) (Figures. 3.40, 3.41 and 3.42A). The analysis showed no significant difference in the

number of PGP9.5-immunoreactive cells between *Pou2f3*$^{+/-}$ and *Pou2f3*$^{-/-}$ mice (p>0.9999, Kruskal-Wallis test) (Figure 3.42A).

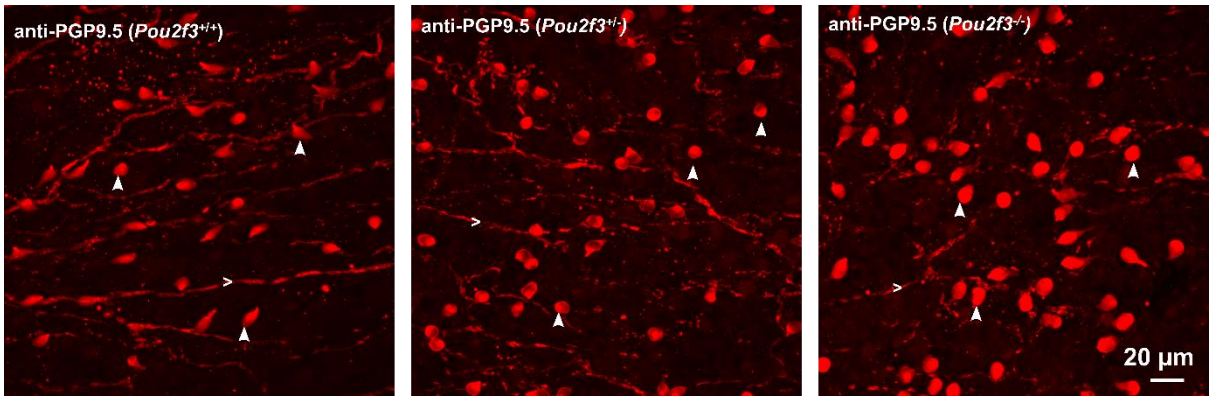

Figure 3.41: PGP9.5-immunoreactive cells are increased in *Pou2f3*$^{+/-}$ and *Pou2f3*$^{-/-}$ mice. CLSM, maximum intensity projection of z-stack of confocal optical sections. Tracheal whole mount immunohistochemistry with antibodies against PGP9.5, labeling neuroendocrine cells (arrowheads) and nerve fibers (>), showing PGP9.5-immunoreactive cells from the same region (3rd intercartilage region). Less PGP9.5-immunoreactive cells in *Pou2f3*$^{+/+}$ than in *Pou2f3*$^{+/-}$ and *Pou2f3*$^{-/-}$ mice.

The quantification revealed no significant difference in the number of PGP9.5-immunoreactive cells in wild-type *Pou2f3*$^{+/+}$ mice (median=193.4, mean±SEM=198.8±9.6 cells/mm², n=11) compared to wild-type C57BL/6Rj mice (median=148.6, mean±SEM=145.8±23 cells/mm², n=5; p=0.0897, Mann Whitney test) (Figure 3.42B).

3.3.2.2 CGRP-immunoreactive tracheal epithelial cells

CGRP-immunoreactive cells were increased in *Pou2f3*$^{+/-}$ (median=319.8, mean±SEM 357±37.5 cells/mm², n=5, p=0.0056, Kruskal-Wallis test) and *Pou2f3*$^{-/-}$ mice (median=283.8, mean±SEM=289.6±33.4 cells/mm², n=5, p=0.0851, Kruskal-Wallis test) compared to wild-type C57BL/6Rj mice (median=168.3, mean±SEM=156.4±18.7 cells/mm², n=5) (Figure 3.42C). The analysis showed no significant difference in the number of CGRP-immunoreactive cells between *Pou2f3*$^{+/-}$ and *Pou2f3*$^{-/-}$ mice (p>0.9999, Kruskal-Wallis test) (Figure 3.42C).

3.3.2.3 CXCL13-immunoreactive tracheal epithelial cells

CXCL13-immunoreactive cells were increased in *Pou2f3*$^{+/-}$ (median=265.5, mean±SEM=274.4±21.5 cells/mm², n=10, p=0.0012, Kruskal-Wallis test) and *Pou2f3*$^{-/-}$ mice (median=219.8, mean±SEM=236.8±21 cells/mm², n=11, p=0.0201, Kruskal-Wallis test) compared to wild-type *Pou2f3*$^{+/+}$ mice (median=145.8, mean±SEM=145.3±13.4 cells/mm², n=8) (Figures 3.40 and 3.42D). The analysis showed no significant difference in the number of

CXCL13-immunoreactive cells between *Pou2f3*$^{+/-}$ and *Pou2f3*$^{-/-}$ mice (p>0.9999, Kruskal-Wallis test) (Figure 3.42D).

The quantification revealed no significant difference in the number of CXCL13-immunoreactive cells in wild-type *Pou2f3*$^{+/+}$ mice (median=145.8, mean±SEM=145.3±13.4 cells/mm², n=8) compared to wild-type C57BL/6Rj mice (median=130, mean±SEM=114.9±11.8 cells/mm², n=10; p=0.2031, Mann Whitney test) (Figure 3.42E).

The extent of colocalization of PGP9.5- and CXCL13-immunoreactivities remained constant among these mouse strains and accounted for 69.3% (1561/2254 cells, n=5), 60.3% (4287/7107 cells, n=8), 65.8% (3744/5689 cells, n=5) and 62.5% (4980/7970 cells, n=6) in C57BL/6Rj, *Pou2f3*$^{+/+}$, *Pou2f3*$^{+/-}$ and *Pou2f3*$^{-/-}$ mice, respectively (Figure 3.42F).

Likewise, the extent of colocalization of CGRP- and CXCL13-immunoreactivities was also preserved: 78.1% (4535/5806 cells, n=5) in *Pou2f3*$^{+/-}$ and 79.8% (4004/5015 cells, n=5) in *Pou2f3*$^{-/-}$ mice, compared to 73.3% (1942/2650 cells, n=5) in wild-type C57BL/6Rj mice (Figure 3.42G).

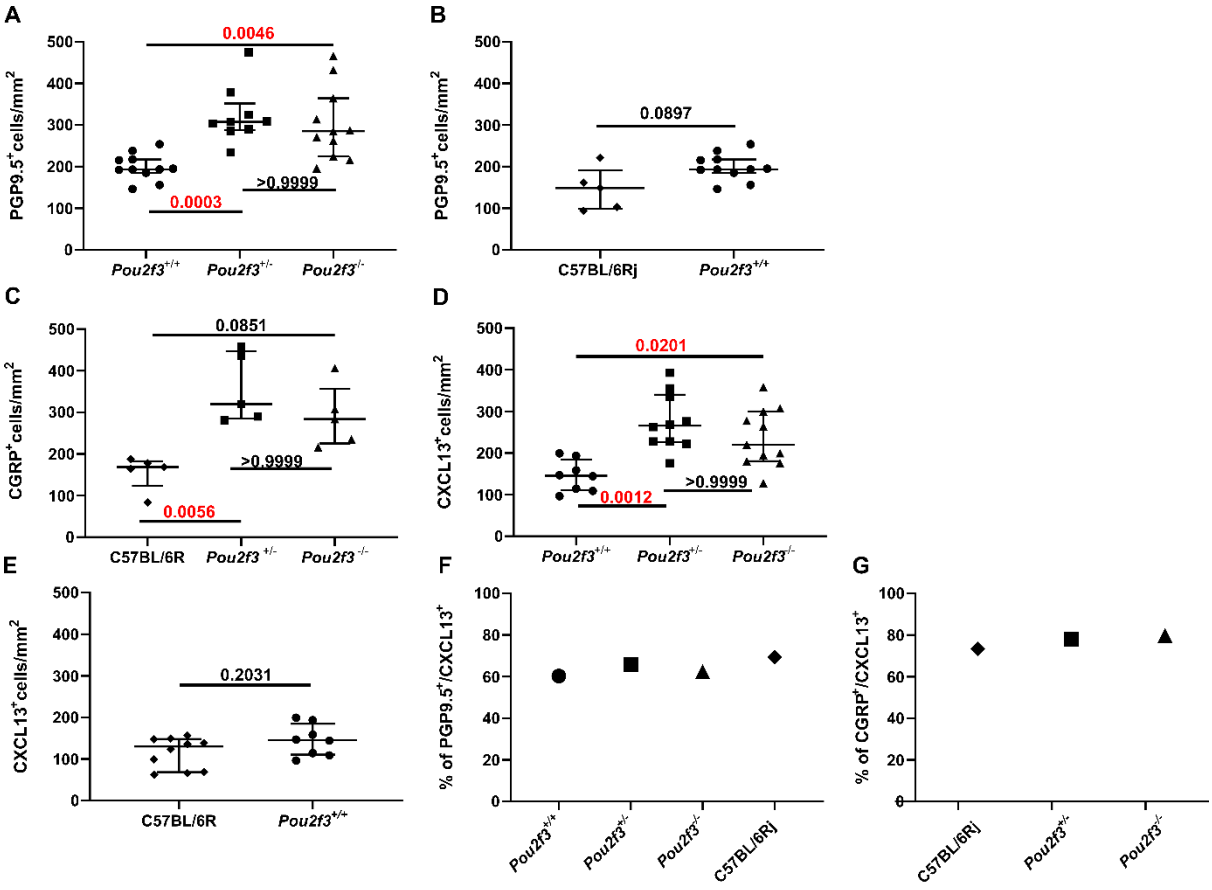

Figure 3.42: Tracheal neuroendocrine cell hyperplasia in *Pou2f3*$^{+/-}$ and *Pou2f3*$^{-/-}$ mice.
(A-E) Scatter dot plots with median and interquartile range bars, showing the mean value for each investigated trachea. Whole mount tracheas from wild-type (C57BL/6Rj or *Pou2f3*$^{+/+}$), *Pou2f3*$^{+/-}$ and *Pou2f3*$^{-/-}$ were immunolabeled with antibodies against PGP9.5 or CGRP and CXCL13. ***(A)*** Quantification of PGP9.5^{+}-immunoreactive cells in wild-type *Pou2f3*$^{+/+}$ (n=11), *Pou2f3*$^{+/-}$ (n=9) and *Pou2f3*$^{-/-}$ (n=11). Multi comparison Kruskal-Wallis test. ***(B)*** Quantification of PGP9.5^{+}-immunoreactive cells in wild-type C57BL/6Rj (n=5) and *Pou2f3*$^{+/+}$ (n=11). Mann Whitney test. ***(C)*** Quantification of CGRP-immunoreactive cells in wild-type C57BL/6Rj (n=5), *Pou2f3*$^{+/-}$ (n=5) and *Pou2f3*$^{-/-}$ (n=5). Multi comparison Kruskal-Wallis test. ***(D)*** Quantification of CXCL13-immunoreactive cells in *Pou2f3*$^{+/+}$ (n=8), *Pou2f3*$^{+/-}$ (n=10) and *Pou2f3*$^{-/-}$ (n=11). Multi comparison Kruskal-Wallis test ***(E)*** Quantification of CXCL13^{+}-immunoreactive cells in wild-type C57BL/6Rj (n=10) and *Pou2f3*$^{+/+}$ (n=8). Mann Whitney test. ***(F)*** Shows the percentage of PGP9.5 and CXCL13 colocalization based on the pooled total number of immunoreactive cells in tracheal whole mounts of *Pou2f3*$^{+/+}$ (4287/7107 cells, n=8), *Pou2f3*$^{+/-}$ (3744/5689 cells, n=5), *Pou2f3*$^{-/-}$(4980/7970 cells, n=6) and C57BL/6Rj (1561/2254 cells, n=5) mice. ***(G)*** Shows the percentage of CGRP and CXCL13 colocalization based on the pooled total number of immunoreactive cells in the tracheal whole mount of C57BL/6Rj (1942/2650 cells, n=5), *Pou2f3*$^{+/-}$ (4535/5806 cells, n=5) and *Pou2f3*$^{-/-}$ (4004/5015 cells, n=5) mice.

4 Discussion

4.1 Villin expression is restricted to the neuroendocrine cells in the murine lower airway epithelium

In this study, we defined the identity of poorly defined villin-immunoreactive cells, which have been reported previously in the murine trachea [7, 32]. These cells are neither a new epithelial cell type nor a brush cell phenotype. By applying immunohistochemistry, *in silico*-analysis of publicly available sequencing data sets, RT-PCR and immunohistochemical characterization of tissues obtained from *Vil1-Cre* mice, we identified the specific expression of villin in a subpopulation of neuroendocrine cells. Furthermore, our attempt to investigate the ultrastructure of the poorly defined villin-immunoreactive cells in the trachea of *Pou2f3*$^{-/-}$ mice revealed cells with neuroendocrine cell features as the only rare microvillous epithelial cell type. This approach was chosen on the rationale that rare microvillus epithelial cell types including poorly defined villin-immunoreactive cells and neuroendocrine cells persist in *Pou2f3*$^{-/-}$mice, but cholinergic chemosensory cells (brush cells) are absent [32]. Since only cells with basally accumulating dense core vesicles remained in this approach, the presumed ill-defined cells must be among them, representing neuroendocrine cells.

Double-labeling experiments with antibodies against PGP9.5 (neuroendocrine cell marker) and villin revealed that approximately two thirds of wild-type (C57BL/6RJ) tracheal neuroendocrine cells express villin, whilst a third is villin-negative. In contrast to this, immunolabeling of tracheal sections from *Vil1-Cre*$^{+}$*/ROSA*$^{mT/mG}$ reporter mice with antibodies against PGP9.5 and eGFP (to enhance fluorescence of villin-eGFP^{+} cells) revealed that approximately one third of tracheal neuroendocrine cells show *Vil1-Cre* activity, which is very consistent with *in silico*-analysis of available single cell RNA sequencing data, in which one third of neuroendocrine cell express *Vil1*-mRNA. One possible cause of the discrepancy in the expression of villin protein in wild-type and the endogenous expression of the driver gene (*Vil1*) in the reporter mice might be that villin is a structural protein with a long half-lifetime, so it can be visible by immunohistochemistry during a longer time of the cell life. In contrast, the reporter mice express eGFP under the *Vil1* promoter, and it might be that eGFP has a shorter lifetime than the villin protein. For example, the GFP was found to be stable with a half-life of ~26 h in cultured mouse LA-9 cells [167]. Alternatively, this difference may perhaps reflect a difference in villin expression between different mouse strains.

Another discrepancy was our observation in the broncho-pulmonary neuroendocrine cells, we observed also difference of eGFP expression of the reporter mice and endogenous expression of the driver gene. Some cells expressed eGFP, but on the protein level villin was not detected by immunolabeling of sections, neither from wild-type mice (C57BL/6RJ) nor *Vil1-Cre*$^{+}$*/ROSA*$^{mT/mG}$ reporter mice. Potential explanations for this discrepancy are: First, it might reflect ectopic *Cre*-expression in these cells. Second, villin protein expression might be too low to be detectable by immunohistochemistry. Third, *Vil1*-mRNA was not translated due to post-transcriptional silencing mechanism.

We also observed a cluster of cells expressing eGFP and being immunoreactive to villin, which means that villin also can be present at protein level in broncho-pulmonary neuroendocrine cells, but very rarely. RT-PCR also confirmed the expression of *Vil1* mRNA in the lung.

Our finding of limited *Vil1*-promoter-driven Cre recombinase activity to neuroendocrine cells in the lower airway epithelium suggests that functionally relevant *Vil1* gene expression and villin protein are only present in neuroendocrine cells. The function of villin and regulation of its expression in neuroendocrine cells still need to be investigated. For example, why it is expressed in a subpopulation of neuroendocrine cells but not in all? Is villin expression in neuroendocrine cells related to chemosensory and mechanosensory functions? Does it play a role in neuroendocrine cell migration during embryogenesis and cancer cell metastasis as it was reported in the intestinal and renal epithelial cell lines [59, 60].

4.2 Villin is not a cholinergic chemosensory cell marker in the murine trachea

Villin antibodies have been considered to serve as excellent immunohistochemical markers to identify brush cells in different species and organs [7, 8, 26, 32, 39, 40, 64, 65]. However, later studies showed that advillin is strongly and specifically expressed in intestinal brush cells and that advillin, rather than villin, is a brush cell marker in the mouse alimentary tract [62, 69, 71]. Likewise, cell-type-specific deletion of ChAT in tracheal chemosensory cells has been achieved by using *Avil-Cre* mice to generate *Avil*^{cre}:ChAT$^{fl/fl}$ mice [9], indicating that advillin is a brush cell marker also in the trachea. All these data suggest the possibility that the formerly published immunostaining of brush cells with villin antibodies might have resulted from cross-reactivity with advillin, which is likely a more specific brush cell marker [9, 62, 69, 71]. Indeed, there is a high structural similarity between advillin and villin, raising the possibility of antibody cross-reactivity. Structurally, advillin and villin both have a six-domain structure and headpiece domain (carboxyl-terminal). Along the full length, advillin exhibits substantial sequence

homology to villin. Murine villin and advillin share 65% identity at the nucleic acid level, with 75% homology and 59% identity in amino acid sequence. The headpiece of villin and advillin share 44% identity at the nucleic acid level, with 60% homology and 40% identity in amino acid sequence [61]. Of course, cross-reactivity of villin-antibodies with advillin do not allow to decide whether only one or even both structural proteins are coexpressed in an immunoreactive cell. Our data on gene expression strongly favor nearly exclusive advillin, but no villin expression in cholinergic chemosensory cells, in that *Vil1-Cre* activity was not detected in tracheal cholinergic chemosensory cells, and *in silico*-analysis of publicly available sequencing data sets also showed that less than 3% of cholinergic chemosensory cells were expressing *Vil1*-mRNA.

4.3 The ultrastructure of cholinergic chemosensory and neuroendocrine cells may reflect different functional requirements

In light microscopy, tracheal cholinergic chemosensory and neuroendocrine cells share some similarity in their morphology [25]. They are rare, flask-shaped epithelial cells, resting on the basement membrane. They have slender necks extending towards the lumen and short thick processes extending from their basal part. Some of them are connected to nerve fibers. They share two unique characteristics of spatial distribution: enrichment in epithelial areas between cartilages and a striking cranio-caudal gradient in cell frequency. However, our analysis showed that cholinergic chemosensory cells have slightly higher density recorded as cells per mm^2. Despite these similarities they are distinct cell types, they are different in their ultrastructure, and they have a different function. Recently, several studies have reported the role of these rare cells in immunoregulation. Tracheal cholinergic chemosensory cells are a predominant source of IL-25. Also, they express IL-25 receptor (IL17RB), IL-18, IL-10, CXCL12, and the enzymes involved in cysteinyl leukotriene synthesis. The production of these mediators by these cells suggests a role in airway immune responses [27]. Cholinergic chemosensory cells are sentinels of microbial products initiating protective neural reflexes and local innate immune responses [7–9]. Neuroendocrine cells, on the other hand, participate in immunoregulation by different mechanisms. In mouse models of allergic airway inflammation, GABA released from neuroepithelial bodies induces goblet cell hyperplasia and mucus overproduction. In addition, CGRP, another product of neuroendocrine cells, stimulates group 2 innate lymphoid cells to release IL-5, which in the end recruits eosinophils [19]. Immune cell recruitment in allergic airway inflammation is not restricted to eosinophils but includes also B cells and the formation of BALT [148]. The chemokine CXCL13 is indispensable for this process [47, 108–113, 168].

Our data add this homeostatic chemokine, CXCL13, to the portfolio of messengers produced by neuroendocrine cells, pointing towards a potential immunoregulatory function of these cells in BALT formation and B cell homeostasis.

Our results revealed a considerable difference in the ultrastructure of cholinergic chemosensory and neuroendocrine cells in transmission and scanning electron microscopy. In transmission electron microscopy, they are clearly distinguished by their luminal (apical) appearance. The cholinergic chemosensory cells have thinner, longer, and tightly packed microvilli compared to the neuroendocrine cells. In cholinergic chemosensory cells, filaments were observed extending from the root of the microvilli into the cytoplasm, which was not observed in neuroendocrine cells. These filaments have been previously described in the tuft cell of the intestine and, there, were considered as a passage carrying molecules and linking the endoplasmic reticulum to the intestinal lumen [169]. The differences in microvillus length and width were also evident in the scanning electron microscope, although the absolute values different from those measured by transmission electron microscope. This was most likely due to differences in sample preparation protocols. All these structural variations likely reflect different functional requirements. Furthermore, villin in neuroendocrine cells and advillin in cholinergic chemosensory cells might contribute to determining the apical features of these cells. For example, villin is expressed in microvilli of the epithelial cells of the intestine and the proximal tubules of the kidney [35–41] and most likely plays an important role in the morphogenesis of microvilli [170]. Advillin, however, is highly expressed in the dorsal root and trigeminal ganglia and all other neural crest-derived neurons [171]. Advillin can interact with the scavenger receptor SREC-1 (scavenger receptor expressed by endothelial cells-1) leading to morphological change in the cell and inducing neurite-like outgrowth [172].

Both cholinergic chemosensory and neuroendocrine cells have small size mitochondria compared to ciliated and secretory cells, though they were the smallest in neuroendocrine cells. These variations and the cell-type specific mitochondrial size could be a good differential criterion between different cell types in the airway epithelium, and it could be associated with cell-type specific function and demands.

The neuroendocrine cells additionally can be differentiated by the accumulation of dense core vesicles basally. Some vesicles were detected in cholinergic chemosensory cells, but they were less frequent, mostly located apically and larger than the neuroendocrine cell vesicles. The location of the vesicles in the basal or apical region may suggest that the contents of these vesicles will be secreted close to their location. For example, vesicles in the basal pole of the

cell might be secreted to affect the structures in their vicinity, which also can include the basolateral receptors of the other epithelial cells. Alternatively, vesicles located at the apical pole of the cell might be secreted into the lumen of the trachea affecting the surrounding epithelial cells by acting on receptors located at the apical surface. Additionally, the variation in the size of the vesicles might be caused by the different contents of these vesicles. For example, CGRP is a mediator which is known to be stored in vesicles [173]. Neuroendocrine cells release CGRP which stimulates group 2 innate lymphoid cells to release IL-5, which in the end recruits eosinophils [19]. This signaling mechanism and the fact that the dense core vesicles are preferentially located in the basal region of the cell suggest that the neuroendocrine cell most likely release CGRP from its basal side into the underlying tissues. On the other hand, the dense core vesicles in cholinergic chemosensory cells may contain mediators which can be released apically. Until now, the contents of such vesicles in cholinergic chemosensory cells remained unknown. Cholinergic chemosensory cells can release ACh [9], but in such non-neuronal cells, there is evidence to assume that it is released from the cytoplasm through certain transporters such as organic cation transporters (OCTs) [174] and choline transporter-like protein 4 (CTL4) [175].

The mono-modal frequency distribution of short and long axis diameters of dense core vesicles of the neuroendocrine cells (in total 930, vesicles were evaluated from 10 cells) indicates that tracheal neuroendocrine cells in the mouse have one population of dense core vesicles.

4.4 The predominant expression of CXCL13 in airway neuroendocrine cells suggests a putative role of these cells in B cell homeostasis

In this study, we identified a subtype of epithelial cells characterized by the expression of the chemokine CXCL13 in the naive mouse airway epithelium. By applying immunohistochemistry, *in-silico* analysis and immunoelectron techniques, we identified a subpopulation of neuroendocrine cells as a specific source of CXCL13 in the epithelium. We found that CXCL13 is predominantly expressed in solitary neuroendocrine cells of the tracheal epithelium and to a lesser extent in a small subpopulation of solitary and clustered broncho-pulmonary neuroendocrine cells of the lung.

Several studies have shown that CXCL13 plays a crucial role in BALT formation in several pathological conditions, including allergic airway inflammation [114], lung cancer [115, 116], bacterial [117–119]. and viral infection [120], cigarette smoking and chronic obstructive pulmonary disease (COPD) [121]. Within organized lymphoid tissues such as BALT, CXCL13

is predominantly produced by follicular dendritic cells [110, 168, 176]. Provided that BALT is located underneath the airway epithelium, one could assume that some signals from the epithelium might directly govern its formation. Several studies have shown that CXCL13 is not restricted to such follicular aggregates, and it is widely upregulated in the lung in inflammatory conditions. For example, CXCL13 expression can be induced in various airway epithelial cells, pneumocytes, macrophages, endothelial cells, and pulmonary reticular cells/fibroblasts [114, 117, 120, 177]. In contrast to neuroendocrine cells, however, there is no or only negligible steady state or homeostatic expression of CXCL13 in these cells. The expression of the homeostatic chemokine CXCL13 in neuroendocrine cells may point towards a putative role of these cells in the initial steps in B cell recruitment and B cell homeostasis before BALT has been formed, similar to its homeostatic role in B cell recruitment and B cell homeostasis of the secondary lymphoid organs [109, 110].

4.4.1 Potentially different secretory pathways of CXCL13 and CGRP

Neuroendocrine cells can produce different amines, neurotransmitters, and neuropeptides. Our data add a homeostatic chemokine, CXCL13, to the other products of neuroendocrine cells. As their name reflects, secretory products identified so far included biogenic amines like serotonin and GABA, which are typically used as neuronal signaling molecules, and peptides also known from neurons or endocrine cells like CGRP. A basal accumulation of dense core vesicles is the ultrastructural characteristic of airway neuroendocrine cells, and such amines and peptides are often co-stored in and co-released from such vesicles [178]. The limited overlap of CXCL13- and CGRP-immunoreactivities which we observed in high resolution confocal microscopy, however, might suggest an independent secretory pathway for CXCL13, matching their predicted mode of function. CGRP is a pre-formed mediator released by exocytosis of the storage vesicles upon acute stimulation, for example, exposure of human airway neuroendocrine cells to volatile chemicals [179]. Chemokines are preferentially released through constitutive secretory pathways [180, 181]. The specific secretory pathways of CXCL13 yet have not been investigated, but its homeostatic role in governing B cell migration through tissues is most compatible with a constitutive mode of secretion.

Pre-embedding immuno-electron microscopy validated the neuroendocrine identity of CXCL13-immunoreactive cells. Ultrastructurally, solitary neuroendocrine cells are characterized by basal aggregations of small granules with variable densities. Both CGRP- and CXCL13-immunoreactive cells invariably showed these accumulations of dense core vesicles. These dense core vesicles showed comparable dimensions in CGRP- and CXCL13-

immunoreactive cells, suggesting that the CXCL13-immunoreactive neuroendocrine cell phenotype is similar in ultrastructure to the other CGRP-immunoreactive neuroendocrine cells. This observation was consistent with our result about the mono-modal frequency distribution of diameters of dense core vesicles of the neuroendocrine cells, although the absolute values obtained from material processed for pre-embedding immuno-electron microscopy differed slightly from those obtained from routine electron microscopy. This is likely caused by the difference in sample preparation.

The pre-embedding immuno-electron microscopy based on a peroxidase reaction with DAB as a chromogen was chosen since it allows for osmication of the samples before embedding and ultrathin sectioning. This results in optimal preservation of the cell membrane and organelles, allowing for unequivocal identification of labeled cells and their general ultrastructure. Thus, the neuroendocrine identity of CXCL13-immunoreactive cells could be validated by detecting the dense core vesicles in the basal region of the cell. It should be emphasized, however, that this technique is not suited to determine the precise subcellular localization of CXCL13 and CGRP, since DAB is a diffusible reaction product that can precipitate microns away from the site of enzymatic generation.

4.4.2 Single RNA-sequence analysis suggests a phenotypic variation of CXCL13 expressing neuroendocrine cells

Double-labeling experiments with antibodies against two different neuroendocrine cell markers and *in silico*-analysis of available single cell RNA sequencing data very consistently revealed that approximately two thirds of tracheal neuroendocrine cells express CXCL13, whilst the remaining third is CXCL13-negative at a given time point. Notably, the raw single cell RNA sequencing data we analyzed were generated in an entirely independent laboratory at the Novartis Institutes for BioMedical Research, Cambridge, MA, USA [5]), showing that baseline expression of CXCL13 in tracheal neuroendocrine cells does not reflect an inflammatory condition that may have occurred unperceived in one animal house. Known inducers of CXCL13 expression in non-lymphoid tissue under inflammatory settings include type I interferon, IL-1, IL-17, IL-22 and tumor necrosis factor α [117, 182–184]. The driver of CXCL13 expression in tracheal neuroendocrine cells under baseline conditions remains to be discovered.

Even with this heterogeneity, however, unbiased scRNA-seq analysis of overall gene expression data did not yield subclusters of neuroendocrine cells, and expression of the most

characteristic and defining genes of neuroendocrine cells was not different between $CXCL13^+$ and $CXCL13^-$ cells. Thus, we consider $CXCL13^+$ and $CXCL13^-$ as phenotypes of one cell type rather than proposing to subdivide neuroendocrine cells into two distinct entities defined by the expression or not of CXCL13. However, this analysis includes only 53 neuroendocrine cells, and increasing the number of neuroendocrine cells might give additional information or defines a neuroendocrine subclusters.

Ptp4A3 (protein tyrosine phosphatase 4A3, *PRL-3* phosphatase of regenerating liver 3) was upregulated in *Cxcl13*$^+$ cells. *Ptp4A3* seemed to be strongly associated with the $CXCL13^+$ cell population (29/36 versus 3/17 in $CXCL13^-$ cells). Studies have shown an involvement of Ptp4A3 in chemokine and cytokine upregulation in human colon cancer tissues and cell lines [185, 186]. For example, when Ptp4A3 is overexpressed in colon cancer cell lines, Ptp4A3 has been found to regulate phosphorylation of proteins which are associated with many crucial signaling pathways, including focal adhesion, ErbB signaling pathway, MAPK signaling pathway and chemokine signaling pathway [185]. Ptp4A3 overexpressing in colon cancer cell lines is associated with upregulation and secretion of different cytokines like IL-1α and growth differentiation factors (GDF-15). Ptp4A3 upregulates and enhances the secretion of IL-1α via activating NF-κB and Jak2-Stat3 signal pathways [185]. Another study showed that Ptp4A3 upregulates chemokine (C-C motif) ligand 26 (CCL26) in colorectal cancer cells to induce tumor associated macrophages infiltration into tumor tissues [186]. Based on our scRNA-seq analysis and the finding of these studies, Ptp4A3 could also play a role in CXCL13 expression and secretion in tracheal neuroendocrine cells, however, this hypothesis needs to be investigated in the future.

4.5 Villin and CXCL13 expression in the lower airway suggests a spatial heterogeneity of the neuroendocrine cells

In contrast to the trachea, where neuroendocrine always appeared solitary or rarely as a couple of two neighboring cells, they predominantly clustered in the lung. The vast majority (95.3%) of broncho-pulmonary neuroendocrine cells were aggregated to neuroepithelial bodies and only 4.7% of cells were solitary neuroendocrine cells. In the trachea, two thirds of neuroendocrine cells were $CXCL13^+$, while CXCL13 expression occurred in only less than 10% of broncho-pulmonary neuroendocrine cells. During development, pulmonary neuroendocrine cells differentiate as solitary cells, presumably from basal cells, and then aggregate to neuroepithelial bodies through directed migration within the epithelial cell layer [85, 86]. It is unlikely that

downregulation of CXCL13 expression in neuroepithelial bodies was induced by this clustering because solitary neuroendocrine cells in the lung exhibited equally low frequency of CXCL13 expression as tracheal neuroendocrine cells. Thus, less broncho-pulmonary than tracheal neuroendocrine express CXCL13, regardless of whether they are aggregated into neuroepithelial bodies or lie solitarily in the epithelium. The difference also presents when we consider villin expression in the lung, where we could not detect villin at the protein level in the broncho-pulmonary neuroendocrine cells, neither in solitary cells nor in the neuroepithelial body, but it was detected in tracheal neuroendocrine cells. One possible cause of this difference might be that tracheal and broncho-pulmonary neuroendocrine cells represent two distinct entities with profound functional differences. Single cell sequencing data allowing direct comparison between tracheal and broncho-pulmonary neuroendocrine cells to address this question are not available yet. Alternatively, neuroendocrine cells of the tracheal and broncho-pulmonary epithelium basically represent the same cell type at different anatomical locations, but are exposed to different environmental cues driving CXCL13 and villin expression preferentially in the trachea. The particularly high frequency of neuroendocrine cells in the cranial (sublaryngeal) part of the trachea is suggestive of a sentinel function towards inhaled substances, in line with the observation of the expression of olfactory receptors in cultured human solitary tracheobronchial neuroendocrine cells [179]. Higher exposure to such air-borne stimuli might promote CXCL13 expression in the proximal airways. Yet, this model is not supported by our observation that the relative frequency of $CXCL13^+$ cells changed abruptly from trachea to lung but not gradually along the trachea. Lastly, the cellular microenvironment of tracheal and bronchopulmonary neuroendocrine cells differs, and tracheal neuroendocrine cells might be instructed to express CXCL13 by specific cells of their vicinity. One candidate might be cholinergic chemosensory cells which share two unique characteristics of spatial distribution with tracheal neuroendocrine cells: enrichment in epithelial areas between cartilages and a striking cranio-caudal gradient in cell frequency. In addition, the neuroendocrine cells were present in the lower airway from the proximal trachea into the distal bronchioles, while the cholinergic chemosensory cells were rarely found in the broncho-pulmonary epithelium below the tracheal bifurcation [7, 24], which may suggest less communication between cholinergic chemosensory and neuroendocrine cells in the broncho-pulmonary epithelium. Direct evidence of cross-talk between these rare cell types, however, has not been reported yet.

4.6 Tracheal neuroendocrine cell hyperplasia in *Pou2f3*–deficient mice suggests an unrecognized role of Pou2f3 in their population dynamics

The development of TRPM5-positive chemosensory cells is critically dependent on the transcription factor Pou2f3. Genetic deletion of *Pou2f3* results in the general absence of TRPM5-positive chemosensory cells, including the tracheal epithelium [32]. In our material, quantitative analysis of TRPM5-immunoreactive epithelial cells in tracheal whole mounts showed no difference between *Pou2f3*$^{+/-}$ and wild-type *Pou2f3*$^{+/+}$ mice, whereas in *Pou2f3*$^{-/-}$ mice, no TRPM5-immunoreactivity was detected as it was reported previously [32].

In oropharyngeal taste buds, the lack of TRPM5-positive type II taste cells is accompanied by increased numbers of type III taste cells in *Pou2f3*$^{-/-}$ mice [151–154]. Comparably, in the trachea, immunolabeling experiments with antibodies against two different neuroendocrine cell markers (PGP9.5 or CGRP) and CXCL13 (as another marker, we reported its exclusive expression in tracheal epithelium by neuroendocrine cells in this study) very consistently revealed neuroendocrine cell hyperplasia in *Pou2f3*$^{+/-}$ and *Pou2f3*$^{-/-}$. These data might suggest that the impact of Pou2f3 on tracheal epithelial development also extends beyond the block of the generation of TRPM5-positive cells. Notably, the loss of even only one allele of *Pou2f3* leads to hyperplasia of these cells, demonstrating an unrecognized role of this transcription factor in their population dynamics. One possible cause behind this expansion is that neuroendocrine and cholinergic chemosensory cells have the same progenitor and blocking the development of cholinergic chemosensory cells might drive the differentiation of progenitors to the neuroendocrine cell linage. Alternatively, tracheal neuroendocrine cell expansion might be an evidence of cross-talk between these rare cell types. For example, a signal from cholinergic chemosensory cells may affect neuroendocrine cell density. Acetylcholine signalling is one candidate of such a cross-talk. Previous work showed a significant increase in the neuroendocrine cells in the cervical part of trachea in mice lacking muscarinic acetylcholine receptor M1 (M1R$^{-/-}$) [166]. In that study, the increase in neuroendocrine cells occurred when the receptor was absent. It could be possible also the absence of ACh which is released by cholinergic chemosensory cells in *Pou2f3*$^{-/-}$ mice in our study caused this expansion. Alternatively, the absence of cholinergic chemosensory cells in *Pou2f3*$^{-/-}$ mice may affect the tracheal microenvironment which favors neuroendocrine cell expansion. On the other hand, this expansion may happen independent of cholinergic chemosensory cells. For example, recent work has identified hypoxia as a factor inducing the increase in the number of solitary neuroendocrine cells in the mouse trachea to protect adjacent epithelial cells from the damage

through releasing CGRP. In this model, basal cells differentiate into neuroendocrine cells, leading to neuroendocrine cell hyperplasia [187].

Type III taste cells (sour taste cells) share some characteristics and developmental aspects with neuroendocrine cells. They develop in the absence of Pou2f3; they share with neuroendocrine cells expression of AADC, SNAP-25, chromogranin A, chromogranin B, and they release serotonin and GABA [151, 157, 158]. *Ascl1/Mash1* (achaete-scute homolog 1/ mammalian achaete-scute homolog 1) encoding a basic helix-loop-helix transcription factor, is expressed in neuroendocrine cells [6] and plays an important role in their differentiation. Deficiency of the transcription factor *Ascl1* leads to absence of neuroendocrine cells in the mouse lung [188, 189]. Similarly, in the mouse adult taste buds, *Ascl1* is expressed in basal cells and most of type III cells, but not in type II cells [190]. *Ascl1* is required for the development of AADC- and glutamic acid decarboxylase 67- (GAD67) positive type III cells in the mouse taste buds [191, 192]. In this study, we found another common aspect between neuroendocrine cells and type III taste cells, in which neuroendocrine cells expand in *Pou2f3*-deficient mice like type III taste cells. Recent work showed a developmental relation between type II and type III taste cells, in which *Ascl1*-expressing precursor cells differentiate into type III cells and a small population of short lifetime type II cells (gustducin- and PLC-β2-positive cells) in the mouse mature taste buds [193]. This developmental aspect needs to be explored in trachea to study the relation between cholinergic chemosensory cells and neuroendocrine cells in trachea.

Double-labeling experiments with antibodies against CXCL13 and two different neuroendocrine cell markers consistently revealed that approximately two thirds of tracheal neuroendocrine cells express CXCL13, whilst a third is CXCL13-negative at a given time point in *Pou2f3*$^{+/+}$, *Pou2f3*$^{+/-}$ and *Pou2f3*$^{-/-}$ mice, consistent with our previous result in wild-type C57BL/6Rj mice.

Neuroendocrine cell hyperplasia is frequently observed in a variety of critical, but poorly understood lung diseases, including idiopathic diffuse hyperplasia of pulmonary neuroendocrine cells [194], sudden infant death syndrome [195, 196], bronchopulmonary dysplasia [197], and emphysema [198]. Therefore, it will be of great interest to identify the cause and the mechanism behind the solitary neuroendocrine cell expansion in *Pou2f3*$^{+/-}$ and *Pou2f3*$^{-/-}$ mice.

4.7 Conclusion

The present study identifies the enigmatic non-cholinergic chemosensory and villin-expressing cells in the lower airways as a cell population hidden amongst the neuroendocrine cells. Furthermore, the B cell attracting chemokine CXCL13 appeared as a novel mediator with high expression in a subpopulation of neuroendocrine cell, which includes villin-expressing neuroendocrine cells. Unbiased *in silico*-analysis of publicly available sequencing data sets in a limited number of cells supported our findings but did not yield subclusters of neuroendocrine cells. Thus, based on the available limited sequencing data resources, we can consider that villin and CXCL13 define phenotypes of one cell type rather than proposing to subdivide neuroendocrine cells into distinct entities defined by the expression or not of villin or CXCL13. Then, loss of even just one allele of Pou2f3 results in hyperplasia of neuroendocrine cell phenotypes, demonstrating a yet unrecognized role of this transcription factor in neuroendocrine cell population dynamics.

5. Summary

The rare epithelial cell types in the airways are ionocytes, solitary cholinergic chemosensory cells, solitary and clustered neuroendocrine cells. Previous studies reported an enigmatic rare cell in the mouse tracheal epithelium displaying an apical tuft of villin-immunoreactive microvilli. This cell has a morphology similar to cholinergic chemosensory cells. Unlike cholinergic chemosensory cells, the transcription factor Pou2f3 is not required for the development of these unknown cells. Furthermore, some scattered CXCL13 (B-cell attracting chemokine) -immunoreactive cells have been described in the airway epithelium under homeostatic condition, but their identity remained undefined. The present study aimed to clarify the identity of these ill-defined cell types and the role of the transcription factor Pou2f3 in regulation of their cell numbers.

To address these aims, appropriate mouse strains, either wild-type or genetically modified, were selected and studied by electron microscopy, immunohistochemistry and RT-PCR. In addition, *in silico*-analysis was done using publicly available sequencing data sets.

The present study identified the enigmatic non-cholinergic chemosensory and villin-expressing cells in the lower airways as a cell population hidden amongst the neuroendocrine cells. In contrast, villin is not expressed in tracheal cholinergic chemosensory cells. The B cell attracting chemokine CXCL13 appeared as a novel mediator with high expression in a subpopulation of neuroendocrine cells, including villin-expressing neuroendocrine cells. CXCL13 is expressed predominantly in solitary neuroendocrine cells of the tracheal epithelium (approx. 70% $CXCL13^+$) and, to a lesser extent, in the solitary neuroendocrine cells and neuroepithelial bodies of the intrapulmonary bronchial epithelium (<10% $CXCL13^+$). *In silico*-analysis of published sequencing data of murine tracheal epithelial cells was consistent with the results obtained by immunohistochemistry as it revealed that neuroendocrine cells are the major source of *Cxcl13*- and *Vil1*-mRNA. Unbiased *in silico*-analysis of publicly available sequencing data sets did not yield subclusters of neuroendocrine cells. Loss of even just one allele of Pou2f3 results in hyperplasia of neuroendocrine cell phenotypes.

The present data demonstrate phenotypic heterogeneity of airway neuroendocrine cells and point towards a putative regulatory role of these cells in B cell homeostasis. The transcription factor Pou2f3 plays a hitherto unrecognized role in their population dynamics.

6. Zusammenfassung

Zu den seltenen Epithelzelltypen der Atemwege werden Ionozyten, solitäre cholinerge chemosensorische Zellen sowie einzelne und gruppierte neuroendokrine Zellen gezählt. Zusätzlich wurde im Trachealepithel der Maus eine weitere Zelle mit einem apikalen Büschel villin-immunoreaktiver Mikrovilli beschrieben. Die Morphologie dieser Zellen ähnelt der der cholinergen chemosensorischen Zellen, jedoch ist im Gegensatz zu diesen der Transkriptionsfaktor Pou2f3 nicht für ihre Entwicklung notwendig. Weiterhin wurden im Atemwegsepithel verstreut CXCL13- (B-cell attracting chemokine) immunreaktive Zellen beschrieben, mit ebenfalls unbekannter Identität. Ziel dieser Arbeit war die Klärung der Identität dieser unbekannten Zellen und der Rolle des Transkriptionsfaktors Pou2f3 in der Regulation ihrer Zellzahl.

Zur Bearbeitung der Fragen wurden Elektronenmikroskopie, Immunhistochemie und RT-PCR an Proben von Mäusen mit für die Fragestellung relevanten genetischen Modifikationen angewandt. Zusätzlich wurden öffentlich zugängliche Sequenzierungsdatensätze *in silico* analysiert.

Diese Arbeit identifizierte die rätselhafte non-cholinerge chemosensorische und villin-exprimierende Zelle der unteren Atemwege als eine unter den neuroendokrinen Zellen versteckte Zellpopulation. Villin ist im Gegensatz dazu nicht in trachealen cholinergen chemosensorischen Zellen exprimiert. Das auf B Zellen chemotaktisch wirkende CXCL13 zeigte sich als ein neu erkannter Mediator einer Subpopulation von neuroendokrinen Zellen, darunter auch die villin-exprimierenden Zellen. CXCL13 ist vorwiegend in solitären neuroendokrinen Zellen der Trachea exprimiert (zu ca. 70%) und im geringeren Maße in den solitären neuroendokrinen Zellen und Neuroepithelkörperchen der intrapulmonalen Bronchien (<10%). *In silico*-Analyse der zugänglichen Sequenzdaten bestätigte, dass neuroendokrine Zellen die Hauptquelle von *Cxcl13*- und *Vil1*-mRNA sind, führte jedoch nicht zu einer Untergliederung der neuroendokrinen Zellen in klar getrennte Untergruppen. Verlust von auch nur einem Allel von *Pou2f3* resultierte in einer Hyperplasie der neuroendokrinen Zellphänotypen.

Die vorliegenden Daten zeigen eine phänotypische Heterogenität der neuroendokrinen Zellen der Atemwege und weisen auf eine regulatorische Rolle dieser Zellen in der B-Zell-Homöostase hin. Der Transkriptionsfaktor Pou2f3 spielt dabei eine bisher nicht erkannte Rolle in der Populationsdynamik der neuroendokrinen Zellen.

7. References

1 Meyerholz DK, Suarez CJ, Dintzis SM, Frevert CW: Respiratory System; in Comparative Anatomy and Histology, Elsevier, 2018, pp 147–162.

2 Rock JR, Randell SH, Hogan BLM: Airway basal stem cells: a perspective on their roles in epithelial homeostasis and remodeling. Disease Models & Mechanisms 2010;3:545–56.

3 Metzger RJ, Klein OD, Martin GR, Krasnow MA: The branching programme of mouse lung development. Nature 2008;453:745–50.

4 Hogan BLM, Barkauskas CE, Chapman HA, Epstein JA, Jain R, Hsia CCW, Niklason L, Calle E, Le A, Randell SH, Rock J, Snitow M, Krummel M, Stripp BR, Vu T, White ES, Whitsett JA, Morrisey EE: Repair and regeneration of the respiratory system: complexity, plasticity, and mechanisms of lung stem cell function. Cell Stem Cell 2014;15:123–38.

5 Plasschaert LW, Žilionis R, Choo-Wing R, Savova V, Knehr J, Roma G, Klein AM, Jaffe AB: A single-cell atlas of the airway epithelium reveals the CFTR-rich pulmonary ionocyte. Nature 2018;560:377–81.

6 Montoro DT, Haber AL, Biton M, Vinarsky V, Lin B, Birket SE, Yuan F, Chen S, Leung HM, Villoria J, Rogel N, Burgin G, Tsankov AM, Waghray A, Slyper M, Waldman J, Nguyen L, Dionne D, Rozenblatt-Rosen O, Tata PR, Mou H, Shivaraju M, Bihler H, Mense M, Tearney GJ, Rowe SM, Engelhardt JF, Regev A, Rajagopal J: A revised airway epithelial hierarchy includes CFTR-expressing ionocytes. Nature 2018;560:319–24.

7 Krasteva G, Canning BJ, Hartmann P, Veres TZ, Papadakis T, Mühlfeld C, Schliecker K, Tallini YN, Braun A, Hackstein H, Baal N, Weihe E, Schütz B, Kotlikoff M, Ibanez-Tallon I, Kummer W: Cholinergic chemosensory cells in the trachea regulate breathing. Proceedings of the National Academy of Sciences of the United States of America 2011;108:9478–83.

8 Krasteva G, Canning BJ, Papadakis T, Kummer W: Cholinergic brush cells in the trachea mediate respiratory responses to quorum sensing molecules. Life Sciences 2012;91:992–6.

9 Perniss A, Liu S, Boonen B, Keshavarz M, Ruppert A-L, Timm T, Pfeil U, Soultanova A, Kusumakshi S, Delventhal L, Aydin Ö, Pyrski M, Deckmann K, Hain T, Schmidt N, Ewers C, Günther A, Lochnit G, Chubanov V, Gudermann T, Oberwinkler J, Klein J, Mikoshiba K, Leinders-Zufall T, Offermanns S, Schütz B, Boehm U, Zufall F, Bufe B, Kummer W: Chemosensory cell-derived acetylcholine drives tracheal mucociliary clearance in response to virulence-associated formyl peptides. Immunity 2020;52:683-699.e11.

10 Reynolds SD, Giangreco A, Power JH, Stripp BR: Neuroepithelial bodies of pulmonary airways serve as a reservoir of progenitor cells capable of epithelial regeneration. The American Journal of Pathology 2000;156:269–78.

11 Song H, Yao E, Lin C, Gacayan R, Chen M-H, Chuang P-T: Functional characterization of pulmonary neuroendocrine cells in lung development, injury, and tumorigenesis. Proceedings of the National Academy of Sciences of the United States of America 2012;109:17531–6.

12 Ouadah Y, Rojas ER, Riordan DP, Capostagno S, Kuo CS, Krasnow MA: Rare pulmonary neuroendocrine cells are stem cells regulated by Rb, p53, and notch. Cell 2019;179:403-416.e23.

13 Lembrechts R, Brouns I, Schnorbusch K, Pintelon I, Kemp PJ, Timmermans J-P, Riccardi D, Adriaensen D: Functional expression of the multimodal extracellular calcium-sensing receptor in pulmonary neuroendocrine cells. Journal of Cell Science 2013;126:4490–501.

14 Fu XW, Wang D, Nurse CA, Dinauer MC, Cutz E: NADPH oxidase is an O2 sensor in airway chemoreceptors: evidence from K+ current modulation in wild-type and oxidase-deficient mice. Proceedings of the National Academy of Sciences of the United States of America 2000;97:4374–9.

15 Kazemian P, Stephenson R, Yeger H, Cutz E: Respiratory control in neonatal mice with NADPH oxidase deficiency. Respiration Physiology 2001;126:89–101.

16 Lembrechts R, Brouns I, Schnorbusch K, Pintelon I, Timmermans J-P, Adriaensen D: Neuroepithelial bodies as mechanotransducers in the intrapulmonary airway epithelium: involvement of TRPC5. American Journal of Respiratory Cell and Molecular Biology 2012;47:315–23.

17 Nonomura K, Woo S-H, Chang RB, Gillich A, Qiu Z, Francisco AG, Ranade SS, Liberles SD, Patapoutian A: Piezo2 senses airway stretch and mediates lung inflation-induced apnoea. Nature 2017;541:176–81.

18 Branchfield K, Nantie L, Verheyden JM, Sui P, Wienhold MD, Sun X: Pulmonary neuroendocrine cells function as airway sensors to control lung immune response. Science (New York, N.Y.) 2016;351:707–10.

19 Sui P, Wiesner DL, Xu J, Zhang Y, Lee J, van Dyken S, Lashua A, Yu C, Klein BS, Locksley RM, Deutsch G, Sun X: Pulmonary neuroendocrine cells amplify allergic asthma responses. Science (New York, N.Y.) 2018;360.

20 Hattori S, Matsuda M, Tateishi R, Nishihara H, Horai T: Oat-cell carcinoma of the lung. Clinical and morphological studies in relation to its histogenesis. Cancer 1972;30:1014–24.

21 Sutherland KD, Proost N, Brouns I, Adriaensen D, Song J-Y, Berns A: Cell of origin of small cell lung cancer: inactivation of Trp53 and Rb1 in distinct cell types of adult mouse lung. Cancer Cell 2011;19:754–64.

22 Park K-S, Liang M-C, Raiser DM, Zamponi R, Roach RR, Curtis SJ, Walton Z, Schaffer BE, Roake CM, Zmoos A-F, Kriegel C, Wong K-K, Sage J, Kim CF: Characterization of the cell of origin for small cell lung cancer. Cell Cycle 2011;10:2806–15.

23 Rhodin J, Dalhamn T: Electron microscopy of the tracheal ciliated mucosa in rat. Zeitschrift fur Zellforschung und Mikroskopische Anatomie 1956;44:345–412.

24 Tizzano M, Cristofoletti M, Sbarbati A, Finger TE: Expression of taste receptors in solitary chemosensory cells of rodent airways. BMC Pulmonary Medicine 2011;11:3.

25 Saunders CJ, Reynolds SD, Finger TE: Chemosensory brush cells of the trachea. A stable population in a dynamic epithelium. American Journal of Respiratory Cell and Molecular Biology 2013;49:190–6.

26 Krasteva-Christ G, Soultanova A, Schütz B, Papadakis T, Weiss C, Deckmann K, Chubanov V, Gudermann T, Voigt A, Meyerhof W, Boehm U, Weihe E, Kummer W: Identification of cholinergic chemosensory cells in mouse tracheal and laryngeal glandular ducts. International Immunopharmacology 2015;29:158–65.

27 Bankova LG, Dwyer DF, Yoshimoto E, Ualiyeva S, McGinty JW, Raff H, Moltke J von, Kanaoka Y, Frank Austen K, Barrett NA: The cysteinyl leukotriene 3 receptor regulates expansion of IL-25-producing airway brush cells leading to type 2 inflammation. Science Immunology 2018;3.

28 Zhao GQ, Zhang Y, Hoon MA, Chandrashekar J, Erlenbach I, Ryba NJ, Zuker CS: The Receptors for Mammalian Sweet and Umami Taste. Cell 2003;115:255–66.

29 Liu S, Lu S, Xu R, Atzberger A, Günther S, Wettschureck N, Offermanns S: Members of bitter taste receptor cluster Tas2r143/Tas2r135/Tas2r126 are expressed in the epithelium of murine airways and other non-gustatory tissues. Frontiers in Physiology 2017;8:849.

30 Kaske S, Krasteva G, König P, Kummer W, Hofmann T, Gudermann T, Chubanov V: TRPM5, a taste-signaling transient receptor potential ion-channel, is a ubiquitous signaling component in chemosensory cells. BMC Neuroscience 2007;8:49.

31 Perniss A, Schmidt P, Soultanova A, Papadakis T, Dahlke K, Voigt A, Schütz B, Kummer W, Deckmann K: Development of epithelial cholinergic chemosensory cells of the urethra and trachea of mice. Cell and Tissue Research 2021.

32 Yamashita J, Ohmoto M, Yamaguchi T, Matsumoto I, Hirota J: Skn-1a/Pou2f3 functions as a master regulator to generate Trpm5-expressing chemosensory cells in mice. PLOS One 2017;12:e0189340.

33 Bretscher A, Weber K: Villin: the major microfilament-associated protein of the intestinal microvillus. Proceedings of the National Academy of Sciences of the United States of America 1979;76:2321–5.

34 Bretscher A, Weber K: Villin is a major protein of the microvillus cystoskeleton which binds both G and F actin in a calcium-dependent manner. Cell 1980;20:839–47.

35 Bretscher A, Osborn M, Wehland J, Weber K: Villin associates with specific microfilamentous structures as seen by immunofluorescence microscopy on tissue sections and cells microinjected with villin. Experimental Cell Research 1981;135:213–9.

36 Robine S, Huet C, Moll R, Sahuquillo-Merino C, Coudrier E, Zweibaum A, Louvard D: Can villin be used to identify malignant and undifferentiated normal digestive epithelial cells? Proceedings of the National Academy of Sciences of the United States of America 1985;82:8488–92.

37 West A, Isaac CA, Carboni JM, Morrow JS, Mooseker MS, Barwick KW: Localization of villin, a cytoskeletal protein specific to microvilli, in human ileum and colon and in colonic neoplasms. Gastroenterology 1988;94:343–52.

38 Grone H-J, Weber K, Helmchen U, Osborn M: Villin -A Marker of Brush Border Differentiation and Cellular Origin in Human Renal Cell Carcinoma. American Journal of Pathology 1986;124:294–302.

39 Höfer D, Drenckhahn D: Identification of brush cells in the alimentary and respiratory system by antibodies to villin and fimbrin. Histochemistry 1992;98:237–42.

40 Höfer D, Drenckhahn D: Cytoskeletal markers allowing discrimination between brush cells and other epithelial cells of the gut including enteroendocrine cells. Histochemistry and Cell Biology 1996;105:405–12.

41 Brown D, Lee R, Bonventre JV: Redistribution of villin to proximal tubule basolateral membranes after ischemia and reperfusion. The American Journal of Physiology 1997;273:F1003-12.

42 Kerneis S, Bogdanova A, Colucci-Guyon E, Kraehenbuhl JP, Pringault E: Cytosolic distribution of villin in M cells from mouse Peyer's patches correlates with the absence of a brush border. Gastroenterology 1996;110:515–21.

43 Khurana S, George SP: Regulation of cell structure and function by actin-binding proteins: villin's perspective. FEBS Letters 2008;582:2128–39.

44 Southwick FS, DiNubile MJD: Rabbit alveolar macrophages contain a Ca2+-sensitive, 41,000-dalton protein which reversibly blocks the "barbed" ends of actin filaments but does not sever them. The Journal of Biological Chemistry 1986;261(30):14191-5.

45 Bazari WL, Matsudaira P, Wallek M, Smeal T, Jakes R, Ahmed Y: Villin sequence and peptide map identify six homologous domains. Proceedings of the National Academy of Sciences of the United States of America 1988;85:4986–90.

46 Pestonjamasp KN, Pope RK, Wulfkuhle JD, Luna EJ: Supervillin (p205): A novel membrane-associated, F-actin-binding protein in the villin/gelsolin superfamily. The Journal of Cell Biology 1997;139:1255–69.

47 Campbell JJ, Hedrick J, Zlotnik A, Siani MA, Thompson DA, Butcher EC: Chemokines and the arrest of lymphocytes rolling under flow conditions. Science (New York, N.Y.) 1998;279:381–4.

48 Janmey PA, Matsudaira PT: Functional comparison of villin and gelsolin. Effects of Ca2+, KCl, and polyphosphoinositides. The Journal of Biological Chemistry 1988;263(32):16738-43.

49 Glenney JR, Weber K: Calcium control of microfilaments: uncoupling of the F-actin-severing and -bundling activity of villin by limited proteolysis in vitro. Proceedings of the National Academy of Sciences of the United States of America 1981;78:2810–4.

50 Glenney Jr. JR, Kaulfus P, Weber K: F actin assembly modulated by villin: Ca++-dependent nucleation and capping of the barbed end. Cell 1981;24:471–80.

51 Glenney JR, Geisler N, Kaulfus P, Weber K: Demonstration of at least two different actin-binding sites in villin, a calcium-regulated modulator of F-actin organization. Journal of Biological Chemistry 1981;256:8156–61.

52 Pinson KI, Dunbar L, Samuelson L, Gumucio DL: Targeted disruption of the mouse villin gene does not impair the morphogenesis of microvilli. Developmental Dynamics 1998;211:109–21.

53 Ferrary E, Cohen-Tannoudji M, Pehau-Arnaudet G, Lapillonne A, Athman R, Ruiz T, Boulouha L, El Marjou F, Doye A, Fontaine JJ, Antony C, Babinet C, Louvard D, Jaisser F, Robine S: In vivo, villin is required for Ca(2+)-dependent F-actin disruption in intestinal brush borders. The Journal of Cell Biology 1999;146:819–30.

54 Northrop J, Weber A, Mooseker MS, Franzini-Armstrong C, Bishop MF, Dubyak GR, Tucker M, Walsh TP: Different calcium dependence of the capping and cutting activities of villin. Journal of Biological Chemistry 1986;261:9274–81.

55 Zhai L, Zhao P, Panebra A, Guerrerio AL, Khurana S: Tyrosine phosphorylation of villin regulates the organization of the actin cytoskeleton. The Journal of Biological Chemistry 2001;276:36163–7.

56 Burgess DR, Broschat KO, Hayden JM: Tropomyosin distinguishes between the two actin-binding sites of villin and affects actin-binding properties of other brush border proteins. The Journal of Cell Biology 1987;104:29–40.

57 Kumar N, Zhao P, Tomar A, Galea CA, Khurana S: Association of villin with phosphatidylinositol 4,5-bisphosphate regulates the actin cytoskeleton. The Journal of Biological Chemistry 2004;279:3096–110.

58 Wang Y, Srinivasan K, Siddiqui MR, George SP, Tomar A, Khurana S: A novel role for villin in intestinal epithelial cell survival and homeostasis. The Journal of Biological Chemistry 2008;283:9454–64.

59 Tomar A, Wang Y, Kumar N, George S, Ceacareanu B, Hassid A, Chapman KE, Aryal AM, Waters CM, Khurana S: Regulation of cell motility by tyrosine phosphorylated villin. Molecular Biology of the Cell 2004;15:4807–17.

60 Wang Y, Tomar A, George SP, Khurana S: Obligatory role for phospholipase C-gamma(1) in villin-induced epithelial cell migration. American Journal of Physiology. Cell Physiology 2007;292:C1775-86.

61 Marks PW, Arai M, Bandura JL, Kwiatkowski DJ: Advillin (p92): a new member of the gelsolin/villin family of actin regulatory proteins. Journal of Cell Science 1998;111:2129–36.

62 Esmaeilniakooshkghazi A, George SP, Biswas R, Khurana S: Mouse intestinal tuft cells express advillin but not villin. Scientific Reports 2020;10:8877.

63 Krasteva G, Hartmann P, Papadakis T, Bodenbenner M, Wessels L, Weihe E, Schütz B, Langheinrich AC, Chubanov V, Gudermann T, Ibanez-Tallon I, Kummer W: Cholinergic chemosensory cells in the auditory tube. Histochemistry and Cell Biology 2012;137:483–97.

64 Panneck AR, Rafiq A, Schütz B, Soultanova A, Deckmann K, Chubanov V, Gudermann T, Weihe E, Krasteva-Christ G, Grau V, Del Rey A, Kummer W: Cholinergic epithelial cell with chemosensory traits in murine thymic medulla. Cell and Tissue Research 2014;358:737–48.

65 Deckmann K, Filipski K, Krasteva-Christ G, Fronius M, Althaus M, Rafiq A, Papadakis T, Renno L, Jurastow I, Wessels L, Wolff M, Schütz B, Weihe E, Chubanov V, Gudermann T, Klein J, Bschleipfer T, Kummer W: Bitter triggers acetylcholine release from polymodal

urethral chemosensory cells and bladder reflexes. Proceedings of the National Academy of Sciences of the United States of America 2014;111:8287–92.

66 Horvat B, Osborn M, Damjanov I: Expression of villin in the mouse oviduct and the seminiferous ducts. Histochemistry 1990;93:661–3.

67 Saqui-Salces M, Keeley TM, Grosse AS, Qiao XT, El-Zaatari M, Gumucio DL, Samuelson LC, Merchant JL: Gastric tuft cells express DCLK1 and are expanded in hyperplasia. Histochemistry and Cell Biology 2011;136:191–204.

68 Schütz B, Ruppert A-L, Strobel O, Lazarus M, Urade Y, Büchler MW, Weihe E: Distribution pattern and molecular signature of cholinergic tuft cells in human gastro-intestinal and pancreatic-biliary tract. Scientific Reports 2019;9:17466.

69 Bezençon C, Fürholz A, Raymond F, Mansourian R, Métairon S, Le Coutre J, Damak S: Murine intestinal cells expressing Trpm5 are mostly brush cells and express markers of neuronal and inflammatory cells. The Journal of Comparative Neurology 2008;509:514–25.

70 Bornstein C, Nevo S, Giladi A, Kadouri N, Pouzolles M, Gerbe F, David E, Machado A, Chuprin A, Tóth B, Goldberg O, Itzkovitz S, Taylor N, Jay P, Zimmermann VS, Abramson J, Amit I: Single-cell mapping of the thymic stroma identifies IL-25-producing tuft epithelial cells. Nature 2018;559:622–6.

71 Ruppert A-L, Keshavarz M, Winterberg S, Oberwinkler J, Kummer W, Schütz B: Advillin is a tuft cell marker in the mouse alimentary tract. Journal of Molecular Histology 2020;51:421–35.

72 van Lommel A, Bollé T, Fannes W, Lauweryns JM: The pulmonary neuroendocrine system: the past decade. Archives of Histology and Cytology 1999;62:1–16.

73 Cutz E, Pan J, Yeger H, Domnik NJ, Fisher JT: Recent advances and contraversies on the role of pulmonary neuroepithelial bodies as airway sensors. Seminars in Cell & Developmental Biology 2013;24:40–50.

74 Lauweryns JM, Cokelaere M, Theunynck P: Neuro-epithelial bodies in the respiratory mucosa of various mammals. A light Optical, Histochemical and Ultrastructural Investigation. Zeitschrift fur Zellforschung und Mikroskopische Anatomie 1972;135:569–92.

75 Hung K-S, Hertweck MS, Hardy JD, Loosli CG: Ultrastructure of nerves and associated cells in bronchiolar epithelium of the mouse lung. Journal of Ultrastructure Research 1973;43:426–37.

76 Wasano K: Neuro-epithelial bodies in the lung of the rat and the mouse. Archivum histologicum Japonicum = Nihon soshikigaku kiroku 1977;40 Suppl:207–19.

77 Frohlich F: The light cell of the bronchial mucosa and its relationship to the problem of chemoreceptors. Frankfurter Zeitschrift für Pathologie 1949;60:517–59.

78 Bonikos DS, Bensch KG: Endocrine cells of bronchial and bronchiolar epithelium. The American Journal of Medicine 1977;63:765–71.

79 Pearse AG: The cytochemistry and ultrastructure of polypeptide hormone-producing cells of the APUD series and the embryologic, physiologic and pathologic implications of the concept. The journal of histochemistry and cytochemistry official journal of the Histochemistry Society 1969;17:303–13.

80 Lauweryns JM, Peuskens JC: Neuro-epithelial bodies (neuroreceptor or secretory organs?) in human infant bronchial and bronchiolar epithelium. The Anatomical record 1972;172:471–81.

81 Ericson LE, Håkanson R, Larson B, Owman C, Sundler F: Fluorescence and electron microscopy of amine-storing enterochromaffin-like cells in tracheal epithelium of mouse. Zeitschrift fur Zellforschung und mikroskopische Anatomie (Vienna, Austria 1948) 1972;124:532–45.

82 Hung KS, Loosli CG: Bronchiolar neuro-epithelial bodies in the neonatal mouse lungs. The American journal of anatomy 1974;140:191–9.

83 Perl A-KT, Wert SE, Nagy A, Lobe CG, Whitsett JA: Early restriction of peripheral and proximal cell lineages during formation of the lung. Proceedings of the National Academy of Sciences of the United States of America 2002;99:10482–7.

84 Rawlins EL, Clark CP, Xue Y, Hogan BLM: The Id2+ distal tip lung epithelium contains individual multipotent embryonic progenitor cells. Development (Cambridge, England) 2009;136:3741–5.

85 Noguchi M, Sumiyama K, Morimoto M: Directed migration of pulmonary neuroendocrine cells toward airway branches organizes the stereotypic location of neuroepithelial bodies. Cell Reports 2015;13:2679–86.

86 Kuo CS, Krasnow MA: Formation of a neurosensory organ by epithelial cell slithering. Cell 2015;163:394–405.

87 Lauweryns JM, van Lommel AT, Dom RJ: Innervation of rabbit intrapulmonary neuroepithelial bodies. Journal of the Neurological Sciences 1985;67:81–92.

88 Pan J, Yeger H, Cutz E: Innervation of pulmonary neuroendocrine cells and neuroepithelial bodies in developing rabbit lung. The Journal of Histochemistry and Cytochemistry Official Journal of the Histochemistry Society 2004;52:379–89.

89 Weichselbaum M, Sparrow MP, Hamilton EJ, Thompson PJ, Knight DA: A confocal microscopic study of solitary pulmonary neuroendocrine cells in human airway epithelium. Respiratory Research 2005;6:115.

90 Brouns I, Oztay F, Pintelon I, Proost I de, Lembrechts R, Timmermans J-P, Adriaensen D: Neurochemical pattern of the complex innervation of neuroepithelial bodies in mouse lungs. Histochemistry and Cell Biology 2009;131:55–74.

91 Rawlins EL, Okubo T, Xue Y, Brass DM, Auten RL, Hasegawa H, Wang F, Hogan BLM: The role of Scgb1a1+ Clara cells in the long-term maintenance and repair of lung airway, but not alveolar, epithelium. Cell Stem Cell 2009;4:525–34.

92 Adriaensen D, Brouns I, Pintelon I, Proost I de, Timmermans J-P: Evidence for a role of neuroepithelial bodies as complex airway sensors: comparison with smooth muscle-associated airway receptors. Journal of Applied Physiology 2006;101:960–70.

93 Miller MC, Mayo KH: Chemokines from a structural perspective. International Journal of Molecular Sciences 2017;18.

94 Legler DF, Thelen M: Chemokines: Chemistry, Biochemistry and Biological Function. Chimia 2016;70:856–9.

95 Bachelerie F, Ben-Baruch A, Burkhardt AM, Combadiere C, Farber JM, Graham GJ, Horuk R, Sparre-Ulrich AH, Locati M, Luster AD, Mantovani A, Matsushima K, Murphy PM, Nibbs R, Nomiyama H, Power CA, Proudfoot AEI, Rosenkilde MM, Rot A, Sozzani S, Thelen M, Yoshie O, Zlotnik A: International Union of Basic and Clinical Pharmacology. corrected. LXXXIX. Update on the extended family of chemokine receptors and introducing a new nomenclature for atypical chemokine receptors. Pharmacological Reviews 2014;66:1–79.

96 Mackay CR: Chemokines: immunology's high impact factors. Nature Immunology 2001;2:95–101.

97 de Yang, Chen Q, Hoover DM, Staley P, Tucker KD, Lubkowski J, Oppenheim JJ: Many chemokines including CCL20/MIP-3alpha display antimicrobial activity. Journal of Leukocyte Biology 2003;74:448–55.

98 Crawford M, Burdick MD, Glomski IJ, Boyer AE, Barr JR, Mehrad B, Strieter RM, Hughes M: Interferon-inducible CXC chemokines directly contribute to host defense against inhalational anthrax in a murine model of infection. PLOS Pathogens 2010;6.

99 Addison CL, Daniel TO, Burdick MD, Liu H, Ehlert JE, Xue YY, Buechi L, Walz A, Richmond A, Strieter RM: The CXC chemokine receptor 2, CXCR2, is the putative receptor for ELR+ CXC chemokine-induced angiogenic activity. Journal of Immunology 2000;165:5269–77.

100 Endres R, Alimzhanov MB, Plitz T, Fütterer A, Kosco-Vilbois MH, Nedospasov SA, Rajewsky K, Pfeffer K: Mature follicular dendritic cell networks depend on expression of lymphotoxin beta receptor by radioresistant stromal cells and of lymphotoxin beta and tumor necrosis factor by B cells. The Journal of Experimental Medicine 1999;189:159–68.

101 Gerszten RE, Garcia-Zepeda EA, Lim YC, Yoshida M, Ding HA, Gimbrone MA, Luster AD, Luscinskas FW, Rosenzweig A: MCP-1 and IL-8 trigger firm adhesion of monocytes to vascular endothelium under flow conditions. Nature 1999;398:718–23.

102 Fernandez EJ, Lolis E: Structure, function, and inhibition of chemokines. Annual Review of Pharmacology and Toxicology 2002;42:469–99.

103 Zlotnik A, Yoshie O: The chemokine superfamily revisited. Immunity 2012;36:705–16.

104 Chen K, Bao Z, Tang P, Gong W, Yoshimura T, Wang JM: Chemokines in homeostasis and diseases. Cellular & Molecular Immunology 2018;15:324–34.

105 Rossi D, Zlotnik A: The biology of chemokines and their receptors. Annual Review of Immunology 2000;18:217–42.

106 Dobner T, Wolf I, Emrich T, Lipp M: Differentiation-specific expression of a novel G protein-coupled receptor from Burkitt's lymphoma. European Journal of Immunology 1992;22:2795–9.

107 Kaiser E, Förster R, Wolf I, Ebensperger C, Kuehl WM, Lipp M: The G protein-coupled receptor BLR1 is involved in murine B cell differentiation and is also expressed in neuronal tissues. European Journal of Immunology 1993;23:2532–9.

108 Förster R, Mattis AE, Kremmer E, Wolf E, Brem G, Lipp M: A Putative chemokine receptor, BLR1, directs B cell migration to defined lymphoid organs and specific anatomic compartments of the spleen. Cell 1996;87:1037–47.

109 Legler DF, Loetscher M, Roos RS, Clark-Lewis I, Baggiolini M, Moser B: B cell-attracting chemokine 1, a human CXC chemokine expressed in lymphoid tissues, selectively attracts B lymphocytes via BLR1/CXCR5. The Journal of Experimental Medicine 1998;187:655–60.

110 Gunn MD, Ngo VN, Ansel KM, Ekland EH, Cyster JG, Williams LT: A B-cell-homing chemokine made in lymphoid follicles activates Burkitt's lymphoma receptor-1. Nature 1998;391:799–803.

111 Förster R, Emrich T, Kremmer E, Lipp M.: Expression of the G-protein-coupled receptor BLR1 defines mature, recirculating B cells and a subset of T-helper memory cells. Blood 1994;84:830–40.

112 Vissers JLM, Hartgers FC, Lindhout E, Figdor CG, Adema GJ: BLC (CXCL13) is expressed by different dendritic cell subsets in vitro and in vivo. European Journal of Immunology. 2001;31:1544–9.

113 Cyster JG, Ansel KM, Reif K, Ekland EH, Hyman PL, Tang HL, Luther SA, Ngo VN: Follicular stromal cells and lymphocyte homing to follicles. Immunological Reviews 2000;176:181–93.

114 Baay-Guzman GJ, Huerta-Yepez S, Vega MI, Aguilar-Leon D, Campillos M, Blake J, Benes V, Hernandez-Pando R, Teran LM: Role of CXCL13 in asthma: novel therapeutic target. Chest 2012;141:886–94.

115 Rangel-Moreno J, Hartson L, Navarro C, Gaxiola M, Selman M, Randall TD: Inducible bronchus-associated lymphoid tissue (iBALT) in patients with pulmonary complications of rheumatoid arthritis. The Journal of Clinical Investigation 2006;116:3183–94.

116 Dieu-Nosjean M-C, Antoine M, Danel C, Heudes D, Wislez M, Poulot V, Rabbe N, Laurans L, Tartour E, Chaisemartin L de, Lebecque S, Fridman W-H, Cadranel J: Long-term survival for patients with non-small-cell lung cancer with intratumoral lymphoid structures. Journal of Clinical Oncology Official Journal of the American Society of Clinical Oncology 2008;26:4410–7.

117 Frija-Masson J, Martin C, Regard L, Lothe M-N, Touqui L, Durand A, Lucas B, Damotte D, Alifano M, Fajac I, Burgel P-R: Bacteria-driven peribronchial lymphoid neogenesis in bronchiectasis and cystic fibrosis. The European Respiratory Journal 2017;49.

118 Khader SA, Rangel-Moreno J, Fountain JJ, Martino CA, Reiley WW, Pearl JE, Winslow GM, Woodland DL, Randall TD, Cooper AM: In a murine tuberculosis model, the absence of homeostatic chemokines delays granuloma formation and protective immunity. Journal of Immunology 2009;183:8004–14.

119 Day TA, Koch M, Nouailles G, Jacobsen M, Kosmiadi GA, Miekley D, Kuhlmann S, Jörg S, Gamradt P, Mollenkopf H-J, Hurwitz R, Reece ST, Kaufmann SHE, Kursar M: Secondary lymphoid organs are dispensable for the development of T-cell-mediated immunity during tuberculosis. European Journal of Immunology 2010;40:1663–73.

120 Denton AE, Innocentin S, Carr EJ, Bradford BM, Lafouresse F, Mabbott NA, Mörbe U, Ludewig B, Groom JR, Good-Jacobson KL, Linterman MA: Type I interferon induces

CXCL13 to support ectopic germinal center formation. The Journal of Experimental Medicine 2019;216:621–37.

121 Bracke KR, Verhamme FM, Seys LJM, Bantsimba-Malanda C, Cunoosamy DM, Herbst R, Hammad H, Lambrecht BN, Joos GF, Brusselle GG: Role of CXCL13 in cigarette smoke-induced lymphoid follicle formation and chronic obstructive pulmonary disease. American Journal of Respiratory and Critical Care Medicine 2013;188:343–55.

122 Moyron-Quiroz JE, Rangel-Moreno J, Kusser K, Hartson L, Sprague F, Goodrich S, Woodland DL, Lund FE, Randall TD: Role of inducible bronchus associated lymphoid tissue (iBALT) in respiratory immunity. Nature Medicine 2004;10:927–34.

123 Randall TD: Bronchus-associated lymphoid tissue (BALT) structure and function. Advances in Immunology 2010;107:187–241.

124 Hwang JY, Randall TD, Silva-Sanchez A: Inducible Bronchus-Associated Lymphoid Tissue: Taming Inflammation in the Lung. Frontiers in Immunology 2016;7:258.

125 Gould SJ, Isaacson PG: Bronchus-associated lymphoid tissue (BALT) in human fetal and infant lung. The Journal of Pathology 1993;169:229–34.

126 Pabst R, Gehrke I: Is the bronchus-associated lymphoid tissue (BALT) an integral structure of the lung in normal mammals, including humans? American Journal of Respiratory Cell and Molecular Biology 1990;3:131–5.

127 Woodland DL, Randall TD: Anatomical features of anti-viral immunity in the respiratory tract. Seminars in Immunology 2004;16:163–70.

128 Kocks JR, Davalos-Misslitz ACM, Hintzen G, Ohl L, Förster R: Regulatory T cells interfere with the development of bronchus-associated lymphoid tissue. The Journal of Experimental Medicine 2007;204:723–34.

129 GeurtsvanKessel CH, Willart MAM, Bergen IM, van Rijt LS, Muskens F, Elewaut D, Osterhaus ADME, Hendriks R, Rimmelzwaan GF, Lambrecht BN: Dendritic cells are crucial for maintenance of tertiary lymphoid structures in the lung of influenza virus-infected mice. The Journal of Experimental Medicine 2009;206:2339–49.

130 Ansel KM, Ngo VN, Hyman PL, Luther SA, Förster R, Sedgwick JD, Browning JL, Lipp M, Cyster JG: A chemokine-driven positive feedback loop organizes lymphoid follicles. Nature 2000;406:309–14.

131 Rangel-Moreno J, Moyron-Quiroz JE, Hartson L, Kusser K, Randall TD: Pulmonary expression of CXC chemokine ligand 13, CC chemokine ligand 19, and CC chemokine ligand 21 is essential for local immunity to influenza. Proceedings of the National Academy of Sciences of the United States of America 2007;104:10577–82.

132 Matsumoto M, Fu YX, Molina H, Chaplin DD: Lymphotoxin-alpha-deficient and TNF receptor-I-deficient mice define developmental and functional characteristics of germinal centers. Immunological Reviews 1997;156:137–44.

133 Fütterer A, Mink K, Luz A, Kosco-Vilbois MH, Pfeffer K: The lymphotoxin β receptor controls organogenesis and affinity maturation in peripheral lymphoid tissues. Immunity 1998;9:59–70.

134 Gonzalez M, Mackay F, Browning JL, Kosco-Vilbois MH, Noelle RJ: The sequential role of lymphotoxin and B cells in the development of splenic follicles. The Journal of Experimental Medicine 1998;187:997–1007.

135 Halle S, Dujardin HC, Bakocevic N, Fleige H, Danzer H, Willenzon S, Suezer Y, Hämmerling G, Garbi N, Sutter G, Worbs T, Förster R: Induced bronchus-associated lymphoid tissue serves as a general priming site for T cells and is maintained by dendritic cells. The Journal of Experimental Medicine 2009;206:2593–601.

136 Hiramatsu K, Azuma A, Kudoh S, Desaki M, Takizawa H, Sugawara I: Inhalation of diesel exhaust for three months affects major cytokine expression and induces bronchus-associated lymphoid tissue formation in murine lungs. Experimental Lung Research 2003;29:607–22.

137 Förster R, Schubel A, Breitfeld D, Kremmer E, Renner-Müller I, Wolf E, Lipp M: CCR7 coordinates the primary immune response by establishing functional microenvironments in secondary lymphoid organs. Cell 1999;99:23–33.

138 Mebius RE: Organogenesis of lymphoid tissues. Nature Reviews. Immunology 2003;3:292–303.

139 Randall TD, Carragher DM, Rangel-Moreno J: Development of secondary lymphoid organs. Annual Review of Immunology 2008;26:627–50.

140 Ngo VN, Korner H, Gunn MD, Schmidt KN, Riminton DS, Cooper MD, Browning JL, Sedgwick JD, Cyster JG: Lymphotoxin alpha/beta and tumor necrosis factor are required for stromal cell expression of homing chemokines in B and T cell areas of the spleen. The Journal of Experimental Medicine 1999;189:403–12.

141 Conlon TM, John-Schuster G, Heide D, Pfister D, Lehmann M, Hu Y, Ertüz Z, Lopez MA, Ansari M, Strunz M, Mayr C, Angelidis I, Ciminieri C, Costa R, Kohlhepp MS, Guillot A, Günes G, Jeridi A, Funk MC, Beroshvili G, Prokosch S, Hetzer J, Verleden SE, Alsafadi H, Lindner M, Burgstaller G, Becker L, Irmler M, Dudek M, Janzen J, Goffin E, Gosens R, Knolle P, Pirotte B, Stoeger T, Beckers J, Wagner D, Singh I, Theis FJ, Angelis MH de, O'Connor T, Tacke F, Boutros M, Dejardin E, Eickelberg O, Schiller HB, Königshoff M,

Heikenwalder M, Yildirim AÖ: Inhibition of LTβR signalling activates WNT-induced regeneration in lung. Nature 2020;588:151–6.

142 Demoor T, Bracke KR, Maes T, Vandooren B, Elewaut D, Pilette C, Joos GF, Brusselle GG: Role of lymphotoxin-alpha in cigarette smoke-induced inflammation and lymphoid neogenesis. The European Respiratory Journal 2009;34:405–16.

143 Rangel-Moreno J, Carragher DM, La Luz Garcia-Hernandez M de, Hwang JY, Kusser K, Hartson L, Kolls JK, Khader SA, Randall TD: The development of inducible bronchus-associated lymphoid tissue depends on IL-17. Nature Immunology 2011;12:639–46.

144 Lund FE, Partida-Sánchez S, Lee BO, Kusser KL, Hartson L, Hogan RJ, Woodland DL, Randall TD: Lymphotoxin-alpha-deficient mice make delayed, but effective, T and B cell responses to influenza. Journal of Immunology 2002;169:5236–43.

145 Chen HD, Fraire AE, Joris I, Welsh RM, Selin LK: Specific history of heterologous virus infections determines anti-viral immunity and immunopathology in the lung. The American Journal of Pathology 2003;163:1341–55.

146 Wiley JA, Richert LE, Swain SD, Harmsen A, Barnard DL, Randall TD, Jutila M, Douglas T, Broomell C, Young M, Harmsen A: Inducible bronchus-associated lymphoid tissue elicited by a protein cage nanoparticle enhances protection in mice against diverse respiratory viruses. PlOS One 2009;4:e7142.

147 Moyron-Quiroz JE, Rangel-Moreno J, Hartson L, Kusser K, Tighe MP, Klonowski KD, Lefrançois L, Cauley LS, Harmsen AG, Lund FE, Randall TD: Persistence and responsiveness of immunologic memory in the absence of secondary lymphoid organs. Immunity 2006;25:643–54.

148 Chvatchko Y, Kosco-Vilbois MH, Herren S, Lefort J, Bonnefoy JY: Germinal center formation and local immunoglobulin E (IgE) production in the lung after an airway antigenic challenge. The Journal of Experimental Medicine 1996;184:2353–60.

149 Andersen B, Schonemann MD, Flynn SE, Pearse RV, Singh H, Rosenfeld MG: Skn-1a and Skn-1i: two functionally distinct Oct-2-related factors expressed in epidermis. Science (New York, N.Y.) 1993;260:78–82.

150 Andersen B, Weinberg WC, Rennekampff O, McEvilly RJ, Bermingham JR, Hooshmand F, Vasilyev V, Hansbrough JF, Pittelkow MR, Yuspa SH, Rosenfeld MG: Functions of the POU domain genes Skn-1a/i and Tst-1/Oct-6/SCIP in epidermal differentiation. Genes & Development 1997;11:1873–84.

151 Matsumoto I, Ohmoto M, Narukawa M, Yoshihara Y, Abe K: Skn-1a (Pou2f3) specifies taste receptor cell lineage. Nature Neuroscience 2011;14:685–7.

152 Maeda N, Narukawa M, Ishimaru Y, Yamamoto K, Misaka T, Abe K: A large increase of sour taste receptor cells in Skn-1-deficient mice does not alter the number of their sour taste signal-transmitting gustatory neurons. Neuroscience Letters 2017;648:53–8.

153 Larson ED, Vandenbeuch A, Anderson CB, Kinnamon SC: Function, innervation, and neurotransmitter signaling in mice lacking type-II taste cells. eNeuro 2020;7.

154 Ohmoto M, Jyotaki M, Foskett JK, Matsumoto I: Sodium-taste cells require Skn-1a for generation and share molecular features with sweet, umami, and bitter taste cells. eNeuro 2020;7.

155 Huang Y-H, Klingbeil O, He X-Y, Wu XS, Arun G, Lu B, Somerville TDD, Milazzo JP, Wilkinson JE, Demerdash OE, Spector DL, Egeblad M, Shi J, Vakoc CR: POU2F3 is a master regulator of a tuft cell-like variant of small cell lung cancer. Genes & Development 2018;32:915–28.

156 Ireland AS, Micinski AM, Kastner DW, Guo B, Wait SJ, Spainhower KB, Conley CC, Chen OS, Guthrie MR, Soltero D, Qiao Y, Huang X, Tarapcsák S, Devarakonda S, Chalishazar MD, Gertz J, Moser JC, Marth G, Puri S, Witt BL, Spike BT, Oliver TG: MYC drives temporal evolution of small cell lung cancer subtypes by reprogramming neuroendocrine fate. Cancer Cell 2020;38:60-78.e12.

157 Sukumaran SK, Lewandowski BC, Qin Y, Kotha R, Bachmanov AA, Margolskee RF: Whole transcriptome profiling of taste bud cells. Scientific Reports 2017;7:7595.

158 Huang YA, Pereira E, Roper SD: Acid stimulation (sour taste) elicits GABA and serotonin release from mouse taste cells. PLOS One 2011;6:e25471.

159 Muzumdar MD, Tasic B, Miyamichi K, Li L, Luo L: A global double-fluorescent Cre reporter mouse. Genesis (New York, N.Y. 2000) 2007;45:593–605.

160 Madison BB, Dunbar L, Qiao XT, Braunstein K, Braunstein E, Gumucio DL: Cis elements of the villin gene control expression in restricted domains of the vertical (crypt) and horizontal (duodenum, cecum) axes of the intestine. Journal of Biological Chemistry 2002;277:33275–83.

161 Russell WMS BRL: The principles of humane experimental technique 1992.

162 Forssmann WG, Ito S, Weihe E, Aoki A, Dym M, Fawcett DW: An improved perfusion fixation method for the testis. The Anatomical Record 1977;188:307–14.

163 Kaske S, Krasteva G, König P, Kummer W, Hofmann T, Gudermann T, Chubanov V: TRPM5, a taste-signaling transient receptor potential ion-channel, is a ubiquitous signaling component in chemosensory cells. BMC Neuroscience 2007:8–49.

164 Wolock SL, Lopez R, Klein AM: Scrublet: Computational identification of cell doublets in single-cell transcriptomic data. Cell Systems 2019;8:281-291.e9.

165 Satija R, Farrell JA, Gennert D, Schier AF, Regev A: Spatial reconstruction of single-cell gene expression data. Nature Biotechnology 2015;33:495–502.

166 Klein MK, Haberberger RV, Hartmann P, Faulhammer P, Lips KS, Krain B, Wess J, Kummer W, König P: Muscarinic receptor subtypes in cilia-driven transport and airway epithelial development. The European Respiratory Journal 2009;33:1113–21.

167 Corish P, Tyler-Smith C: Attenuation of green fluorescent protein half-life in mammalian cells, Protein Engineering. Design and Selection 1999;12:1035–40.

168 Fleige H, Ravens S, Moschovakis GL, Bölter J, Willenzon S, Sutter G, Häussler S, Kalinke U, Prinz I, Förster R: IL-17-induced CXCL12 recruits B cells and induces follicle formation in BALT in the absence of differentiated FDCs. The Journal of Experimental Medicine 2014;211:643–51.

169 Hoover B, Baena V, Kaelberer MM, Getaneh F, Chinchilla S, Bohórquez DV: The intestinal tuft cell nanostructure in 3D. Scientific Reports 2017;7:1652.

170 Franck Z, Footer M, Bretscher A: Microinjection of villin into cultured cells induces rapid and long-lasting changes in cell morphology but does not inhibit cytokinesis, cell motility, or membrane ruffling. The Journal of Cell Biology 1990;111:2475–85.

171 Hunter DV, Smaila BD, Lopes DM, Takatoh J, Denk F, Ramer MS: Advillin is expressed in all adult neural crest-derived neurons. eNeuro 2018;5.

172 Shibata M, Ishii J, Koizumi H, Shibata N, Dohmae N, Takio K, Adachi H, Tsujimoto M, Arai H: Type F scavenger receptor SREC-I interacts with advillin, a member of the gelsolin/villin family, and induces neurite-like outgrowth. The Journal of Biological Chemistry 2004;279:40084–90.

173 Matteoli M, Haimann C, Torri-Tarelli F, Polak JM, Ceccarelli B, Camilli P de: Differential effect of alpha-latrotoxin on exocytosis from small synaptic vesicles and from large dense-core vesicles containing calcitonin gene-related peptide at the frog neuromuscular junction. Proceedings of the National Academy of Sciences of the United States of America 1988;85:7366–70.

174 Lips KS, Volk C, Schmitt BM, Pfeil U, Arndt P, Miska D, Ermert L, Kummer W, Koepsell H: Polyspecific cation transporters mediate luminal release of acetylcholine from bronchial epithelium. American Journal of Respiratory Cell and Molecular Biology 2005;33:79–88.

175 Song P, Rekow SS, Singleton C-A, Sekhon HS, Dissen GA, Zhou M, Campling B, Lindstrom J, Spindel ER: Choline transporter-like protein 4 (CTL4) links to non-neuronal acetylcholine synthesis. Journal of Neurochemistry 2013;126:451–61.

176 Cosgrove J, Novkovic M, Albrecht S, Pikor NB, Zhou Z, Onder L, Mörbe U, Cupovic J, Miller H, Alden K, Thuery A, O'Toole P, Pinter R, Jarrett S, Taylor E, Venetz D, Heller M, Uguccioni M, Legler DF, Lacey CJ, Coatesworth A, Polak WG, Cupedo T, Manoury B, Thelen M, Stein JV, Wolf M, Leake MC, Timmis J, Ludewig B, Coles MC: B cell zone reticular cell microenvironments shape CXCL13 gradient formation. Nature Communications 2020;11:3677.

177 Wang G-Z, Cheng X, Zhou B, Wen Z-S, Huang Y-C, Chen H-B, Li G-F, Huang Z-L, Zhou Y-C, Feng L, Wei M-M, Qu L-W, Cao Y, Zhou G-B, [No last name!]: The chemokine CXCL13 in lung cancers associated with environmental polycyclic aromatic hydrocarbons pollution. eLife 2015;4.

178 Fujita T, Kanno T, Kobayashi S: The paraneuron. Chapter 3. Secretions and secretory granules. Tokyo: pp 13-39, Springer, 1988.

179 Gu X, Karp PH, Brody SL, Pierce RA, Welsh MJ, Holtzman MJ, Ben-Shahar Y: Chemosensory functions for pulmonary neuroendocrine cells. American Journal of Respiratory Cell and Molecular Biology 2014;50:637–46.

180 Morales-Tirado V, Johannson S, Hanson E, Howell A, Zhang J, Siminovitch KA, Fowell DJ: Cutting edge: selective requirement for the Wiskott-Aldrich syndrome protein in cytokine, but not chemokine, secretion by CD4+ T cells. Journal of Immunology 2004;173:726–30.

181 Reikvam H, Aasebø E, Brenner AK, Bartaula-Brevik S, Grønningsæter IS, Forthun RB, Hovland R, Bruserud Ø: High constitutive cytokine release by primary human acute myeloid leukemia cells is associated with a specific intercellular communication phenotype. Journal of Clinical Medicine 2019;8.

182 Kuroda E, Ozasa K, Temizoz B, Ohata K, Koo CX, Kanuma T, Kusakabe T, Kobari S, Horie M, Morimoto Y, Nakajima S, Kabashima K, Ziegler SF, Iwakura Y, Ise W, Kurosaki T, Nagatake T, Kunisawa J, Takemura N, Uematsu S, Hayashi M, Aoshi T, Kobiyama K, Coban C, Ishii KJ: Inhaled fine particles induce alveolar macrophage death and interleukin-1α release to promote inducible bronchus-associated lymphoid tissue formation. Immunity 2016;45:1299–310.

183 Neyt K, GeurtsvanKessel CH, Deswarte K, Hammad H, Lambrecht BN: Early IL-1 signaling promotes iBALT induction after influenza virus infection. Frontiers in Immunology 2016;7:312.

184 Barone F, Nayar S, Campos J, Cloake T, Withers DR, Toellner K-M, Zhang Y, Fouser L, Fisher B, Bowman S, Rangel-Moreno J, La Garcia-Hernandez MdL, Randall TD, Lucchesi D, Bombardieri M, Pitzalis C, Luther SA, Buckley CD: IL-22 regulates lymphoid chemokine production and assembly of tertiary lymphoid organs. Proceedings of the National Academy of Sciences of the United States of America 2015;112:11024–9.

185 Yang Y, Lian S, Meng L, Qu L, Shou C: Antibody array revealed PRL-3 affects protein phosphorylation and cytokine secretion. PLOS One 2017;12:e0169665.

186 Lan Q, Lai W, Zeng Y, Liu L, Li S, Jin S, Zhang Y, Luo X, Xu H, Lin X, Chu Z: CCL26 participates in the prl-3-induced promotion of colorectal cancer invasion by stimulating tumor-associated macrophage infiltration. Molecular Cancer Therapeutics 2018;17:276–89.

187 Shivaraju M, Chitta UK, Grange RMH, Jain IH, Capen D, Liao L, Xu J, Ichinose F, Zapol WM, Mootha VK, Rajagopal J: Airway stem cells sense hypoxia and differentiate into protective solitary neuroendocrine cells. Science (New York, N.Y.) 2021;371:52–7.

188 Borges M, Linnoila RI, Helgi J. K. van de Velde, Chen H, Nelkin BD, Mabry M, Baylin SB, Ball DW: An achaete-scute homologue essential for neuroendocrine differentiation in the lung. Nature 1997;386:852–5.

189 Ito T, Udaka N, Yazawa T, Okudela K, Hayashi H, Sudo T, Guillemot F, Kageyama R, Kitamura H: Basic helix-loop-helix transcription factors regulate the neuroendocrine differentiation of fetal mouse pulmonary epithelium. Development 2000;127:3913–21.

190 Seta Y, Stoick-Cooper CL, Toyono T, Kataoka S, Toyoshima K, Barlow LA: The bHLH transcription factors, Hes6 and Mash1, are expressed in distinct subsets of cells within adult mouse taste buds. Archives of Histology and Cytology 2006;69:189-98.

191 Seta Y, Oda M, Kataoka S, Toyono T, Toyoshima K: Mash1 is required for the differentiation of AADC-positive type III cells in mouse taste buds. Developmental Dynamics an official publication of the American Association of Anatomists 2011;240:775–84.

192 Kito-Shingaki A, Seta Y, Toyono T, Kataoka S, Kakinoki Y, Yanagawa Y, Toyoshima K: Expression of GAD67 and Dlx5 in the taste buds of mice genetically lacking Mash1. Chemical Senses 2014;39:403–14.

193 Hsu C-C, Seta Y, Matsuyama K, Kataoka S, Nakatomi M, Toyono T, Gunjigake KK, Kuroishi KN, Kawamoto T: Mash1-expressing cells may be relevant to type III cells and a

subset of PLCβ2-positive cell differentiation in adult mouse taste buds. Cell and Tissue Research 2021;383:667–75.

194 Aguayo Samuel M., Miller York E., Waldron James A. Jr., Bogin Robert M., Sunday Mary E., Staton Gerald W. Jr., Beam William R., King Talmadge E. Jr.: Idiopathic diffuse hyperplasia of pulmonary neuroendocrine cells and airways disease. The New England Journal of Medicine 1992;

195 Aita K, Doi M, Tanno K, Oikawa H, Myo-Thaik-Oo, Ohashi N, Misawa S: Pulmonary neuroendocrine cell distribution in sudden infant death syndrome. Legal Medicine 2000;2:134–42. 327:1285-1288.

196 Cutz E, Perrin DG, Pan J, Haas EA, Krous HF: Pulmonary neuroendocrine cells and neuroepithelial bodies in sudden infant death syndrome: potential markers of airway chemoreceptor dysfunction. Pediatric and Developmental Pathology the official journal of the Society for Pediatric Pathology and the Paediatric Pathology Society 2007;10:106–16.

197 Gillan JE, Cutz E: Abnormal pulmonary bombesin immunoreactive cells in Wilson-Mikity syndrome (pulmonary dysmaturity) and bronchopulmonary dysplasia. Pediatric Pathology 1993;13:165–80.

198 Gosney JR, Sissons MC, Allibone RO, Blakey AF: Pulmonary endocrine cells in chronic bronchitis and emphysema. The Journal of Pathology 1989;157:127–33.

8. Declaration

“I declare that I have completed this dissertation single-handedly without the unauthorized help of a second party and only with the assistance acknowledged therein. I have appropriately acknowledged and referenced all text passages that are derived literally from or are based on the content of published or unpublished work of others, and all information that relates to verbal communications. I have abided by the principles of good scientific conduct laid down in the charter of the Justus Liebig University of Giessen in carrying out the investigations described in the dissertation.”

Giessen 2021

Wafaa Mahmoud

9. Acknowledgement

Throughout the course of my PhD degree, I have received a great deal of support and assistance.

I acknowledge the generous financial support from Jordan University of Science and Technology, Justus Liebig University Giessen, the German Research Foundation (DFG), the German Center for Lung Research (DZL) and the Excellence Cluster Cardio-Pulmonary Institute (CPI).

I would like to express my sincere gratitude to my supervisor, Professor Wolfgang Kummer, for his continued guidance, patience, and support. I have benefited greatly from his wealth of knowledge and meticulous editing. I am extremely grateful that he accepted to supervise me and continued to have faith in me over the years. Whose expertise was invaluable in formulating the research questions and methodology. His insightful feedback pushed me to sharpen my thinking and brought my work to a higher level.

I would like to extend my sincere thanks to my colleague Mr. Alexander Perniss, his immense help, knowledge, and plentiful experience have encouraged me all the time.

I would like to offer my special thanks to Dr. Renate Paddenberg for her treasured support and scientific knowledge which were influential in shaping my starting in the lab.

I would like to thank my lab mates, colleagues and research team. Special thanks to Dr. Krupali Poharkar, Dr. Uwe Pfeil, Dr. Maryam Keshavarz, Dr. Klaus Deckmann, Dr. Ulrich Gärtner, Mrs. Petra Mermer, Mrs. Anika Seipp, Mrs.Tamara Papadakis, Mr. Gerhard Kripp and Mr. Martin Bodenbenner-Türich for their assistance at every stage of the research project.

I am deeply grateful to Ms. Patricia Berger for her extraordinary support and help from my starting time in Germany until the end.

Finally, I would like to express my gratitude to my father, my husband, my children (Alaa and Saif), and all my brothers and sisters especially Diana. Without their tremendous understanding and encouragement in the past few years, it would be impossible for me to complete my study.

This thesis is heartily dedicated to the memory of my mother.

List of publications

List of publications:

1. Mahmoud W, Perniss A, Poharkar K, Soultanova A, Pfeil U, Hoek A, Bhushan S, Hain T, Gärtner U, Kummer W. CXCL13 is expressed in a subpopulation of neuroendocrine cells in the murine trachea and lung. Cell Tissue Res. 2021 Nov 11. doi: 10.1007 / s00441-021-03552-2. Epub ahead of print. PMID: 34762185.
2. Mustafa AG, Allouh MZ, Ghaida JH, Al-Omari MH, Mahmoud WA. Branching patterns of the aortic arch: a computed tomography angiography-based study. Surg Radiol Anat. 2017 Mar; 39 (3): 235-242. doi: 10.1007 / s00276-016-1720-z. Epub 2016 Jun 23. PMID: 27338939.